# NOVEL MATERIALS FOR LIGHT GAS SEPARATION AND REACTION ENGINEERING APPLICATIONS

A Thesis

by

NAVEEN KUMAR MISHRA

Submitted to the Office of Graduate and Professional Studies of
Texas A&M University
in partial fulfillment of the requirements for the degree of

DOCTOR OF PHILOSOPHY

| | |
|---|---|
| Chair of Committee, | Benjamin A. Wilhite |
| Committee Members, | Micah J. Green |
| | Mahmoud El-Halwagi |
| | Jaime Grunlan |
| Head of Department, | Arul Jayaraman |

May 2021

Major Subject: Chemical Engineering

# ABSTRACT

This work focuses on modifying active membrane of polymeric substrates using layer by layer coatings and laser induced graphene for hydrogen purification and carbon capture applications. Membranes offer an alternate solution for gas separation over the current industrial process including pressure swing adsorption and cryogenic distillation. Polymeric membranes owing to the cost-effective, energy efficient, and low carbon footprint operation can be used for gas separation applications, however, polymeric membranes have intrinsic trade-off between permeability and selectivity of the membrane.

This thesis focuses on two topics: a) Layer-by-layer (LbL) coatings on hollow fibers composed of poly amide imide (Torlon©), and b) laser-induced graphene (LIG) on polysulfone films. In LbL deposition process, alternate layers of polycationic and polyanionic polymers are deposited on a substrate to form highly cross-linked and inter-diffused layers. In this work, two polymeric pairs were investigated: (a) Polyethyleneimine (PEI) and polyacrylic acid (PAA) pair for hydrogen and, (b) Poly methacrylic acid (PMMA) and polyethylene oxide (PEO) pair for carbon capture. This work utilized the LbL technique to fabricate a new class of highly selective and composite polymer membrane on Torlon© based hollow fibers for hydrogen separation and carbon capture applications.

For laser-induced graphene/polysulfone membrane, $CO_2$ laser was used to photothermally reduce the top surface of the polymeric film to LIG layer. Optimal parameters of laser were identified to get defect-free and reproducible membranes. The LIG/polysulfone membranes resulted in an improvement in the permeability and selectivity of the neat polysulfone film.

## DEDICATION

To my parents, wife, and family; and in memory of my grandparents. Thank you for loving and supporting me all these years. Live and let live!

# ACKNOWLEDGMENTS

I would like to thank my research advisor Dr. Benjamin A. Wilhite for his constant guidance and support during my graduate years. Special thanks to Dr. Micah Green and Dr. Nutan Patil for teaching me principles of electromagnetic heating and nanomaterials. I am grateful to my committee members: Dr. Mahmoud El-Halwagi, Dr. Jaime Grunlan, and Dr. Micah Green for their time to serve on my PhD committee.

Thanks to Dr. Srikant and Sunjeev Venkateswaran for making me feel welcome in the group and training me. Thank you to my fellow colleagues Dr. Nutan Patil, Anas Muhammad, and Xiaofei Zhao for their contribution in my projects.

# CONTRIBUTORS AND FUNDING SOURCES

## Contributors

This work was supported by a dissertation committee consisting of Dr. Benjamin Wilhite, Dr. Micah Green, Dr. Mahmoud El-Halwagi, and Dr. Jaime Grunlan of Texas A&M University.

I would like to thank Dr. David Hopkinson and Dr. Shouliang Yi from National Energy Technology Laboratory for providing hollow fibers studied in chapter 2 and chapter 3 of this work. I would also like to acknowledge Materials Characterization Facility at Texas A&M University for SEM and nanoindentation analysis and the assistance of Drs. Yordanos Bisrat and Dr. Wilson Serem. Dr. Green's group has contributed equally for Laser Induced Graphene membranes in chapter 4 and RF reactor for chemical manufacturing work in Appendix A; Nutan and Naveen contributed equally and are the co-first authors for both projects. RF reactor project is a part of Dr. Nutan Patil's thesis.

## Funding Sources

The support of the United States Department of Energy, National Energy Technology Laboratory through NETL-Penn State University Coalition for Fossil Energy Research (UCFER, contract number DE-FE0026825) is gratefully acknowledged.

# NOMENCLATURE

LbL = Layer-by-Layer

PEI = polyethyleneimine

PMAA= polymethyl acrylic acid

PAI = polyamide imide

DI = Deionized water

FTIR = Fourier-transform infrared spectroscopy

GPU = Gas permeation unit

RF = Radio Frequency

MW = Microwave

MWCNT = Multiwalled carbon nanotubes

SEM = Scanning Electron Microscope

XRD = X-ray Diffraction

XPS = X-ray photoelectron spectroscopy

TGA = Thermal Gravimetric Analysis

DSC = Differential Scanning Calorimetry

PAN = polyacrylonitrile

PPI = Points per Inch

C = Carbon

# TABLE OF CONTENTS

# LIST OF FIGURES

Page

# LIST OF TABLES

Page

# 1. Introduction

The separation of mixtures to purify components is one of the most significant process in the chemical and petrochemical industry accounting for about 10-15% of total global energy consumption.[1-3] Current industrial processes for gas separation include cryogenic distillation, pressure swing adsorption. Cryogenic distillation has been used to produce high purity gases including nitrogen, oxygen, and argon at large scale. Air separation unit is one of the most critical components of chemical industry producing high purity liquid oxygen, liquid argon, and liquid nitrogen.[4] Pressure swing adsorption (PSA) utilizes the adsorption property of gases on specific materials like zeolites to separate the desired components from the mixture. The gas mixture passes through a packed column with pellets or powder, and when the gas gets compressed it adsorbs on the pellets or powder.[5] With continuous pressurization/depressurization cycle the desired gas is separated out of the mixture. These state-of-the-art processes are complex, costly at smaller scale, and has limited modularity for distributed manufacturing. Membranes offer unique advantage over existing industrial process in terms of low cost, energy efficiency, small carbon footprint, and complexity of operation.

Membrane based gas separation have been extensively used since late 1970s with the development of Prism© by Permea for hydrogen for hydrogen separation from the purge streams of ammonia plants.[6] The utilization of membranes has significantly expanded, and its usage have been improved as a part of standalone or hybrid separation units. The gas separation market size in expected to reach $1 billion by 2025. The major accomplishments by industries in recent years have been listed in Table 1.1.

**Table 1: Industrially used membranes.**

| Year | Description | Company |
|---|---|---|
| 1980 | First Plant with polysulfone hollow fiber membranes for $H_2/N_2$ | Permea (Now Air products) |
| 1982 | Cellulose triacetate membranes for $CO_2/H_2$ | Separex |
| 1983 | First Plant with cellulose acetate spiral wound membranes for $CO_2$ separation in EOR | Cynara |
| 1984 | Polysulfone hollow fiber membranes for $O_2/N_2$ | Dow Chemicals |
| 1987 | Composite hollow fiber membranes for $O_2/N_2$ | IMS |
| 1989 | Polyimide membranes for $H_2$ separation | Ube |
| 1991 | Polyphenylene oxide membranes for air separation | Delair |
| 1994 | Polyimide hollow fibers membranes $CO_2/CH_4$ | Medal |
| 1998 | Field test of membrane contactors for CO2/N2, | Kvaerner |
| 1995 | cellulose acetate membranes for $CO_2$/natural gas separation | UOP |
| 2008 | Teflon composite membranes, for $CO_2$ removal | MTR |
| 2010 | Pilot plant with polyethylene oxide membranes for $CO_2$ separation | MTR |
| 2018 | Olefin-paraffin separations | Compact Membrane Systems |
| 2018 | Dissolved Gas Removal | Compact Membrane Systems |

## 1.1 Light gas separation

Membranes have garnered great traction for light gas separation in the industrial application including hydrogen recovery during ammonia preparation from ($H_2$ from $N_2$), Oxygen or nitrogen enrichment of air ($O_2$ from air), natural gas or biogas upgrading, large scale $CO_2$ capture from flue gas originating from power plants, $H_2$ from hydrocarbons in the refinery, $H_2$ and CO separation for syn gas ratio adjustment, removal of $H_2S$ for acid gas treatment or sour gas

treatment, removal of moisture from air for air dehydration, Helium recovery from $He/N_2$ mixtures.

### *1.1.1 Separation of $O_2$ and $N_2$*

Oxygen-enriched air is used in a multitude of applications in several chemical and environmental, and medical processes.[7] Nitrogen is used as an inert blanketing for storing and shipping inflammable liquids, fresh fruits, and vegetables. Production of high purity nitrogen from the air using membrane is comparatively easier than the production of high purity oxygen owing to the composition of air.[8] For separating $O_2$ or $N_2$ from the air, the feed air is compressed and then it is passed through a membrane that selectively filters out either nitrogen or oxygen. The gases produced are already pressurized and can be easily transported. Although there has been significant improvement in the membranes used for oxygen enrichment there is a need for much improvement in terms of selectivity and throughput of the membranes to compete with current industrial practices.

### *1.1.2 Separation of $H_2$ from hydrocarbon*

Hydrogen recovery in refineries has become increasingly important as well as economical with new environmental restriction, fuel specifications, and increased processing of heavier crude.[9] In the refinery, the main source of hydrogen is catalytic naphtha reforming, however, at the same time, there are multiple rich hydrogen purge gas streams or the off-gas streams which contribute up to 20% of the total hydrogen production.[10] Typically, pressure swing adsorption or cryogenic distillation is used in the refinery for large scale hydrogen separation. Membrane can be used for relatively smaller scale or in hybrid with PSA or cryogenic distillation. Separation of hydrogen

from methane has been one of the promising applications where inorganic membranes can be used.[11-12]

### *1.1.3 Separation of $H_2$ and CO*

Carbon monoxide is key raw material for the production of major chemical products such as liquid hydrocarbon fuels that typically use Fischer-Tropsch process.[13] Synthesis gas is commonly produced from natural gas, oil, coal, or any other any other carbon sources results in a mixture of Hydrogen, Carbon monoxide, and small races of carbon dioxide. The $H_2$:CO ratio in the product stream is roughly around 1:3. However, for its use in the production of acetic acid, methanol, plasticizers on any other valuable products, this ratio needs to be reduced. The syn gas enrichment can be achieved by selectively removing hydrogen as permeate through a membrane.[14]

### *1.1.4 Separation of $H_2$ and $N_2$*

Ammonia is an important product in the chemical industry wire annual production exceeding 200 million tons.[15] Although, ammonia production requires a large amount of hydrogen, it also releases a vast amount of hydrogen in purge gas mainly containing hydrogen (60-70%) and nitrogen (20-25%) that needs to be reused. Hydrogen and nitrogen separation using membrane is one of the most difficult gas pairs for separations owing to similar kinetic diameter and quadrupole moment.[16] Metallic membranes have an excellent permeability for H2, especially Pd or Pt based membrane.[17] Inorganic membranes along wine zeolites and metal-organic framework (MOFs) have been considered for potential membrane materials owing to their uniform pore size, framework structure, and molecular sieving properties.[16]

### *1.1.5 Separation of $H_2$ and $CO_2$*

Currently, in the industry, hydrogen is produced from thermochemical conversions of hydrocarbon sources including natural gas, oil, and coal.[18] These processes result in a mixture of hydrogen and carbon dioxide that needs to be purified for further usage. The current state-of -the-art processes for hydrogen separation, including pressure swing adsorption or cryogenic distillation, are extremely complex costly, and leave a large carbon footprint.[19] Membranes provide a better alternative over the existing processes in terms of low cost, low energy use, and ease of operation. Oftentimes, membranes are used in the industry in hybrid form alongside existing processes to achieve economical separation and purification of hydrogen from mixed gas stream.[20] Apart from hydrogen separation after the reforming or oxidation process in the industry, $H_2/CO_2$ separation is also used in the pre-combustion carbon capture.[21] Pre-combustion carbon capture process refers to removing $CO_2$ from fossil fuels before the combustion is complete typically used in the gasification process where feedstock such as coal is partially oxidized in steam and oxygen/air at high temperature and pressure to form synthesis gas. This product oftentimes has $CO_2$ concentration in the range of 15-50% that can be captured, separated, and transported for sequestration.[22-23] The pre-combustion process is preferred over post combustion as the pre-combustion streams are concentrated and are at elevated pressure aiding in the separation by membrane.

## 1.2 Basic concept of membrane separation

Membrane in simplest terms can be stated as any semipermeable barrier which under a driving force permits preferential transfer of desired species or components in gaseous and/or liquid mixture solution. Membrane-based separations are based on the selective transport of one type of gas through the membrane. Species that pass through the membrane is termed as permeate

and species rejected by the membrane is called retentate. The driving force exists in the form of pressure, concentration or sometimes voltage difference across the membrane. Membranes are defined by two most important parameters describing their performance i.e., permeability and selectivity. Permeability is defined by the throughput of the membrane and it is an indication of the overall capacity of the membrane. Selectivity is defined the ratio of permeabilities of different components in simple terms it is the ability of membrane to selectively transfer desired gas over other components.

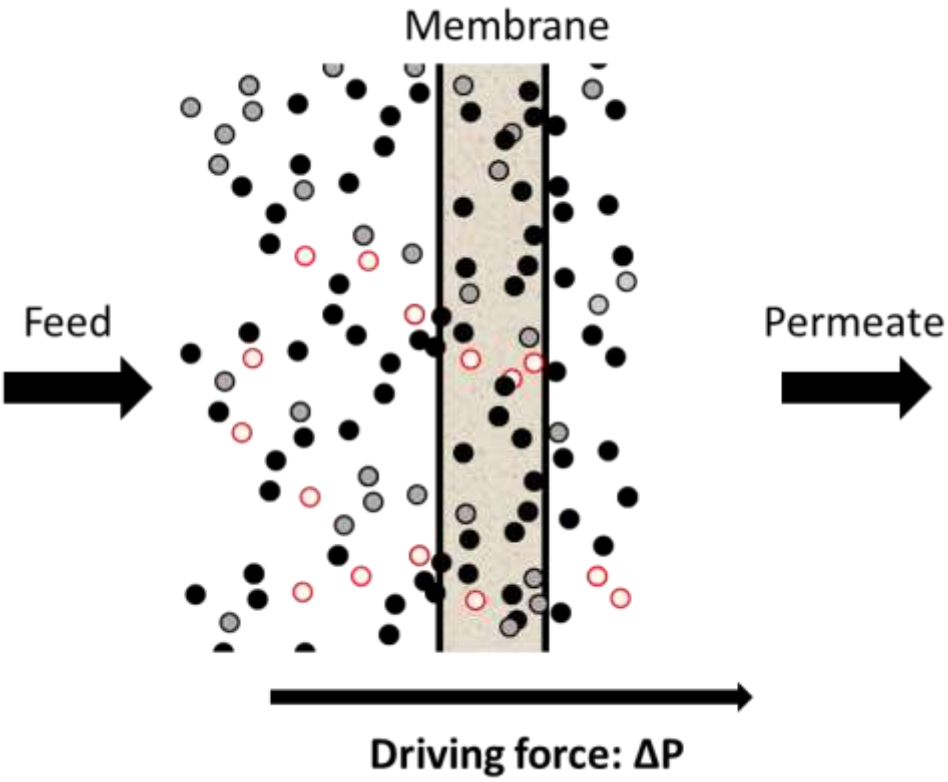


*Figure 1.2 1: Schematic diagram of gas separation by a membrane*

Depending upon the pore size, pore structure, and the free volume, gases follow different mechanism while they transfer across the membranes i.e., (1) Poiseuille flow, (2) Knudsen diffusion, (3) Molecular sieving, and (IV) solution-diffusion. The first three mechanism is dependent upon the pore size of the membrane and the gases are separated using the molecular size through the small pores of the membrane. Polymeric membranes follow solution-diffusion

mechanism, and the permeability of the gases are dependent upon the solubility of the gases in the membrane and diffusivity of the gases through the membrane.

### *1.2.1 Poiseuille flow*

When the pore size of the membrane is larger than the mean free path of the gases and gases follow viscous flow. The membrane contains large flow and enough to allow convective flow to occur, the gas molecule collide with each other and no separation is obtained between the gas components. Poiseuille flow (or Hagen-Poiseuille) is observed for the membranes that have much larger pore size than the gas molecules and the flux is directly proportional to $r^4$.

### *1.2.2 Knudsen diffusion*

When the ration pore size of the membrane over the mean free of the gases are less than unity the gases follow Knudsen diffusion. In this case, there are more collision between the gas molecule and the wall compared to collision among the gas molecules. The separation of different gases is achieved based on the respective velocity of the gases through the pores of the membrane. The selectivity of binary gases can be estimated from the square root of the ratio of the molecular weights.[24]

### *1.2.3 Molecular Sieving*

Molecular sieving occurs in membranes having uniform channels and the pore diameter is in between those of the gas molecules to be separated.[25-26] If the membrane has the pore size between the diameter of the smaller and larger gas molecules, only the smaller molecule can permeate resulting in extremely high selectivity. The porosity of these membranes results in higher permeability and at the same time high selectivity is achieved through effective size and shape separation of the gas species. Typically, the pore size in angstrom range which can be used to

selectively filter a multitude of gas pairs i.e., $O_2/N_2$, $H_2/CO_2$, $CO_2/CH_4$. Zeolites, graphene, molecular organic frameworks (MOFs) and other recently developed 2-D materials exhibit molecular sieving mechanism.

### *1.2.4 Solution-diffusion mechanism*

The solution-diffusion mechanism occurs in polymeric membranes where gases dissolve in the membrane material and then diffuse through the membrane depending upon the pressure gradient.[27-30] A separation between different components of feed gas occurs due to the difference in the number of gases dissolving in the polymeric matrix and the rate at which the gases diffuse through the membrane. Based on this mechanism the permeability coefficient of a polymer for a gas A can be written as

$$P_A = S_A D_A$$

Where, $S_A$ is the solubility coefficient and $D_A$ is the diffusion coefficient of gas A

For a given pair of gas components (e.g., $O_2/N_2$, $H_2/CO_2$, $CO_2/CH_4$, etc.), permeability coefficient and selectivity are fundamental parameters characterizing the membrane performance. The permeability coefficient is the product of permeance (gas flux across the membrane) and the thickness of the membrane. Gas selectivity is the ratio of the permeability coefficients of the gases where, $P_A$ is the permeability of gas A and $\alpha_{A/B}$ is the selectivity of the membrane.

$$\alpha_{A/B} = \frac{P_A}{P_B}$$

Polymer with high selectivity as well as high permeability is desired. High permeability directly translates to reduction in the surface area required for high throughput of the industrial requirement. High selectivity results in higher purity of the product gases. In combination, this will

reduce the capital cost of membrane units. However, homogenous polymeric membranes exhibit a trade-off between the permeability and selectivity. This trade-off relationship has shown to have an upper bound where the log of the selectivity vs the log of the higher permeability gas yielded a limit termed as "Robeson Upper Bound".[27, 29] The upper bound relationship is expressed by $P_A = k\alpha_{AB}^n$, where $\alpha_{AB}$ represents the selectivity of gas A over gas B and n is the slope of the upper bound. There exists a linear relationship between the $-1/n$ versus $\Delta d_{AB}$ (the different between the molecular diameter of the two gases).[31] Since its inception, this upper bound has become a benchmark for membrane performance and several published work has been able to surpass this upper bound.

## 1.3 Membrane modules

Membrane modules is the way membranes are arranged into final devices to achieve required specification, they are available in mainly three basic designs i.e., plate and frame, spiral wound, and hollow fibers. These modules are designed on the basis of hydrodynamic conditions, pressure difference required, product purity, energy consumption, membrane area, etc.

### *1.3.1 Plate-and-frame*

Plate and frame membrane system employs membrane put on a plate like structure that is held together by a frame support.[32-33] Flat sheet membranes are fixed with a frame similar to the filter press or plate type heat exchanger. Flat membranes are clamped together with spacers and porous membrane supports. There are two types of plate and frame membrane: dead-end plate and cross flow. As the name suggests, in dead-end plate and frame membranes the feed flows directly into the membrane while the crossflow system the flow is tangential. Typically, these plate and

frame membrane modules have low surface area to volume ratio which makes it difficult for its usage for gas separation.

### *1.3.2 Spiral wound*

Spiral wound membranes follow the same principle as the flat sheet frame and plate membrane with a sandwich of flat sheet membranes, spacers, and a porous support wrapped around cylindrically with a central tube that collects permeate. It offers advantage over plate and frame module in terms of surface area per unit volume of the membrane, typically 600 $m^2/m^3$ . The feed gas passes in the axial direction through the feed channels across the membrane surface and then the permeate is collected via the central porous tube. Spiral wound membrane modules are extensively used for ultra-filtration for reverse osmosis application.[34]

### *1.3.3 Hollow fibers*

Hollow fiber module typically contains 50 to 5000 self-supporting fibers with diameter in the range from 0.2 mm to 2 mm.[35-36] The packing densities for hollow fiber modules can be as high as 10000 $m^2/m^3$ which is significantly higher that other modules that is required for high throughput industrial feed gases.[37] Feed enters at higher pressure from one end and retentate leaves from the other end. The set up can be operated under co current and counter current flow patter with entry and exit ports at both ends. Hollow fiber modules are employed in multiple applications in the industry ranging from water filtration to bio reactor units. Commercial hollow fibers use commonly use phase inversion techniques with commonly used polymers including polyether sulfone (PES), polyetherimide (Ultem©), polyimides (Matrimid©). Several parameters (e.g., composition of dope solution, bore solution, flow rate, temperature of spinneret and bath

temperature) in the phase inversion process define the membrane morphology and gas permeation properties.[38]

## 1.4 Research objective and organization of the thesis

This research study aims at studying the application of novel materials for their use in membranes and reactors. This study focuses on two method of fabrication of membranes for their applications in hydrogen separation and carbon capture. In the last couple of decades there has been several discoveries of new materials that have great characteristic properties in terms of permeability and selectivity, however, their large-scale industrial application is limited by the ability to scale up and cast the material as either flat sheet membrane or hollow fiber membrane.

Chapter 2 and chapter 3 delves into the application of Layer-by-layer (LbL) deposition of micron level conformal coatings on polyamide imide based hollow fibers for enhanced light gas separation. LbL technique is method to deposit dense ultra-thin conformal coatings of functional polymeric films over a variety of substrates for applications as diverse as biomedicine, drug delivery, water purification, solar cells, optics, batteries, fuel cells, gas barriers, and gas separation. In chapter 4 a new approach to synthesis graphene-based material using $CO_2$ laser is used for $H_2/CO_2$ separation. Laser-induced graphene (LIG) shows promise as a membrane component because of its ease of production and scalability. LIG is fabricated when the surface of a polymer substrate is photothermally converted to graphene containing carbon material using a $CO_2$ laser.

### *1.4.1 Layer by layer membranes:*

The LbL process deposits alternate layers of polycationic and polyanionic pairs that form a highly cross-linked and inter-diffused layer by hydrogen bonding and ionic interactions.[39] Two polymeric pairs were investigated:(a) Polyethyleneimine and polyacrylic acid pair for hydrogen

separation due to the high solubility of hydrogen in LbL membrane; (b) Poly methacrylic acid and polyethylene oxide (PEO) pair for carbon capture, due to the dipole-quadrupole interaction between PEO and $CO_2$ molecules. This work utilized the LbL technique to fabricate a new class of highly selective and composite polymer membrane on Torlon© based hollow fibers for hydrogen separation and carbon capture applications.

A new and unique in-situ technique was developed by using inside a shell-and-tube assembly for LbL deposition to make defect-free and conformal coatings. This is a significant improvement over the traditional LbL approach which utilized dip-coating and often resulted in defective coatings due to vibrations and mechanical stresses induced on the substrate. The fabrication time was also reduced by 70% by using a surface functionalization approach to improve the hydrophilicity of the substrate. This low-cost and aqueous polymers deposition on polymeric hollow fiber has potential industrial applications. Future work will focus on understanding the solution-diffusion mechanism for improved membrane performance by estimating solubility, diffusivity, and adsorption behavior of gases using quartz crystal microbalance.

### *1.4.2 LIG membrane:*

This project utilizes $CO_2$ laser to photothermally reduce the top surface of the polysulfone film to laser-induced graphene (LIG) layer which offers high hydrogen perm-selectivity. This study involved the identification of optimal parameters of laser to get defect-free and reproducible membranes. The LIG/polysulfone membranes resulted in an improvement in the permeability and selectivity of the neat polysulfone film by a factor of 700 and 15, respectively. Future studies will focus on understanding the large improvement in the permeance of the LIG/polysulfone membrane and further optimize the process condition to achieve the highest possible performance. This rapid

approach of forming a thin selective layer on the polymeric substrate will pave a way for scalable membrane fabrication for high throughput applications.

## 2. Enhancing H2-Permselectivity of High-Flux Hollow Fiber Membrane Via in-Situ Layer-By-Layer Surface Treatment *

### 2.1 Introduction

Development of the emerging hydrogen economy combined with existing industry demand from fertilizer production, crude oil and biofuel upgrading, and semiconductor industry has driven the need for high purity hydrogen.[40-45] Current industrial practice for $H_2$ purification, specifically pressure-swing adsorption or cryogenic distillation, are both complex in nature and energy-intensive.[14] Polymeric gas separation membranes offer a passive, energy-efficient alternative, with asymmetric cellulose acetate, polyamide, and polysulfone membranes already in use by industry for air enrichment, natural gas upgrading, and hydrogen recovery from reformate mixtures.[28, 46] Gas transport in dense polymer films occurs via solution-diffusion mechanism, in which separation is achieved by exploiting the disparity in gas solubility (sorption selectivity) and/or solid-state diffusivity (size selectivity).[47] For the case of homogeneous size-selective dense polymeric membranes, there exists an intrinsic trade-off between permselectivity and permeability represented by "Robeson upper bound".[27, 31, 48] These polymers are typically cast in the form of asymmetric membranes consisting of a thick highly porous support layer (>200 μm) and a thin dense functional layer(<10 μm), such that overall gas permeance is maximized while retaining sufficient mechanical integrity at industrial scale. To-date, the implementation of new polymers

* Reprinted with permission from (Naveen K. Mishra, Nutan Patil, Carolyn Long, Shouliang Yi, David Hopkinson, Jaime C. Grunlan, and Benjamin A. Wilhite, Enhancing $H_2$-Permselectivity of High-Flux Hollow Fiber Membrane Via in-Situ Layer-By-Layer Surface Treatment. Journal of Membrane Science, 615, 118312. doi: https://doi.org/10.1016/j.memsci.2020.118312) Copyright 2020 Published by Elsevier B.V.

for gas separation has been limited by the ability to cast the material as either asymmetric flat-sheet or hollow fiber membranes at competitive cost.

Alternatively, a dense ultra-thin film of a novel polymeric material could be introduced on existing mechanical substrates via casting, application of Langmuir Blodgett films, or by layer-by-layer deposition. Layer-by-layer (LbL) assemblies continue to gain interest as a robust and low-cost means to achieve ultra-thin conformal coatings of functional polymeric films over a variety of substrates for applications as diverse as biomedicine, drug delivery, water purification, solar cells, optics, batteries, fuel cells, gas barriers, and gas separation.[49-56] Deposition of LbL films involves a cyclic process wherein a charged material (e.g. polyelectrolyte) is adsorbed onto a substrate followed by adsorption of an oppositely charged material, achieved by dipping, spinning, spraying, or rinsing via fluidic assembly;[57] during each deposition step, the charged materials adsorb, diffuse, and interact with the underlying layer to form an interconnected and/or diffused bi-layer. The resulting film properties can be manipulated by adjusting electrolyte concentration,[58] pH,[59] viscosity,[60] molecular weight,[61] deposition time,[62] and temperature.[63] Recently, LbL films have found usage in gas separation; Sullivan and Bruening deposited polyamic acid/polyallylamine hydrochloride on porous alumina support followed by imidization; resulting LbL coating displayed $H_2$:$N_2$ and $H_2$:$CO_2$ separations comparable to conventional polyimide films.[64] Subsequent studies demonstrated polyallyl-amine/polystyrene sulfonate on silicone substrate,[39] polyallylamine hydrochloride/polysodium-styrene sulphonate on oxidized poly4-methyl-1-pentene substrate both reported hydrogen selectivity similar to conventional membranes.[65] Our research group previously achieved $H_2$:$N_2$ and $H_2$:$CO_2$ selectivity in excess of 2000:1 and 200:1, respectively, at permeability ~5 barrer using LbL films of polyethyleneimine/polyacrylic acid deposited on an alumina-coated porous stainless-steel tubular substrate.[66] Given the promising

$H_2$-permselectivity displayed by the $[PEI_{10}/PAA_4]_x$ LbL films, the present work aims to apply these films to an industrially applicable, easily manufacturable hollow fiber substrate.

Asymmetric hollow fiber membranes are widely employed in industry for both liquid and gaseous separations, owing to intrinsic properties of high surface area to volume ratio, mechanical resistance to large pressure differences, low cost, and high flux.[67] Polyamide imide (PAI) is commonly used for the manufacturing of hollow fibers due to its excellent chemical and mechanical properties, arising from the presence of amide functional groups with excellent thermal stability attributed to the imide ring.[68] PAI-based hollow fibers provide stability against plasticization due to the presence of inter- and intra-chain hydrogen bonding. Several studies have focused on improving the hydrogen selectivity of PAI hollow fibers by use of thermal rearrangement,[69] crosslinking,[70] or chemical modification.[71] Polyethyleneimine (PEI) has been extensively used to chemically modify the PAI to introduce a positively charged surface which has found its use in water purification,[72] removal of Ciprofloxacin from water,[73] forward osmosis membranes,[74] $CO_2$ separation,[75] and carbon capture.[76] These unique properties make PAI-based hollow fibers an excellent candidate as a substrate for LbL deposition.

In this work, we demonstrate LbL deposition of sub-micron conformal coating on a highly selective membrane with competitive permeability on hollow fibers for enhanced light gas separation. The $H_2$ selectivity of high flux HF membranes was enhanced by the addition of Polyethylenimine (PEI)/polyacrylic acid (PAA) bilayers. The effect of surface functionalization was also studied to tune the substrate surface to provide a favorable condition for LbL deposition resulting in a highly selective membrane for hydrogen.

## 2.2 Experimental Section

### *2.2.1 Materials*

Branched polyethyleneimine (Millipore Sigma) (MW ~25,000 g $mol^{-1}$) and polyacrylic acid (Millipore Sigma) (MW ~100,000 g $mol^{-1}$) were dissolved into deionized water (18.2 MΩ) to prepare 0.1 wt % and 0.2 wt % solution, respectively. The pH of the PEI solution was adjusted to 10 from its unaltered value of 10.5 by adding 1 M hydrochloric acid solution (HCl) (Millipore sigma) and the pH of the PAA solution was adjusted to 4 from its unaltered value of 3.1 using 1 M sodium hydroxide solution (NaOH) (Millipore Sigma). For the functionalization, branched polyethyleneimine and water were mixed with 2-propanol to prepare a solution of 5: 5: 90 by wt %.

### *2.2.2 Substrate*

Asymmetric Torlon© (PAI) hollow fiber substrates were fabricated using a dry-jet wet-quench spinning process. A polymer dope was first formed by dissolving Torlon© into a mixture of 1-methyl-2-pyrrolidone (solvent) and DI water (non-solvent). LiCl was added as a pore-forming agent. The dope was well mixed by placing the jar on a roller for at least a week until the solution was homogenous. Hollow fibers were produced by co-extruding the polymer dope with the bore fluid via syringe pumps (Teledyne ISCO) through a custom spinneret, passing through an air gap and into a coagulation bath. The nascent fibers were kept in a DI water bath for three days to remove any residual solvent.

### *2.2.3 Set-up*

Individual hollow fibers were potted into a tube and shell assembly prepared using a 0.25-inch diameter tube and tee fittings (Swagelok), and hollow fibers (5 inches each), followed by sealing with epoxy adhesive (3M DP 100. This set upwas used for LbL deposition and permeation tests.

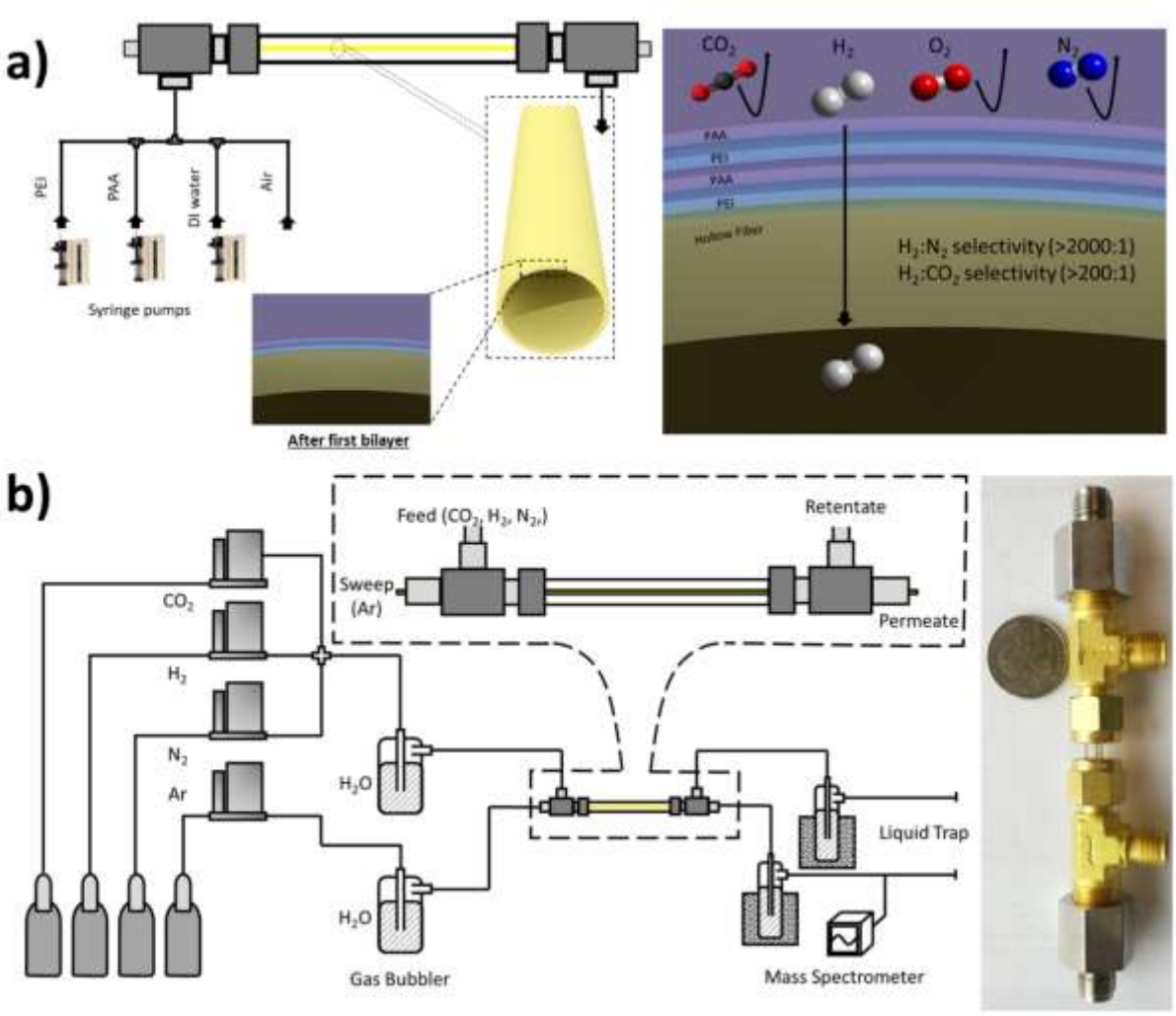


*Figure 2.2-1: A schematic diagram of a) Layer-by-layer deposition process and b) PEI/PAA layer-by-layer deposition on a hollow fiber support.*

### *2.2.4 Layer-by-layer Deposition*

Each bilayer was deposited by passing alternating aqueous cation-anion solutions through the annulus at a flow rate of 10 ml/min via a syringe pump (kdScientific KDS-100). PEI solution (0.1 wt %, pH 10) is introduced first, which deposits an initial positively charged layer over the neutral hollow fiber substrate surface. After 5 minutes, the system is rinsed three times with

deionized water at a flow (10 ml/min) for 30 s to remove excess polyelectrolyte, followed by air at the same flowrate to remove excess moisture. After three rinse-dry cycles, PAA solution (0.2 wt %, pH 4) is fed to the annulus of the assembly with the same flow rate and contact time, followed by identical rinsing and drying steps, to achieve a single [$PEI_{10}/PAA_4$] bilayer. After the initial bilayer, polyelectrolyte solutions were passed through the system for 2 minutes contact time and the steps were repeated to deposit a total of 10, 15, and 20 bilayers; denoted as [HF-$PEI_{10}/PAA_4]_{10}$, [HF- $PEI_{10}/PAA_4]_{15}$, and [HF- $PEI_{10}/PAA_4]_{20}$.

### *2.2.5 Surface Functionalization*

For the functionalization, hollow fibers were immersed in an IPA-PEI-water solution (5:5:90 wt %) for 4 hrs. at 70 $^oC$ in an oil bath followed by washing with DI water and drying at 70 $^o C$ overnight. For the LbL deposition on functionalized hollow fiber, PAA solution is used first to deposit a negatively charged layer upon the positively charged functionalized hollow fiber surface, followed by the deposition of a positively charged layer of PEI with identical flowrate, contact times, rinsing and drying steps as before. These steps were repeated for 2, 5, and 10 bilayers; denoted as [f-HF- $PEI_{10}/PAA_4]_2$, [f-HF- $PEI_{10}/PAA_4]_5$, and [f-HF- $PEI_{10}/PAA_4]_{10}$.

### *2.2.6 Characterization*

Contact angle measurements for the hollow fibers and functionalized hollow fibers were calculated using a sessile drop technique (water, 5 µL). The ImageJ software (National Institutes of Health (NIH), Bethesda, MD, USA) was used to analyze the contact angle by using a plug-in named Low-Bond Axisymmetric Drop Shape Analysis.[77] FTIR spectra of HF and f-HF were measured with a Bruker Optics ALPHA-P 10098-4 spectrometer in ATR mode. For the SEM

analysis, hollow fibers were cut after dipping it in liquid $N_2$ to preserve the cross-section. A Hysitron TI950 Triboindenter was used to measure the mechanical properties.

### *2.2.7 Permeation Study*

The shell and tube assemblies containing each coated hollow fiber were used to measure $H_2$ permeability as follows: Argon sweep gas (99.998% purity) was supplied to the bore of hollow fiber (30 ml/min), while a feed gas mixture of $N_2$ + $H_2$ or $CO_2$ + $H_2$ was supplied to the annulus region. The outlet of the bore hollow fiber (permeate) is continuously monitored via mass spectrometer (RGA 100, Stanford Research Systems). During the experiments, each membrane feed gas mixture was supplied to the annulus keeping the overall feed flowrate constant. The feed gas composition was varied only after the outlet signal of the mass spectrometer reaches a steady state (typically 10 minutes) for the previous feed gas composition.

All experiments were performed at room temperature (~21 °C) and atmospheric outlet pressure. For the present case of co-current flow, the overall observed permeability can be calculated using an observable log mean average driving force via Equation (1)

$$\boldsymbol{F_i = p_{bulk}\left[\frac{(p_p - p_r)-(p_f - p_s)}{ln\left[\frac{p_p - p_r}{p_f - p_s}\right]}\right]_i} \quad (1)$$

Where, $F_i$ is the measured permeation rate ($mol\ m^{-2}s^{-1}$) of species $i$, $t$ is the thickness of the membrane (m), $p_{bulk}$ is the overall observed permeance ($mol\ m^{-2}\ s^{-1}Pa^{-1}$) of the membrane, and $p_p, p_r, p_s$, and $p_f$ are the partial pressures of the permeate, retentate, sweep, and feed side for the species $i$, respectively. Gas selectivity of gas i over j ($\alpha_{i,j}$) is given by the ratio of their

respective permeabilities ($P_i/P_j$). $p_{bulk}$ values were calculated from the curve fitting of log mean pressure difference with permeation rate as shown in Figure. A resistance-in-series model was used to deduce the permeability of the selective layer by using the following equation.

$$\frac{1}{p_{bulk}} = \frac{t_{membrane}}{P_{membrane}} + \frac{1}{p_{substrate}} \quad (2)$$

Where, $p_{bulk}$ is the overall observed bulk permeance ($mol\, m^{-2}\, s^{-1} Pa^{-1}$) of the membrane, $p_{substrate}$ is the permeance of the substrate used, and $t_{membrane}$ is the thickness of the selective layer of membranes calculated using the SEM images. Equation 2 is used to calculate the permeability of the selective layers.

## 2.3 Results and Discussion

### *2.3.1 Surface Functionalization*

The outer surface of the hollow fiber is highly hydrophobic in nature, which restricts adsorption of the polyelectrolyte solution; thus, multiple bilayers are necessary to establish a favorable condition for subsequent uniform and defect-free layers to deposit. To address this, hollow fibers were functionalized prior to LbL deposition using a PEI-water-Isopropanol solution (5:5:90 wt %) to improve their surface properties. The strong nucleophilic primary amine group of the PEI attacks the electrophilic carbonyl group in the imide ring of the PAI hollow fiber backbone opening the imide ring as confirmed by FTIR (.[76] The untreated hollow fiber exhibit strong imide carbonyl (C=O) absorbance at 1750 $\boldsymbol{cm^{-1}}$ and 1730 $\boldsymbol{cm^{-1}}$ and an imide C-N absorbance at 1360 $\boldsymbol{cm^{-1}}$; the functionalized hollow fiber shows weaker absorbances for imide carbonyl group and none for the imide C-N absorbance confirming the breaking of C-N bond and opening of the imide ring. This results in a positively charged surface owing to the presence of

amine groups on the imide ring which improves the hydrophilicity of the HF substrate, confirmed by a decrease in the contact angle of the hollow fiber surfaces from 101° to 68° after functionalization.[77]

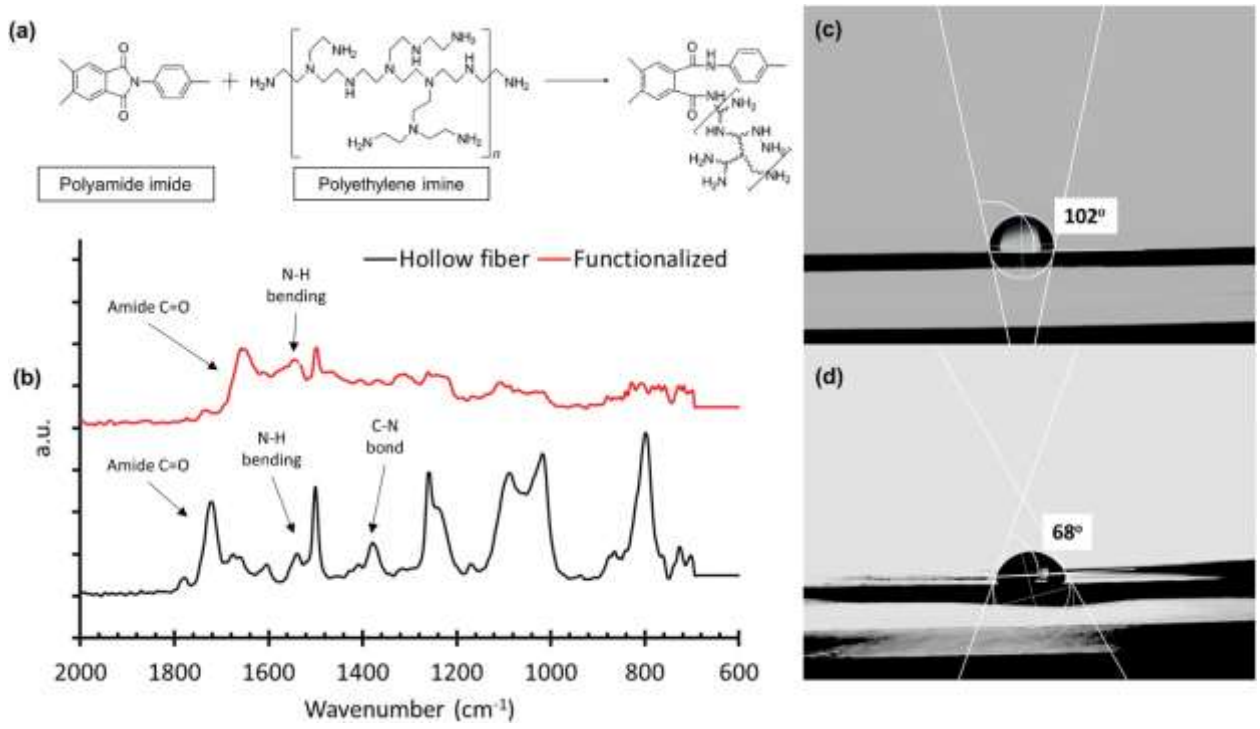


*Figure 2.2-2: Effect of functionalization of hollow fiber: (a) breaking of C-N amide bond in PAI backbone, (b) FTIR spectra supporting the bond breaking, and change in hydrophilicity of hollow fiber (c) before and (d) after functionalization.*

### *2.3.2 Morphology of PEI-PAA Membrane*

Cross-section and surface SEM images of hollow fibers confirm the presence of a dense LbL coating on each substrate. On the PEI-functionalized hollow fiber, defect-free conformal coatings were achieved with as low as 2 bilayers, which was not possible for non-functionalized hollow fibers. The LbL coating thickness of $[f\text{-}HF\text{-}PEI_{10}/PAA_4]_{10}$ is 8.2 µm which is roughly 1.5 times that of $[HF\text{-}PEI_{10}/PAA_4]_{10}$; this is attributed to the introduction of a positively charged surface on the hollow fiber after functionalization which aids in ionic interaction between the

oppositely charged layers. The deposition of LbL films on both untreated and functionalized hollow fibers followed exponential growth, similar to previously studied weak polyelectrolytes (including PEI and PAA); this behavior results from the charge overcompensation by the interpenetration of the polyelectrolyte through the layers.[78-79] Functionalization also resulted in a change in the pore structure of the hollow fiber as depicted in Figure 2.2-5.

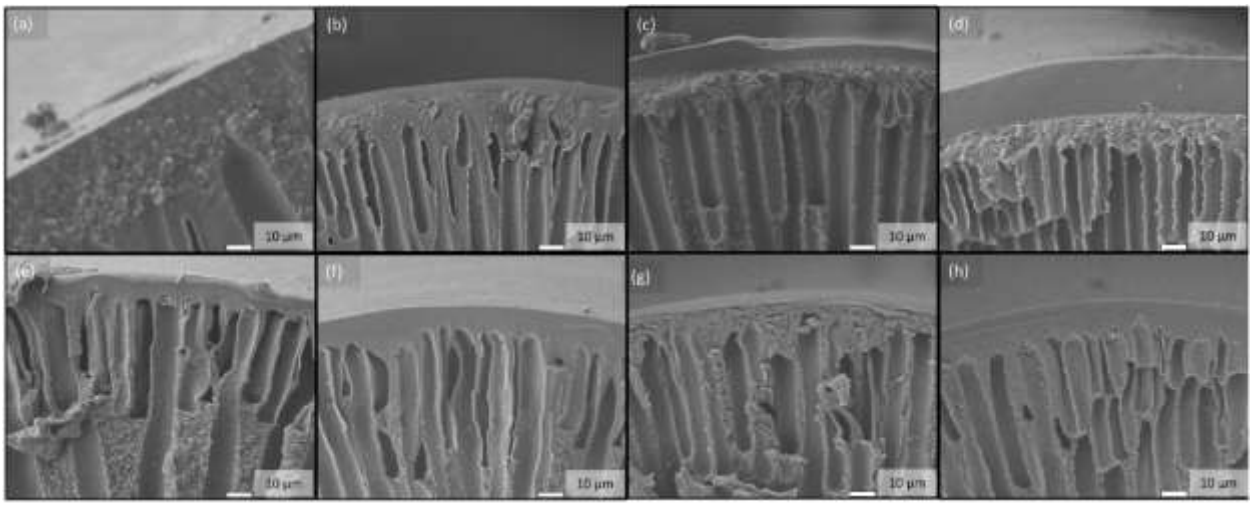


*Figure 2.2-3: SEM cross-sectional image of (a) hollow fiber, (b) [HF- PEI10/PAA4]10, (c) [HF- $PEI_{10}/PAA_4]_{15}$, and (d) [HF- $PEI_{10}/PAA_4]_{20}$, (e) functionalized hollow fiber, (f) [f-HF-$PEI_{10}/PAA_4]_2$, (g) [f-HF-$PEI_{10}/PAA_4]_5$, and (h) [f-HF-$PEI_{10}/PAA_4]_{10}$*

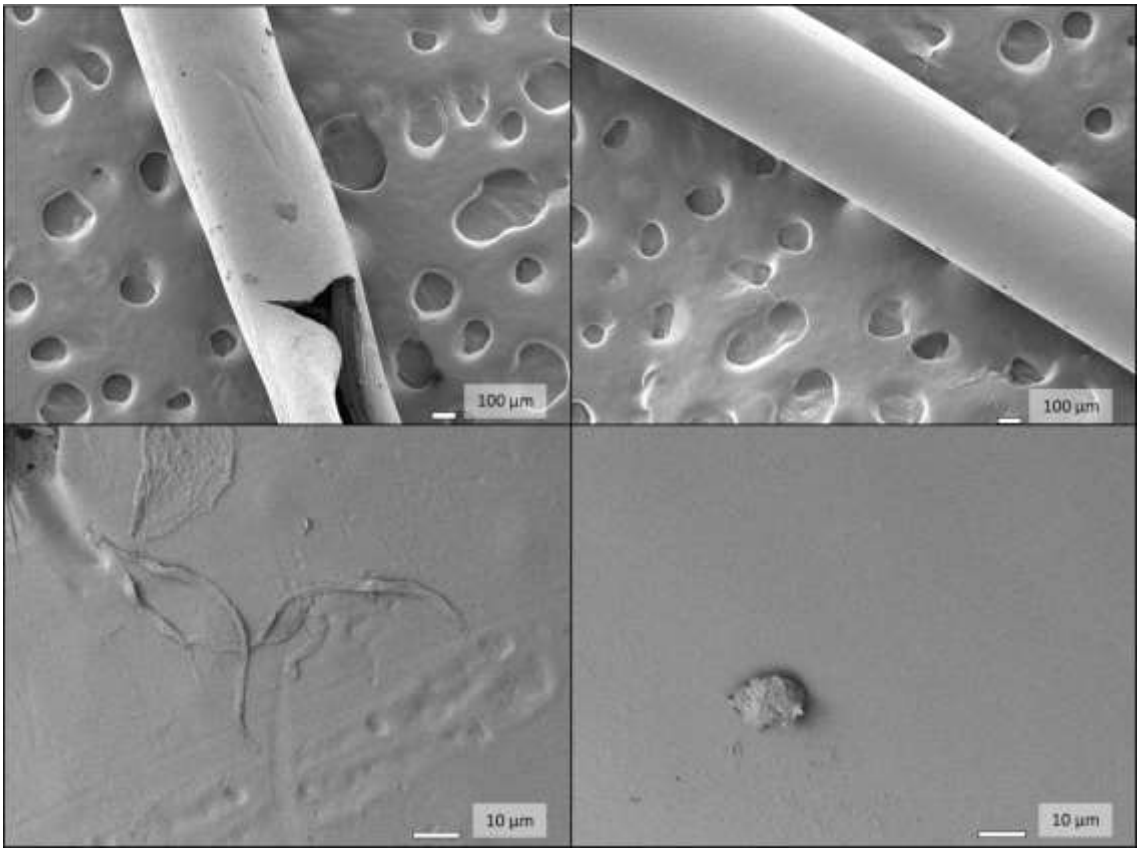


*Figure 2.2-4:SEM image of hollow fiber surface before (left) and after (right) LbL deposition indicating uniform membrane deposition.*

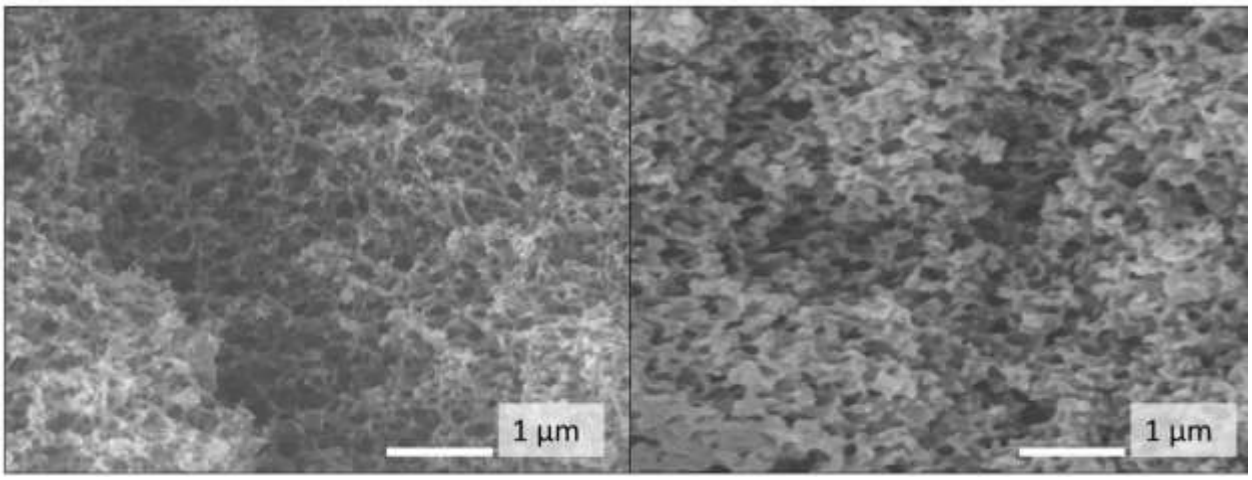


*Figure 2.2-5: Pore structure of hollowfiber (Left) changes after functionalization (Right) depicted by SEM images at 20,000 x magnification.*

### *2.3.3 Permeation Performance*

Initial gas permeation tests were performed with as-received hollow fibers prior to LbL coating or PEI-functionalization with observed $H_2$, $N_2$, and $CO_2$ permeance of 11886 GPU, 7561 GPU, and 8341 GPU, respectively. The gases follow Knudsen diffusion inside the as-received hollow fiber with observed selectivity for $H_2$:$N_2$ and $H_2$:$CO_2$ as 1.6 and 1.4, respectively. Upon deposition of each $PEI_{10}/PAA_4$ LbL films, the $H_2$ permeance decreased while $H_2$ selectivity improved significantly. Our previous studies confirmed that humidity plays an important role in the functioning of these LbL membranes assembly[66], as water molecules swell and plasticize the LbL films leading to bond reshuffling which heals micro-scale surface defects.[80-81] Thus, the feed was bubbled through DI water to achieve 50% RH prior to entering the shell-tube assembly. Figure 2.2-6 and Figure 2.2-7 presents the trend from no membrane to 20 bilayer deposition for $H_2/N_2$ and $H_2/CO_2$ gas pairs for hydrogen permeance with its selectivity. For the case of [HF-$PEI_{10}/PAA_4]_{20}$, permeate $N_2$ and $CO_2$ partial pressures remained below the detection limit of the mass spectrometer, such that a minimum observable $H_2$:$N_2$ and $H_2$:$CO_2$ selectivity of >2000:1 and >200:1, respectively, was based on the minimum detection limit calculated on the basis of three standard deviations of the baseline noise.[66]

Identical permeation studies were performed for PEI-functionalized hollow fiber with 0, 2, 5, and 10 bilayers of $PEI_{10}/PAA_4$. The functionalized hollow fiber showed an order of magnitude improvement in its $H_2$ selectivity which may be attributed to a change in the pore structure and composition of the outer functional layer of the hollow fiber observed via scanning electron microscopy (Figure 2.2-5). For the case of 5 bilayers of $PEI_{10}/PAA_4$ on functionalized hollow fiber, the $CO_2$ permeate signal again drops below the detection limit of the mass spectrometer, thus achieving similar levels of selectivity as of [HF-$PEI_{10}/PAA_4]_{20}$. This may be attributed to enhanced

carbon dioxide adsorption upon functionalization of hollow fiber with PEI, which has been reported by Koros *et. al.*[75], which may decrease the driving force of $CO_2$ partial pressure difference across the membrane. $CO_2$ and $N_2$ permeate pressures remained below the detection limit for 10 bilayers.

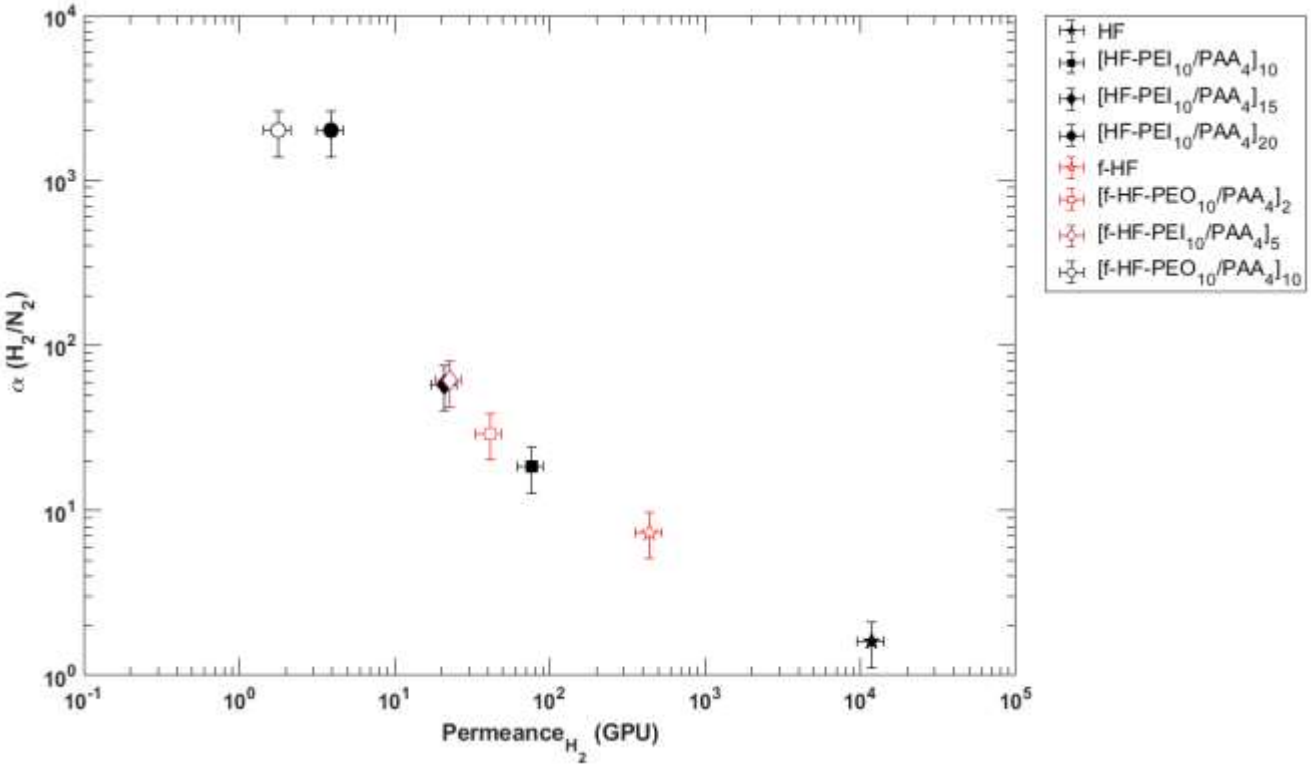


*Figure 2.2-6: Selectivity of $H_2$ over $N_2$ vs H2 Permeance for $H_2/N_2$ gas pair for hollow fiber, $[HF\text{-}PEI_{10}/PAA_4]_{10}$, $[HF\text{-}PEI_{10}/PAA_4]_{15}$, $[HF\text{-}PEI_{10}/PAA_4]_{20}$, functionalized hollow fiber, $[f\text{-}HF\text{-}PEI_{10}/PAA_4]_2$, $[f\text{-}HF\text{-}PEI_{10}/PAA_4]_5$, and $[f\text{-}HF\text{-}PEI_{10}/PAA_4]_{10}$*

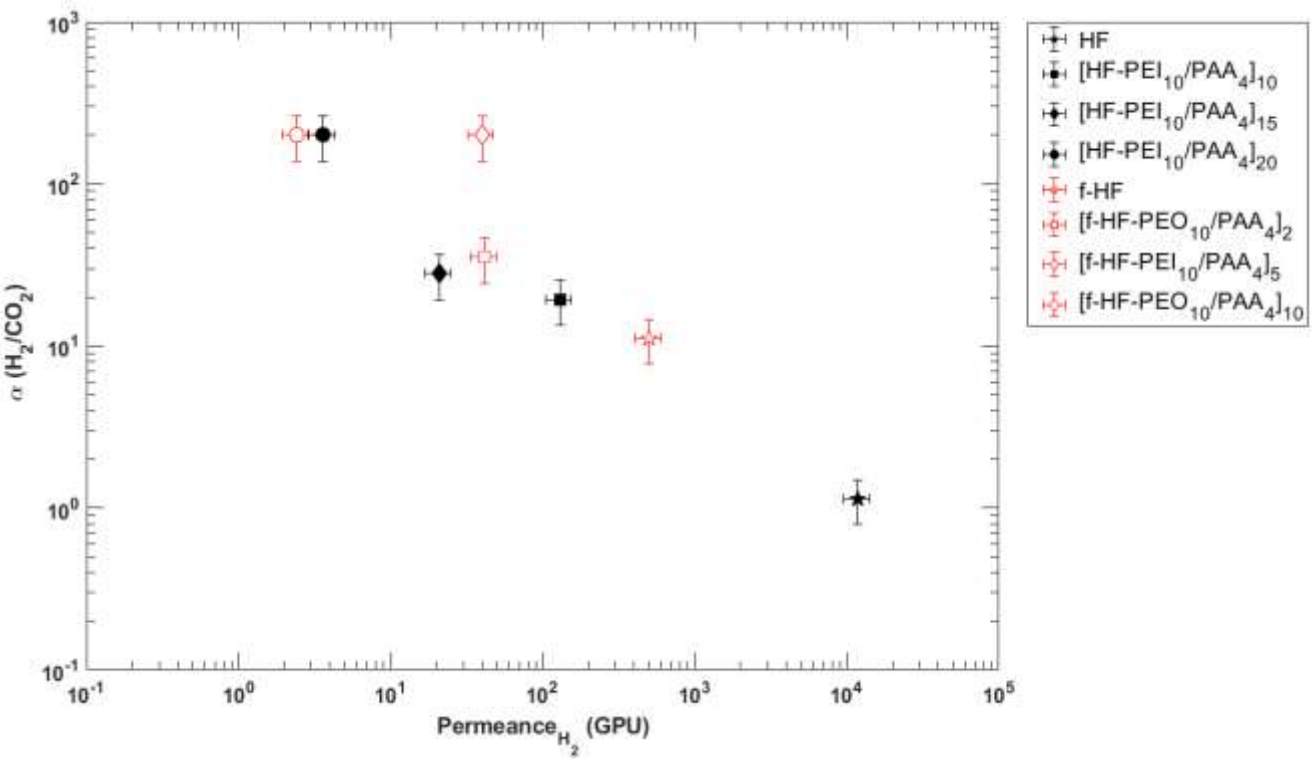


*Figure 2.2-7: Selectivity of $H_2$ over $CO_2$ vs $H_2$ Permeance for $H_2/CO_2$ gas pair for hollow fiber, [HF- $PEI_{10}/PAA_4]_{10}$, [HF- $PEI_{10}/PAA_4]_{15}$, [HF- $PEI_{10}/PAA_4]_{20}$, functionalized hollow fiber, [f-HF-$PEI_{10}/PAA_4]_2$, [f-HF-$PEI_{10}/PAA_4]_5$, and [f-HF-$PEI_{10}/PAA_4]_{10}$*

Figure 2.2-8 and Figure 2.2-9 compares the performances of these LbL films with the Robeson upper bounds for a) $H_2/N_2$ and b) $H_2/CO_2$ gas pairs; the permselectivity of LbL functional films can be tailored by tuning the number of bilayers. For the case of [HF-$PEI_{10}/PAA_4]_{20}$ and [f-HF-$PEI_{10}/PAA_4]_{10}$, the selectivity values exceed the Robeson upper bound for $H_2/N_2$ and $H_2/CO_2$ gas pair and [f-HF-$PEI_{10}/PAA_4]_5$ exceed the upper bound for $H_2/CO_2$ gas pair performing better than the Mixed matrix membrane, zeolites, and MOFs in terms of selectivity.

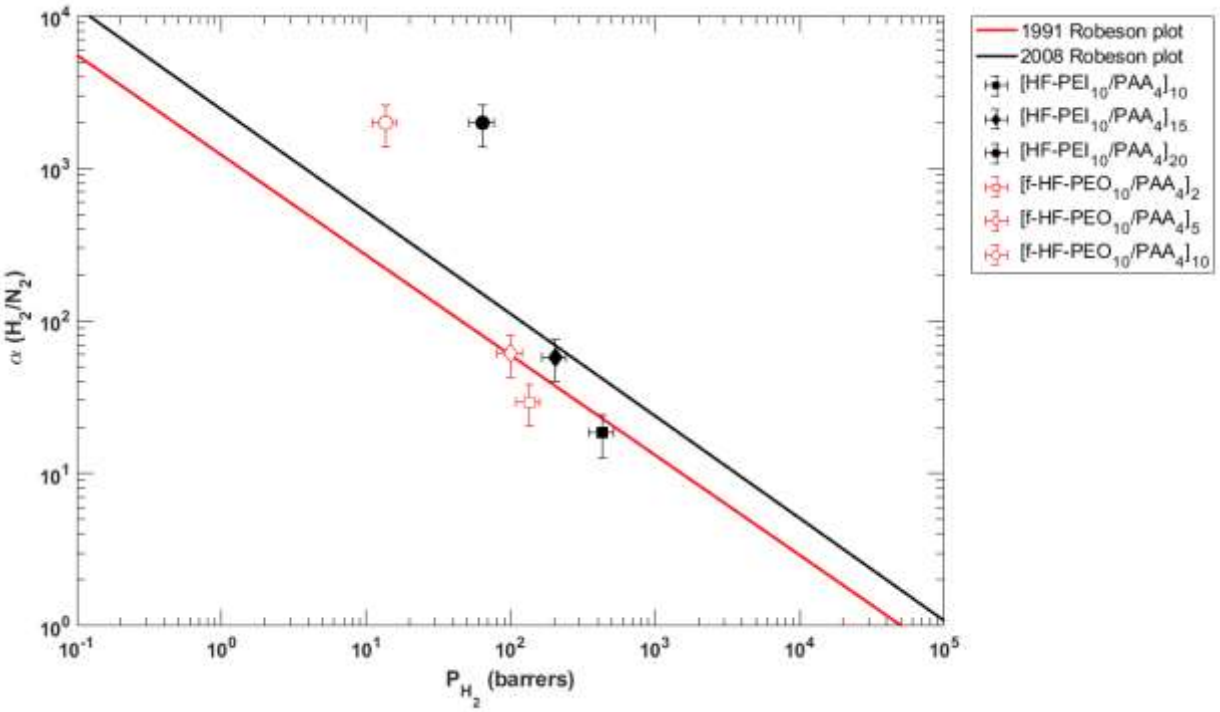


*Figure 2.2-8: Robeson upper bound plots for $H_2/N_2$ gas pair for $[HF\text{-}PEI_{10}/PAA_4]_{10}$, $[HF\text{-}PEI_{10}/PAA_4]_{15}$, $[HF\text{-}PEI_{10}/PAA_4]_{20}$, $[f\text{-}HF\text{-}PEI_{10}/PAA_4]_2$, $[f\text{-}HF\text{-}PEI_{10}/PAA_4]_5$, and $[f\text{-}HF\text{-}PEI_{10}/PAA_4]_{10}$*

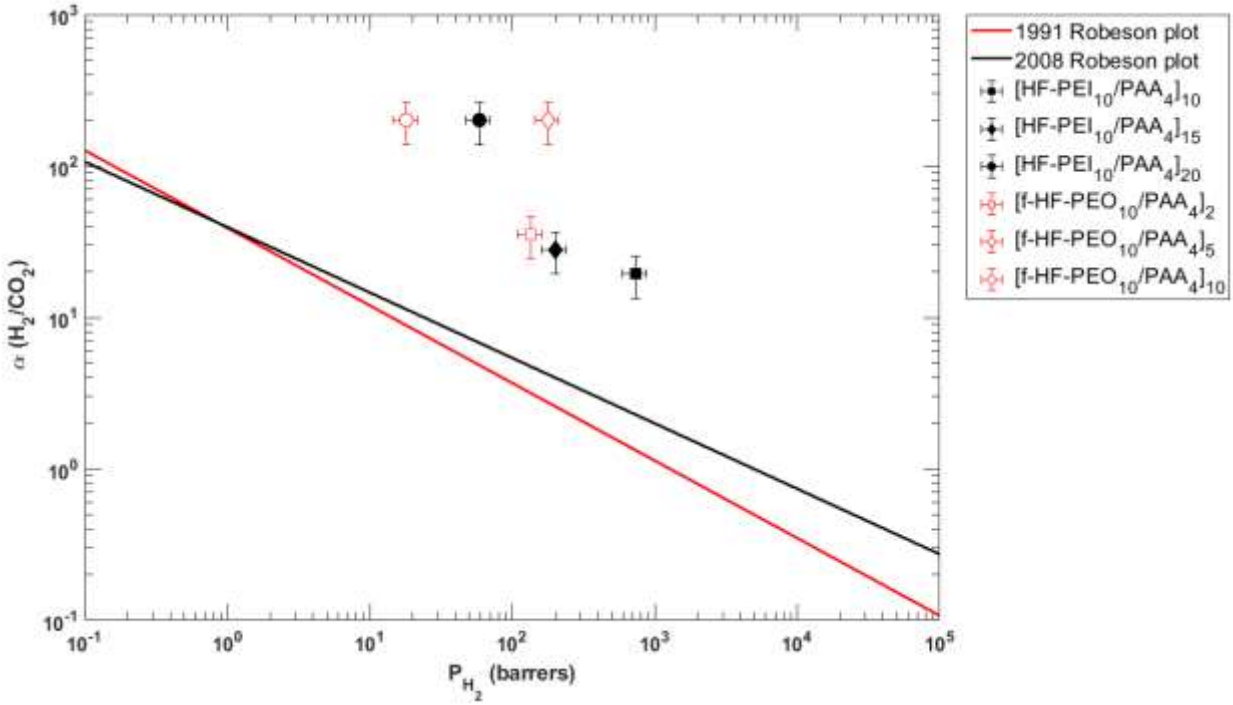


*Figure 2.2-9: Robeson upper bound plots for $H_2/CO_2$ gas pair for $[HF\text{-}PEI_{10}/PAA_4]_{10}$, $[HF\text{-}PEI_{10}/PAA_4]_{15}$, $[HF\text{-}PEI_{10}/PAA_4]_{20}$, $[f\text{-}HF\text{-}PEI_{10}/PAA_4]_2$, $[f\text{-}HF\text{-}PEI_{10}/PAA_4]_5$, and $[f\text{-}HF\text{-}PEI_{10}/PAA_4]_{10}$*

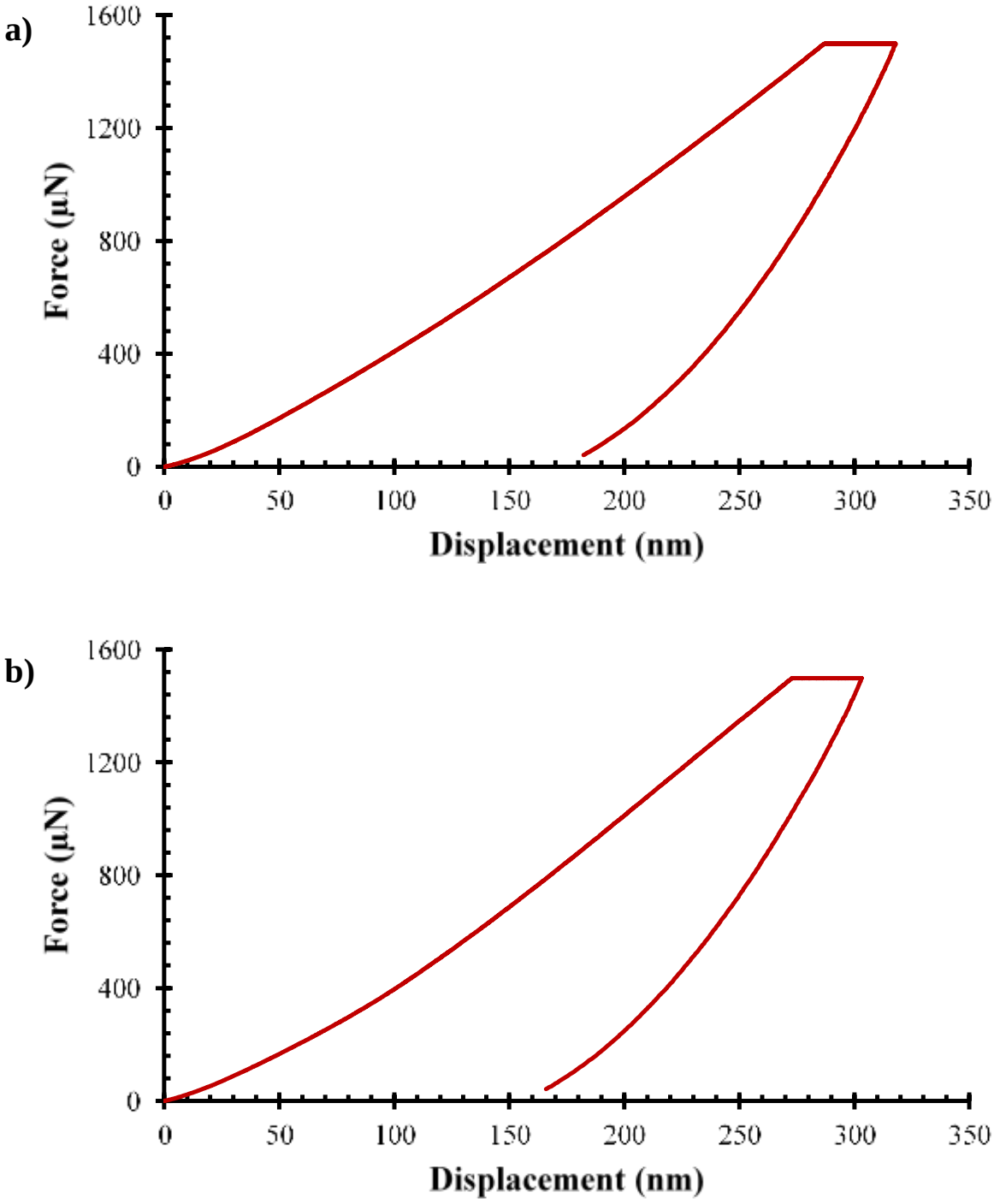


*Figure 2.2-10: Force versus displacement curves from nanoindentation tests performed on 10 bilayers of PEI/PAA assembly coated on a flat sheet Torlon a) neutral hollow fiber, b) functionalized hollow fiber.*

### *2.3.4 Nanoindentation*

The bilayers are too thin to test mechanical properties as free-standing films, hence, nanoindentation was used to measure mechanical properties of 10 bilayers of PEI/PAA films on both neutral hollow fiber and functionalized hollow fiber. Each test was done in load-controlled feedback mode with a quasi-load function with a 5-second loading to a peak force of 1.5 mN followed by a 2-second hold and a 5-second unloading segment. These values were chosen to ensure that the tests were as free as possible from surface roughness and substrate effects. The hardness and elastic modulus were obtained from the loading and unloading curves (Figure 2.2-10).

The LbL membrane system has a compact, dense, and homogenous polymeric structure, as inferred from SEM images and mechanical behavior. The average elastic modulus and hardness of $[HF\text{-}PEI_{10}/PAA_4]_{10}$ measured by nanoindentation analysis on flat Torlon© sheet, are $0.99 \pm 1.10$ GPa and $0.79 \pm 0.11$ GPa, respectively, with comparable values of $11.35 \pm 0.51$ GPa and $0.85 \pm 0.04$ GPa for $[f\text{-}HF\text{-}PEI_{10}/PAA_4]_{10}$, respectively.

## 2.4 Conclusion

In conclusion, this study demonstrates a highly hydrogen-selective membrane deposited on industrial, mass-producible, low cost, high flux, and low selectivity hollow fibers. Also, the surface properties of the substrates play a vital role in the deposition of the LbL membrane which can be enhanced by chemical modification of these substrates.

# 3. Highly Selective Hollow Fiber Membranes for Carbon Capture via in-situ Layer-by-Layer Surface Functionalization *

## 3.1 Introduction

There is a pressing need to reduce anthropogenic $CO_2$ emissions, with an ultimate goal of achieving a carbon-neutral economy.[82-83] The current Intergovernmental Panel on Climate Change (IPCC) recommends drastic measures to limit the rise in average global temperature to below 1.5 $^oC$ relative to the pre-industrial era to avoid frequent heatwaves, heavy rainfall, melting of polar ice, and rising sea levels which might result in loss of life and property.[84] Emissions from fossil fuels remain the largest contributor to rising $CO_2$ levels, with approximately 28% of total greenhouse gas emissions generated by electricity production.[85-86] While electricity production from renewable sources (e.g. solar, wind, and nuclear) continue to rise, fossil fuels are expected to remain the largest contributor to global energy demand for at least another 30 years.[23] Thus, there is a critical need for mitigating the $CO_2$ emission in existing, new, and upcoming power plants.[87-88] Post-combustion $CO_2$ capture is an attractive option, as it can be retrofitted into existing power plants without requiring any major modification of infrastructure.[89-90] Current post-combustion $CO_2$ capture technologies employing gas-liquid absorption and/or pressure swing adsorption are expensive, contributing 70-80% of the total cost of carbon capture and sequestration.[91-92] Over the past two decades, cost-effective membrane technologies for $CO_2$ capture have gained significant attention due to their low energy consumption, small carbon footprint and passive operation.[93]

Homogenous polymeric membranes possess an intrinsic trade-off between permeability and selectivity, while industrial application demands membranes with both high permeance and high selectivity for increased process throughput and product purity.[30] This trade-off was first introduced as an experimentally observed upper bound for homogeneous polymeric membranes by Robeson in 1991 (and a revision in 2008) and theoretically proven by Freeman.[27, 29, 31] Most current research focuses on breaking this upper bound by means of modifying membrane morphology via thermal rearrangement, mixed matrix membrane (MMMs), polymers of intrinsic micro porosity (PIMs), and other approaches.[2, 94] In a typical dense polymeric membrane, gas separation is driven by the pressure difference across the membrane and occurs via solution-diffusion mechanism.[31] The penetrant gas molecule first adsorbs on the upstream side of the membrane, dissolves into the solid phase, then diffuses through the membrane, and finally desorbs on the downside of the membrane. The selectivity of the membrane is therefore dictated by both the relative solubility and diffusivity of each species.

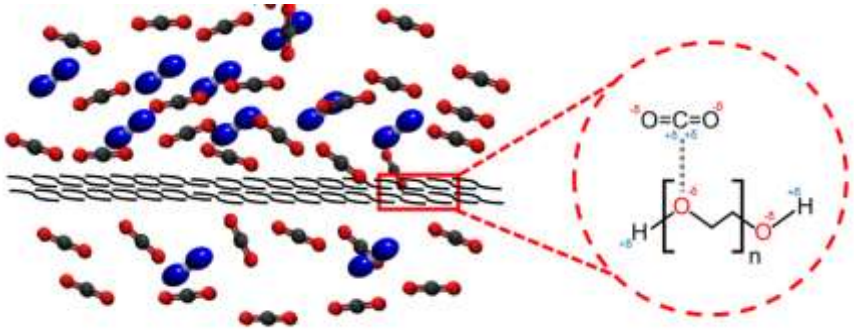


*Figure 2.2-11: A schematic of dipole quadrupole interaction between polyethylene oxide and $CO_2$*

Polymers containing polar moieties, such as the ether group in poly(ethylene oxide) (PEO), have an affinity for $CO_2$ due to the dipole-quadrupole interactions which increase $CO_2$ selectivity (Figure 2.2-11).[95] While PEO-based membranes have been reported with promising $CO_2$ selectivity, their high degree of crystallinity results in low overall gas permeability, as crystalline

regions creates a tortuous pathway for diffusion within the polymer matrix.[96-97] Various strategies have been employed to address this issue, including copolymerization, blending and crosslinking with polyimides or polyamides.[98-99]

Layer-by-layer (LbL) assembly is a powerful technique that allows conformational coating of nanoscale blends from two or more unique polyelectrolytes.[100] LbL has gained significant traction over the past two decades for the fabrication of thin functional films owing to its versatility across a wide range of fields including biomedicine, drug delivery, water purification, solar cells, optics, batteries, gas barriers, and gas separation.[50, 52, 55, 101] LbL is a cyclic process where substrates are dipped alternatively in oppositely charged polyelectrolyte solutions with rinsing and drying steps in between. During each immersion, molecules adsorb, diffuse, and interact with the oppositely charged surface ions resulting in either linear or exponential film growth.[57] This approach provides excellent control of tunability of the resulting thin film structure, composition and material properties by adjusting concentration, pH, temperature, molecular weight, deposition time, and viscosity of the polyelectrolyte solution.[60, 63, 102] LbL assemblies for gas separation thus offer the potential to tune permselectivity and permeability by changing the number of cation-anion deposition (i.e. "bilayers"). Over the past two decades, several LbL films have been studied for gas separation.[57] Stroeve *et al.* deposited 40 bilayers of poly(allylamine) and poly(styrene sulfonate) on polypropylene substrate and 100 bilayers of the same on a dimethyl silicone membrane; $CO_2/N_2$ selectivity up to 24:1 were observed at 70 °C.[39] McCarthy *et al.* reported an increasing trend in selectivity over deposition of 20 to 200 bilayers of poly(allylamine hydrochloride) and polysodium styrene sulfonate on a poly(4-methyl-1-pentene) substrate, however, membrane permeability decreased with increase in the number of bilayers due to formation of rigid and dense structures.[103] Sullivan and Bruening deposited defect-free poly(amic

acid) and poly(allylamine hydrochloride) bilayers on porous alumina, followed by heat induced imidization. These membranes exhibited $O_2/N_2$ and $CO_2/N_2$ selectivity of 6.9 and 68, respectively.[104-105] Kentish *et al.* studied 4 and 2 tri-layers of polystyrene sulfonate, carbonic anhydrase, and poly(allylamine hydrochloride) on poly(propylene) and poly(dimethoxy silane) hollow fiber support resulting in 3-fold increase in $CO_2$ adsorption.[106] LbL assemblies of poly(ethylene oxide) as proton acceptor and either poly(methyl acrylic acid) or poly(acrylic acid) as proton donors have been studied for controlled released applications in drug delivery and Lithium ion conductivity in solid polymer electrolytes.[107-110]

Our research group previously demonstrated highly selective membranes for gas separation using LbL method.[102, 111-115] In a recent work, poly(methacrylic acid) (PMAA) and poly(ethylene oxide) (PEO) bilayers deposited at pH of 2 i.e. [$PEO_2/PMAA_2$], on a dense poly(styrene) substrate was studied for $CO_2/N_2$ separation.[112] This work was able to solve one of the issues with PEO-based membranes by reducing the degree of crystallinity to ~5 %. The combination of reduced crystallinity and high $CO_2$ solubility resulted in one of the highest selectivity (~140:1) reported for homogenous polymeric membranes, albeit at low $CO_2$ permeability of 0.011 Barrer. However, permeabilities were measured separately using pure gas mixtures (owing to the limitation of constant-volume variable-pressure technique), and thus did not consider the effect of plasticization on $CO_2/N_2$ selectivity.[116] Additionally, functional LbL films were deposited on a non-functionalized, dense polymer substrate. Given the performance of this bilayer pair in terms of $CO_2$ selectivity, the present work aims at applying these thin functional films to low-cost, easily manufacturable, and mass-producible hollow fibers with functionalized surfaces to achieve $CO_2$ permselective membranes with competitive permeance.

In this work, we demonstrate LbL deposition of highly selective $PEO_2/PMAA_2$ bilayers hollow fibers capable of achieving both high $CO_2/N_2$ selectivity and $CO_2$ permeabilities for post-combustion carbon capture. The effect of functionalization to create favorable conditions for LbL deposition was also studied. The $CO_2$ selectivity for 5 and 10 bilayers on functionalized hollow fibers and 20 bilayers on hollow fiber support exceeds selectivity values for most of the polymeric membrane. These impressive values can be attributed to the increased solubility of $CO_2$ in the selective layer originated from the favorable PEO and $CO_2$ dipole quadrupole interaction.

## 3.2 Experimental section

### *3.2.1. Materials*

Poly(ethylene oxide) (MW ~4,000,000 g $mol^{-1}$), branched poly(ethyleneimine) (Millipore Sigma) (MW ~25,000 g $mol^{-1}$), and poly(methacrylic acid) (MW ~100,000 g $mol^{-1}$) were purchased from Millipore Sigma. Hydrochloric acid (37% purity) and isopropanol (99.5 % purity) from VWR are used as solvents.

### *3.2.2. Hollow Fiber Fabrication*

Torlon© (PAI) hollow fibers were fabricated using dry-jet wet-quench spinning. A polymer dope was first formed by dissolving Torlon© polymer into 1-methyl-2-pyrrolidone and water. LiCl was added to create a more open porous structure that is desirable in a membrane support. The dope was mixed on a roller for more than one week . The dope solution and bore solutions were pumped using syringe pumps (Teledyne ISCO) through a spinneret, passing through an air gap and into a quench bath of DI water. The hollow fibers were immersed in water for three days to remove any remaining solvent and additives. The fibers were then solvent exchanged by immersion of the fibers for 20 min each in three batches of fresh methanol followed by three batches of fresh n-hexane and dried under vacuum at 70 °C for 3 h. These Torlon HF

supports have an outer diameter of ~600 μm, and a wall thickness of ~150 μm; they are highly permeable to CO2 and N2 with Knudsen selectivity.

### *3.2.3 Membrane Fabrication*

PEO and PMAA solutions with 0.1 wt % and 0.2 wt % loading, respectively, were prepared using deionized water (18.2 MΩ). The pH of the PEO and PMAA solutions were adjusted to 2 by adding 1 M (HCl). For the surface functionalization process, branched PEI and water were mixed with 2-propanol to prepare a solution of 5: 5: 90 by wt %. Hollow fiber surface was functionalized using an IPA-PEI-water solution in an oil-bath setup for 4 hours at 70°C followed by overnight drying.

Neutral hollow fibers were cut in 5 inches length and sealed into shell (0.25-inch diameter) and tube assembly using epoxy and Swagelok compression fittings. This setup was then used for *in-situ* deposition of PEO/PMAA films, which prevented vibrational damage during coating. PEO/PMAA layers are deposited on hollow fiber surface using an iterative process of flowing alternating polymer solutions (5 mins for first bi-layer and 2 mins for the later) with water flushing and air-drying steps each for 30 s. A syringe pump assembly was used to feed PEO and PMAA solutions alternatively to the annulus at 10 mL/min flowrate at ambient conditions. PEO solution is introduced initially to form a positively charged layer over the neutral hollow fiber surface. 10, 15, and 20 bilayers were deposited on hollow fibers to study their permeation behavior and these are denoted as $[HF\text{-}PEO_2/PMAA_2]_{10}$, $[HF\text{-}PEO_2/PMAA_2]_{15}$, and $[HF\text{-}PEO_2/PMAA_2]_{20}$.

For the functionalized hollow fiber, similar set up for *in-situ* deposition of bilayers was prepared. PMAA solution with negative charge was introduced initially to the hollow fiber assembly since the functionalization produces a positively charged surface. The remaining

procedure is same as above. These steps were repeated for 2, 5, and 10 bilayers; denoted as [f-HF-$PEO_2$/$PMAA_2$]$_2$, [f-HF-$PEO_2$/$PMAA_2$]$_5$, and [f-HF-$PEO_2$/$PMAA_2$]$_{10}$.

### *3.2.4 Characterization*

A sessile drop technique was used for contact angle measurements on flat nonfunctionalized and functionalized Torlon© substrate and the data was analyzed using the ImageJ software (National Institutes of Health (NIH), Bethesda, MD, USA). FTIR spectra of Hollow fibers and its functionalized form was collected by making pellets with KBr powder. Surface and cross-sectional images were obtained to confirm defect-free coating on the membrane. Samples were prepared by using liquid $N_2$ to freeze fracture followed by a 5nm platinum coating. Scanning electron microscopy was performed using a JEOL JSM-7500F FESEM (Jeol Ltd, Tokyo, Japan).

A Hysitron TI950 Triboindenter was used to measure the hardness and elastic modulus. The thickness of the selective films is in micron range which makes it challenging to analyze free-standing films to study the mechanical properties, hence, nanoindentation methodology was used to measure hardness and elastic modulus. Samples were prepared by depositing 10 bilayers of PEO/PMAA on both neutral and functionalized Torlon© flat sheet using the procedure described in the methods section. Nanoindentation tests were performed in load-controlled feedback mode with a loading-hold-unloading segment of 5, 2, and 5 seconds each with a peak force reaching up to 1.5mN. These values were considered to avoid any effects from surface roughness and substrate properties. The hardness and elastic modulus values were calculated from the loader and unloading curves.

### *3.2.5 Permeation Study*

The shell and tube assemblies containing each coated hollow fiber were used to measure gas permeabilities at 21 °C and 1 atm outlet pressure. A feed of test gas mixture $N_2$ and $CO_2$ (varied from pure $N_2$ to pure $CO_2$) with a constant overall flowrate of 50 mL/min was fed to the annulus and a sweep gas of argon with a flowrate of 30 mL/min was fed to the bore of the setup as shown in Figure S2. The composition of feed gas mixture was varied from pure $CO_2$ to pure $N_2$ while keeping the overall gas flowrate constant. The permeate i.e., the outlet of the bore hollow fiber (permeate) is connected to a mass spectrometer (RGA 100, Stanford Research Systems) which analyzes composition of gases. The feed gas composition was changed only after the outlet signal from mass spectrometer reaches steady state. The overall permeability is calculated using an observable log mean average driving force for co-current flow configuration via Equation (1)

$$\boldsymbol{F_i = \frac{p_i}{t}\left[\frac{(p_p - p_r)-(p_f - p_s)}{ln\left[\frac{p_p - p_r}{p_f - p_s}\right]}\right]_i} \quad (1)$$

Where, $F_i$ = Flux ($mol\ m^{-2}s^{-1}$) of species $i$

$p_i$ = observed permeance ($mol\ m^{-2}s^{-1}Pa^{-1}$), and

$p_p, p_r, p_s$, and $p_f$ = partial pressure of the permeate, retentate, sweep, and feed side for the species $i$, respectively

The permeability of the selective layer-by-layer film is calculated from overall permeance and substrate permeability using a resistance-in-series model.

$$\frac{1}{p_{bulk}} = \frac{t_{selective\ layer}}{P_{selective\ layer}} + \frac{1}{p_{substrate}} \quad (2)$$

Where, $p_{bulk}$ = overall observed bulk permeance ($mol\ m^{-2}\ s^{-1}Pa^{-1}$) of the membrane,

$p_{substrate}$ = permeance of the substrate used, and

$t_{selective\ layer}$ and $P_{selective\ layer}$= thickness and permeability of the selective layer of the membranes estimated using the scanning electron microscopy images,

Equation 2 is used to calculate the permeability of the selective layers.

Selectivity is calculated using:

$$\alpha_{CO_2/N_2} = P_{CO_2}/P_{N_2} \quad (3)$$

Where, $\alpha_{CO_2/N_2}$= selectivity of $CO_2$ over $N_2$

$P_{CO_2}$= permeability of $CO_2$, and $P_{N_2}$= permeability of $N_2$

This co-current flow configuration facilitates bench-scale measurement of gas permeabilities under mixed-gas conditions, while sweep gas sufficiently dilutes permeate gas composition as to allow accurate determination of steady-state permeabilities in the absence of mixing effects present under concentrated conditions.

## 3.3 Results and Discussion

### *3.3.1 Substrate*

Torlon© based hollow fibers are chemically and mechanically stable due to the presence of amide and imide groups present in the backbone.[117] This also results in a highly hydrophobic surface which impedes bilayer growth requiring multiple initial bilayers to establish favorable conditions for depositing defect-free subsequent layers. Several studies have focused on interaction of polyimides with PEI as a promising approach to introduce a positively charged surface by introducing the amine group from PEI on the membrane surface.[69] Sun *et al.* studied the use of PEI to improve the hydrophilicity of the PAI hollow fiber surface to filter Ciproflaxin

from water stream and Li *et al*. functionalized PAI based hollow fiber to improve carbon dioxide uptake.[73, 118] Similarly, as-received hollow fibers were functionalized using a PEI-water-Isopropanol solution (5:5:90 wt %) to improve the surface hydrophilicity. The primary amine group from the branched PEI attacks the carbonyl (C=O) from the PAI backbone resulting in the opening of imide ring. Comparison of FTIR spectra of untreated and functionalized hollow fiber shows the changes in the structure of PAI after the functionalization reaction . The peaks for imide (C-N) absorbance at 1360 $cm^{-1}$ are missing in the functionalized hollow fiber and the carbonyl (C=O) absorbance peaks at 1750 $cm^{-1}$ and 1730 $cm^{-1}$ are weaker when compared to neutral hollow fibers. The changes in the backbone and the presence of amine group introduces positive charge on the surface improving the hydrophilicity, as confirmed by contact angle measurement. The contact angle of the hollow fiber surface decreases from $102^{o}$ to $68^{o}$ after functionalization. This improvement in hollow-fiber surface wettability in turn facilitated uniform, defect free coatings using aqueous polyelectrolyte solutions via layer-by-layer technique.[115]

### *3.3.2 Functional Layer*

The ether groups present in PEO act as H-bond acceptor and the carboxylic acid groups in the PMMA act as H-bond donors which enables hydrogen bonding between the layers. The LbL process is dependent on the pH of polyelectrolyte solutions and the stability of interpolymer complexes. The stability of interpolymer complexes is dependent on a critical pH which results in phase separation and it precipitates from the solution.**[119]** Sukhishvili and Granick have reported that in the PEO/PMAA system the multilayer films are stable below pH value of 4.6.**[109]** The influence of polyelectrolyte pH of PEO/PMAA system on membrane performance was studied previously (for pH values 2, 2.5, and 3) with pure $CO_2$ permeability unaffected by pH while the $N_2$ permeability was minimized at a pH of 2.**[112]** The carboxylic groups in PMAA are fully

protonated at pH ≤ 2 providing maximum sites for interaction with PEO.[120] The deposition of LbL films on both untreated and functionalized hollow fibers followed exponential growth, which results from charge overcompensation by diffusive penetration of the polyelectrolyte through the multilayer film.[109-110, 121-122] This diffusive penetration of PEO during each deposition cycle not only results in exponential growth but also result in increase in PEO content owing to the higher mobility of PEO molecule over PMAA molecule, as confirmed by several studies using solid state $C^{13}$ nuclear magnetic resonance.[123-126]

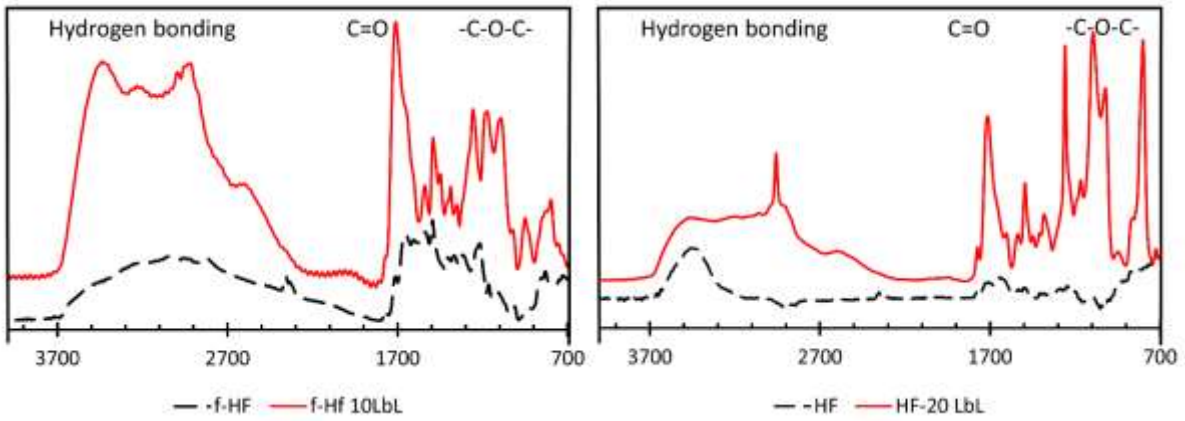


Figure 2.2-12: *FTIR spectra of support and membrane; a) functionalized hollow fiber support with 10 layers of PEO/PMAA; b) hollow fiber support with 20 bilayers of PEO/PMAA*

Fourier-transform infrared (FTIR) spectra were collected to confirm the presence of hydrogen bonding, C-O-C stretch, C=O stretch, and $CH_2$ peaks. Figure 2.2-12 shows FTIR spectra of 10 bi-layers of PEO/PMAA on functionalized hollow fiber and 20 bi-layers of PEO/PMAA on hollow fibers and their respective substrates. These FTIR spectra confirm the presence of functional groups related to PEO and PMAA; peaks at 820, 1030-1110, and 1120-1170 $cm^{-1}$ are similar to C-O-C stretch and -$CH_2$ peaks reported for amorphous PEI.[127] The absorption between 1700 and 1750 $cm^{-1}$ is from carbonyl bond stretching, commonly observed for carboxylic acid similar to PMMA. Hydrogen bonding between the layers is indicated by a broad absorption peak at ~3000 $cm^{-1}$. The intensity of hydrogen bonding peak for the 10 bilayers of PEO/PMAA on

functionalized hollow fiber support showed higher intensity confirming our hypothesis that functionalization improves the support surface condition, in turn increasing interactions between layers as well as between the initial layers and the support. The ratio of C-O-C (from both PEO and PMMA) over C=O (from PMMA increases from 0.32 to 1.46 for 10 bilayers of $PEO_2/PMMA_2$ to 20 bilayers which confirms the hypothesis that PEO content increases as number of bilayers are deposited.

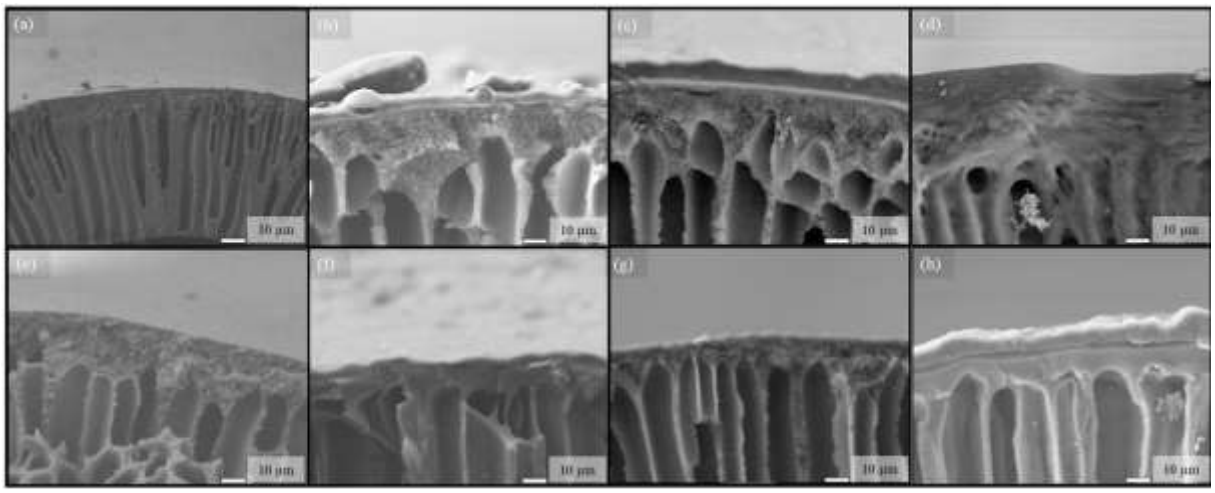

*Figure 2.2-13: Scanning electron microscope image of cross-section of (a) hollow fiber, (b) $[HF\text{-}PEO_2/PMAA_2]_{10}$, (c) $[HF\text{-}PEO_2/PMAA_2]_{15}$, and (d) $[HF\text{-}PEO_2/PMAA_2]_{20}$, (e) functionalized hollow fiber, (f) $[f\text{-}HF\text{-}PEO_2/PMAA_2]_2$, (g) $[f\text{-}HF\text{-}PEO_2/PMAA_2]_5$, and (h) $[f\text{-}HF\text{-}PEO_2/PMAA_2]_{10}$*

Cross-section scanning electron microscopy images of hollow fibers confirm the presence of a dense functional coating on each substrate (Figure 4). The coating thickness for 10 bilayers on functionalized hollow fibers (4.77 μm) is roughly 1.6 times that for the same number of bilayers deposited on neutral hollow fiber. Functionalization of support creates a favorable condition for the subsequent layers to grow due to the presence of a positively charged surface.

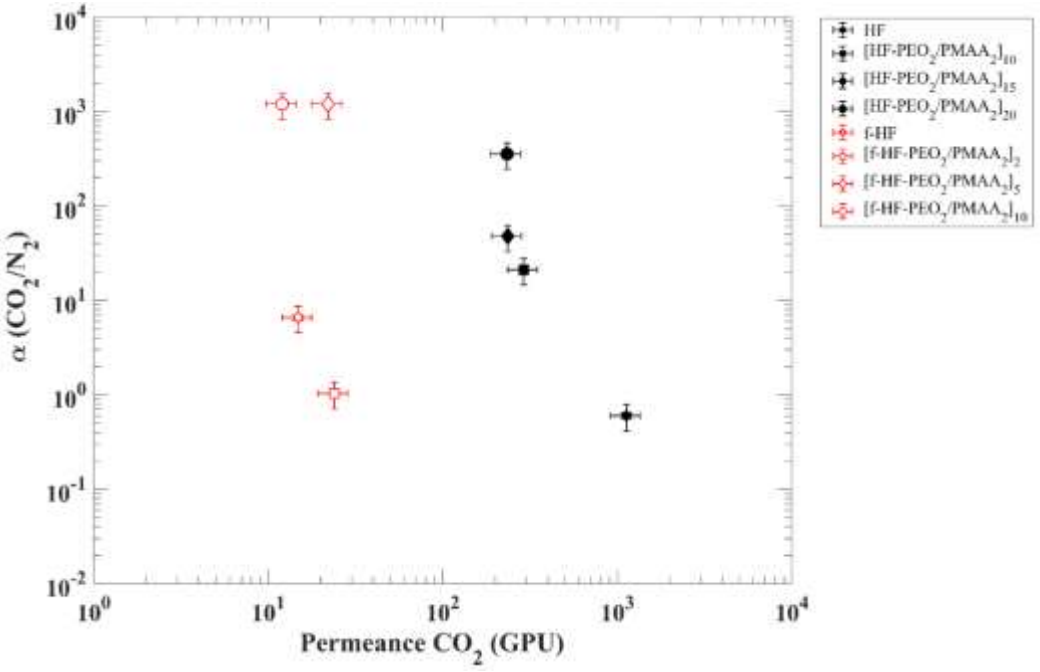


*Figure 2.2-14: Selectivity of $CO_2$ over $N_2$ vs $CO_2$ Permeance for $CO_2/N_2$ gas pair for hollow fiber, $[HF\text{-}PEO_2/PMAA_2]_{10}$, $[HF\text{-}PEO_2/PMAA_2]_{15}$, $[HF\text{-}PEO_2/PMAA_2]_{20}$, functionalized hollow fiber, $[f\text{-}HF\text{-}PEO_2/PMAA_2]_2$, $[f\text{-}HF\text{-}PEO_2/PMAA_2]_5$, and $[f\text{-}HF\text{-}PEO_2/PAA_2]_{10}$*

### *3.3.3 Permeation result*

Initial $N_2$ and $CO_2$ gas transmission rates for uncoated hollow fiber support were analyzed before any layer deposition or functionalization with observed $N_2$ and $CO_2$ permeances of 7561 GPU and 8341 GPU, respectively. The hollow fibers are highly porous in nature, and thus gases follow Knudsen diffusion with a selectivity of $CO_2$ over $N_2$ of ~ 1.1. Figure 2.2-14 presents the $CO_2/N_2$ selectivity vs $CO_2$ permeance values for 10, 15, and 20 bilayers on hollow fiber support and 2, 5, and 10 bilayers on functionalized hollow fiber support. The $CO_2$ permeance for the membranes decreases slightly with increase in number of bilayers of $PEO_2/PMAA_2$ on hollow fibers, however, the nitrogen permeance decreases significantly resulting in an increase in selectivity of $CO_2$ over $N_2$. The kinetic diameter of $N_2$ (3.64 Å) and $CO_2$ (3.3 Å) are very similar;

the results confirm our hypothesis that the presence of dipole-quadruple interaction between PEO and $CO_2$ creates a favorable condition for $CO_2$ transport.

Similarly, for 2, 5, and 10 bilayers of PEO/PMAA on functionalized hollow fibers, the CO2 permeance of the membranes was almost the same and the selectivity increases with an increase in the number of bilayers. The $N_2$ permeate pressure remained below the detection limit for the case of 5 and 10 bilayers and the selectivity values are calculated on the basis of the minimum detection limit of the mass spectrometer. The permeance of hollow fiber after functionalization decreased significantly; this may be attributed to change in $CO_2$ adsorption after functionalization as reported by Koros et al. which creates resistance for $CO_2$.[118] High magnification scanning electron microscope images of hollow fibers show a change in pore structure and FTIR and contact angle measurement shows the change in the backbone of the hollow fibers.[115] The drastic improvement in the selectivity values for 5 and 10 bilayers can be attributed to the favorable conditions developed at the interface due to the functionalization of the hollow fiber.

*Figure 2.2-15* compares the performances of $PEO_2/PMAA_2$ LbL films on hollow fibers and functionalized hollow fiber support with the Robeson upper bounds for $CO_2/N_2$ gas pair with homogenous polymeric membranes (**Table 1)**. The blue dots are data points for various other homogeneous polymer membranes collected from the Membrane Society of Australasia database.[128] The 5 and 10 bilayers on functionalized hollow fiber support and 20 bilayers on functionalized hollow fiber support exceed all $CO_2/N_2$ selectivity. Based on the discussion from section 3.2, it can be hypothesized that exponential growth and better PEO diffusion results in the increase of PEO concentration over increase in the number of bilayers. Thus, increase in bilayers improves $CO_2$ solubility which in turn enhances $CO_2$ permeability as well as $CO_2$:$N_2$ selectivity.

The performance of the membranes can be tailored by manipulating the interaction in between the alternate layers and between the substrate and selective films.

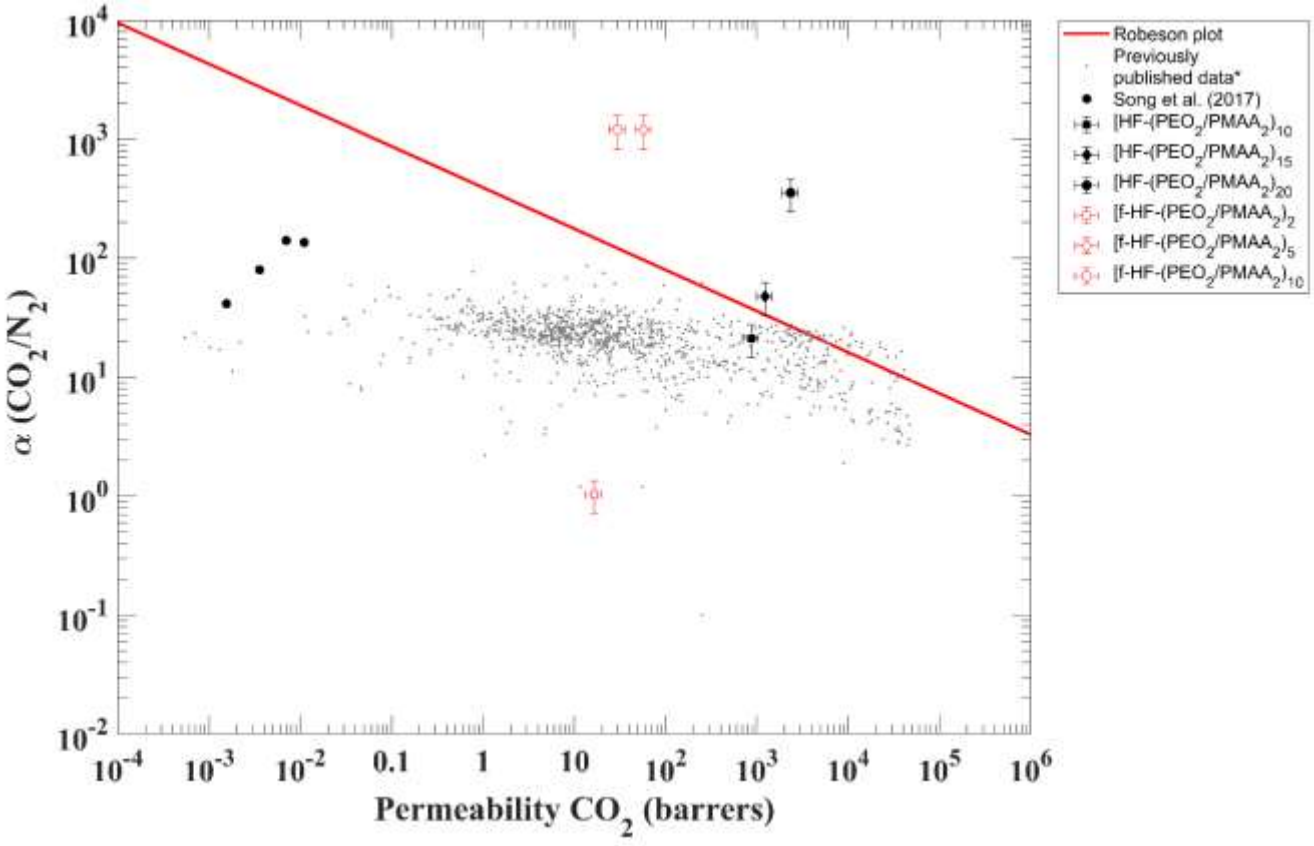


*Figure 2.2-15: Selectivity of $CO_2$ over $N_2$ vs $CO_2$ Permeability on Robeson plot for $CO_2/N_2$ gas pair for hollow fiber, $[HF\text{-}PEO_2/PMAA_2]_{10}$, $[HF\text{-}PEO_2/PMAA_2]_{15}$, $[HF\text{-}PEO_2/PMAA_2]_{20}$, functionalized hollow fiber, $[f\text{-}HF\text{-}PEO_2/PMAA_2]_2$, $[f\text{-}HF\text{-}PEO_2/PMAA_2]_5$, $[f\text{-}HF\text{-}PEO_2/PAA_2]_{10}$, and comparison with previously published data*[112, 128]

These membranes have a uniform, compact, conformal, dense, and homogenous structures depicted from their mechanical behavior and high magnification scanning electron microscope images. The maximum displacement of nano indenter tip was in between 500-600 nm, and the average elastic modulus and hardness of 10 bilayers of $[PEO_2/PAA_2]$ on flat Torlon© sheet was measured by nanoindentation analysis, are $6.03 \pm 1.32$ GPa and $0.24 \pm 0.12$ GPa, respectively,

with comparable values of 6.50 ± 1.32 GPa and 0.26 ± 0.09 GPa for [f-HF-$PEO_2/PAA_2$]$_{10}$, respectively.

**Table 2: $CO_2/N_2$ permeance, selectivity, and thickness of $PEI_{10}/PAA_4$ bilayers on hollow fibers and functionalized hollow fibers**

| Membranes | Thickness [microns] | Permeance $CO_2$ [GPU][a] | Permeance N2 [GPU][a] | $CO_2/N_2$ Selectivity |
|---|---|---|---|---|
| **HF** | --[b] | 1126.8 | 171.1 | 6.6 |
| **[HF- $PEO_2/PAA_2$]$_{10}$** | 2.9 ± 0.1 | 117.6 | 12.4 | 28.1 |
| **[HF- $PEO_2/PAA_2$]$_{15}$** | 5.2 ± 0.7 | 105.7 | 1.0 | 106.3 |
| **[HF- $PEO_2/PAA_2$]$_{20}$** | 10.0 ± 0.6 | 101.5 | 0.4 | 239.4 |
| **f-HF** | --[b] | 14.8 | 23.0 | 0.6 |
| **[f-HF- $PEO_2/PAA_2$]$_2$** | 0.7 ± 0.1 | 23.9 | 23.1 | 1.0 |
| **[f-HF- $PEO_2/PAA_2$]$_5$** | 1.4 ± 0.2 | 24.2 | --[c] | >1100[d] |
| **[f-HF- $PEO_2/PAA_2$]$_{10}$** | 4.7 ± 0.7 | 12.8 | --[c] | >1100[d] |

[a] (Gas Permeation Unit); [b](substrate); [c](below the detection limit) [d](based on minimum detection limit of mass spectrometer)

## 3.4 Conclusion

This work reports for the first time the successful layer-by-layer (LbL) deposition of a PEO/PMAA membrane on hollow fiber support, with $CO_2/N_2$ selectivity of 28-240 at permeabilities of 350-1018 with [HF-$PEO_2/PMAA_2$]$_{20}$ i.e., 20 bi-layers on neutral hollow fiber displaying a permeance of ~101 GPU at a selectivity of ~240. After the addition of 20 bilayers of PEO/PMAA on hollow fiber substrate, the selectivity of $CO_2/N_2$ exceeded the Robeson upper bound for homogenous polymeric films. The hollowfiber support is made from commercial

polymeric material with standard spinning process and the LbL technique also utilizes commercial polymers with dipping procedure that is easily scalable. The cost of fabricating these membranes is expected to be comparable to the commercially available membranes. In conclusion, the LbL technique on low-cost and mass-producible hollow fiber substrate thus has significant potential for carbon dioxide capture in power plants and refinery flue gases.

# 4. Highly selective laser-induced graphene (LIG)/polysulfone composite membrane for hydrogen purification*

## 4.1 Introduction

There is a growing demand for inexpensive and high purity hydrogen for sustainable use of fossil fuels and the emerging hydrogen economy.[40-42, 44-45] The demand for hydrogen in desulfurization and denitrification of hydrocarbon fuels processes continues to grow as increasingly sour resources remain available, whereas the use of ultra-high purity hydrogen in semiconductor processing and fuel cell applications is expected to rise.[10, 129-131] Currently, 95% of hydrogen is produced by steam reforming or combustion of hydrocarbon sources followed by separation of hydrogen from carbon dioxide.[132] The current techniques for hydrogen separation use pressure-swing adsorption and cryogenic distillation; both of which are complex relative to a passive membrane, costly at smaller scale, and has limited modularity for distributed processing.[14] Membranes offer advantages over existing gas separation technologies in terms of low cost, low energy usage, and ease of operation.[47] Over the decades, a large number of highly perm-selective membranes have been developed, but their industrial application has been limited by the cost, scalability, and reliability of membranes.[93]

Porous membranes with uniform nanochannels like graphene nanosheets, graphene oxide, zeolites, and molecular organic frameworks (MOFs) follow the molecular sieving mechanism and have shown promising gas separation performance. Porous membranes with uniform nanochannels like graphene nanosheets, graphene oxide, zeolites, and molecular organic

* Reprinted with permission from (Naveen K. Mishra, Nutan Patil, Muhammad Anas, Xiaofei Zhao, Benjamin A. Wilhite, and Micah J. Green, Highly selective laser-induced graphene (LIG)/polysulfone composite membrane for hydrogen purification. Applied Materials Today, Volume 22, March 2021, 100971 https://doi.org/10.1016/j.apmt.2021.100971 ) Copyright 2020 Published by Elsevier

frameworks (MOFs) follow the molecular sieving mechanism and have shown promising gas separation performance. Several published works have focused on utilizing the uniform pore size, functional materials, and separation properties of MOFs for a variety of gas separation applications.[133-135] Graphene and Graphene oxide-based membranes have reported exceptionally high selectivity for $H_2$:$CO_2$ gas pair owing to the interlayer spacing of these 2-D materials. Li *et al.* studied structural defects and interlayer spacing between graphene sheets for nanometer thickness GO and reduced GO membranes for hydrogen separation; with selectivity values of 3400 for $H_2/CO_2$ were reported.[20] Koenig *et al.* studied atomic layer thick graphene membranes where a UV oxidative etching technique was used to create pores in micrometer sized graphene membranes.[26] However, most of these techniques involve chemical and physical steps for synthesis of graphene and are limited by their mechanical integrity, scalability, and economic feasibility.

Dense polymeric membranes have an intrinsic trade-off between selectivity and permeability based on the kinetic diameter of the gases involved; these membranes rely on the solution diffusion mechanism, and the separation of gases occurs because of the difference in the flux through the membrane.[27] This intrinsic trade-off between selectivity and permeability is shown in a Robeson plot with an upper bound for homogeneous polymeric size-selective membranes whose slope correlates to the kinetic diameter of each gas species.[27, 48] In efforts to improve the upper bounds for polymeric membranes, mixed matrix membranes have been developed by blending nanoporous membrane materials (e.g. zeolites, silicon oxide, graphene oxide, carbon nanotubes) into the dense polymer. However, these methods are often limited by incompatibility between the polymer and nanoporous materials which leads to non-selective void formation. [12-136

Laser-induced graphene (LIG) shows promise as a membrane component because of its ease of production and scalability. LIG is fabricated when the surface of a polymer substrate is photothermally converted to graphene containing carbon material using a $CO_2$ laser.[137-138] Laser processing offers certain advantages over traditional graphene production techniques including Hummer's method and chemical vapor deposition;[139-141] laser processing is a rapid, robust, and inexpensive way to produce LIG on polymer surfaces. [142-146] The quality of LIG can be controlled using power and speed parameters of the $CO_2$ laser, both of which control how much energy is exposed to the sample during laser contact.[147] Laser power determines the amount of energy that the sample is exposed to per second at a single laser contact point and directly affects the depth at which graphitic material is formed at each contact point. The speed of the laser controls the amount of time that the laser is engaged with the sample at any given contact point; thus, lower speed means higher contact time and more energy supplied. The points per inch (PPI) corresponds to the number of laser spots exposed per inch, it controls the spacing between laser contact points and the amount of LIG formed per unit area.[148] In the past few years, LIG has been studied for its potential application in supercapacitors, electrocatalysts, sensors, adsorbents, antibacterial purposes, and composites. [143, 147, 149-154] Singh *et al.* used LIG fabricated on polysulfone polymers for ultrafiltration membranes for antimicrobial and antifouling purposes.[155]

This manuscript reports LIG on polysulfone film as a candidate material for gas separation membranes. LIG on 100 µm thick polysulfone substrate using optimal laser parameters (80 mm/s speed, 9.8 W, 250 PPI) is used for separation of light gas pair $H_2/CO_2$ at room temperature and 1 atm pressure. The composition of gases is varied from 0 to 1 mole fraction for the gas pair, and the permeance values are calculated using a linear fit between flux and partial pressure difference values. The data indicates that this combination is a high perm-selectivity membrane with an

$H_2$:$CO_2$ selectivity of 30.5 ± 1.4 and $H_2$ permeance of 176.4 ±19.5 GPU as compared to neat polysulfone with an $H_2$:$CO_2$ selectivity of 1.87 and permeance of 0.19 GPU.

## 4.2 Experimental

### *4.2.1 Materials*

Polysulfone films (25 µm and 100 µm thickness, Goodfellow USA), hydrogen (99.99% purity), carbon dioxide (99.99% purity), and argon (99.99% purity) were used.

### *4.2.2 LIG fabrication*

For the generation of LIG on polysulfone substrate, a 10.6 µm continuous $CO_2$ laser with 65 W maximum power and 2-inch lens was used. The laser was defocused by 4 mm from its actual focus i.e., the laser was moved an additional 4 mm away from the polymeric film. The spot size of the laser at focus is 0.13 mm and the depth of focus is 2.54 mm. Thus, the spot size of the laser at defocus of 4 mm was calculated to be 0.277mm. The laser is equipped with an air nozzle adjacent to the laser tip which is used to prevent warping of polymeric film. LIG is formed in ambient air condition and at room temperature. The speed, power, and resolution of laser is varied to allow LIG formation on polymeric substrate.

### *4.2.3 Characterization*

The LIG-polysulfone samples were studied under optical microscope. SEM images were taken on surface and cross-section of LIG using a FE-SEM instrument to study the surface characteristics and thickness of membrane. The LIG sample was sputter coated with 5 nm Pt coating. XRD was conducted on the sample using 1.8 $^{\circ}$/min scan rate. TGA analysis was performed on the LIG under air and nitrogen conditions at a temperature ramp rate of 5 $^{o}$C/min. XPS analysis was performed on neat polysulfone and LIG/polysulfone film using spectral scan and studying

individual C12 and S2p peaks. A peak deconvolution was performed to understand the bonds present in neat polysulfone vs. LIG/polysulfone. TGA analysis was also performed on the LIG powder at 5 $^{o}$C/min temperature ramp rate up to 800 $^{o}$C under nitrogen and air conditions. Modulated DSC and TGA analysis were performed on polysulfone before and after laser treatment. GPC analysis was used to track change in molecular weight of polymer after the laser process.

### *4.2.4 Permeation Test:*

Defect-free LIG membranes were tested using a permeation cell set up with constant volume variable pressure technique for quantifying membrane permeabilities with the porous LIG interface facing the feed side. The film to be studied is mounted in a 19 mm filter holder made in house using TAMU facilities and only permeate volumes are subsequently flushed with inert gas. Argon sweep gas (99.998% purity) was supplied to the permeate side (30 ml/min), while a feed gas mixture of $CO_2$ + $H_2$ (50 ml/min) at different composition was supplied to the feed side. Both pure-gas and binary gas mixtures are provided by gas mixing panel equipped with digital flow controllers for precise measurements of feed composition. The permeate is continuously monitored via mass spectrometer (RGA 100, Stanford Research Systems). The feed gas compositions were varied only after the outlet signal of the mass spectrometer reaches a steady state (typically 10 minutes) for the previous feed gas composition. Membrane permeability can be calculated from the slope of the linear region of permeate pressure data which includes gas flux and partial pressure difference.

## 4.3 Results and discussion

Polysulfone films were chosen as a model substrate, as they are well-known for their toughness and high-temperature stability and are thus commonly used for membrane applications in ultrafiltration and gas separation.[156-159] The polysulfone film is irradiated with a $CO_2$ laser to form LIG as shown in Figure 2.2-16A and optimal laser spot focus, speed, power, and resolution were selected to form defect free membranes. The LIG/polysulfone sample contains porous graphene, LIG/polysulfone interface, and polysulfone substrate (Figure 2.2-16B).

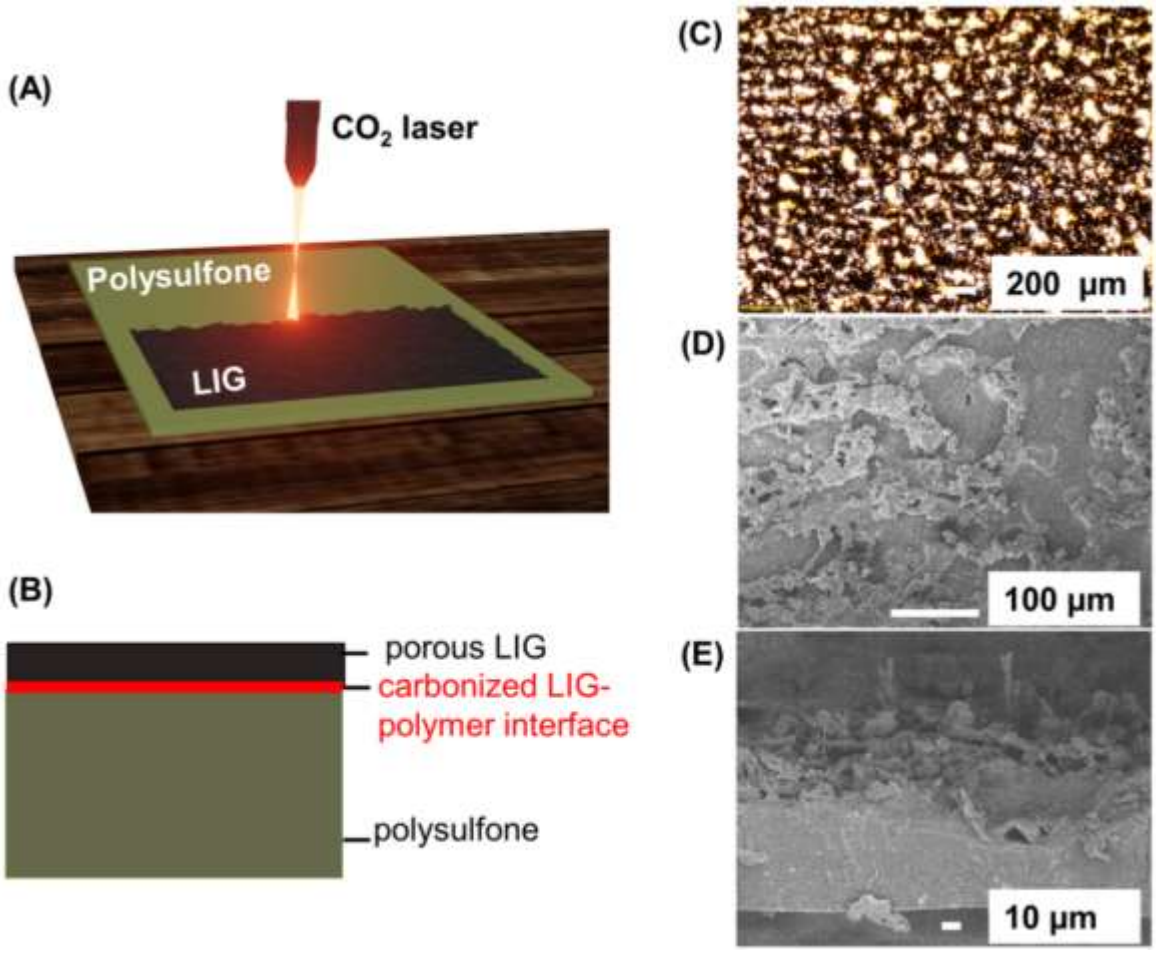


*Figure 2.2-16: (A) Schematic of $CO_2$ laser set up used to make LIG on polysulfone film. (B) Schematic of cross-section of LIG/polysulfone membrane. (C), (D), & (E) Optical image, cross-sectional and surface SEM images of LIG/polysulfone.*

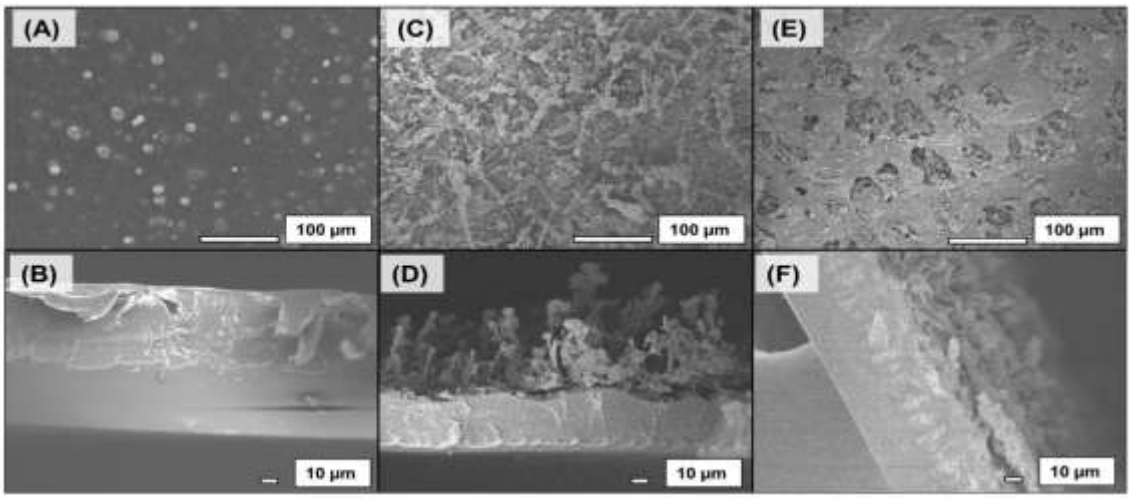


*Figure 2.2-17: SEM image of cross section and surface of (A) and (B) polysulfone film;(C) and (D) LIG2; (E) and (F) LIG3.*

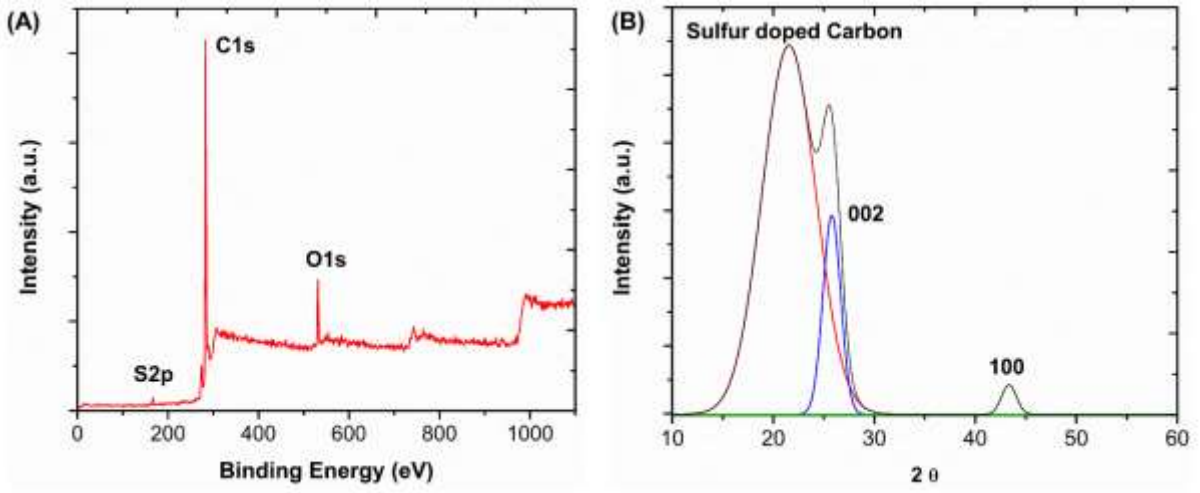


*Figure 2.2-18: (A)XPS survey for LIG/polsyulfone showing presence of sulfur, carbon, and oxygen, (B) Peak deconvolution for XRD data of LIG1.*

Optical microscopy and Scanning Electron Microscopy (SEM) were used to characterize the LIG layer formed on the polysulfone substrate. Figure 2.2 16C shows an optical image of the LIG/polysulfone surface where the darker parts represent the LIG and the lighter parts correspond to the underlying polymeric film that was not converted to LIG during the laser etching process.

SEM images of LIG/polysulfone film shows porous LIG formation on the polymeric surface in Figure 2.2 16D. The cross-sectional images show the thickness of polymer and LIG foam.

Figure 2.2 17 shows SEM images of neat polysulfone film and its surface before LIG formation. X-ray Photoelectron Spectroscopy (XPS) shows surface elemental composition, electronic state, and bonds present on the surface. XPS data on LIG/polysulfone shows that 3 peaks at ~285.5 eV, ~534 eV, and ~167 eV which correspond to C1s, O1s, and S2p peaks as shown in Figure 2.2-18.

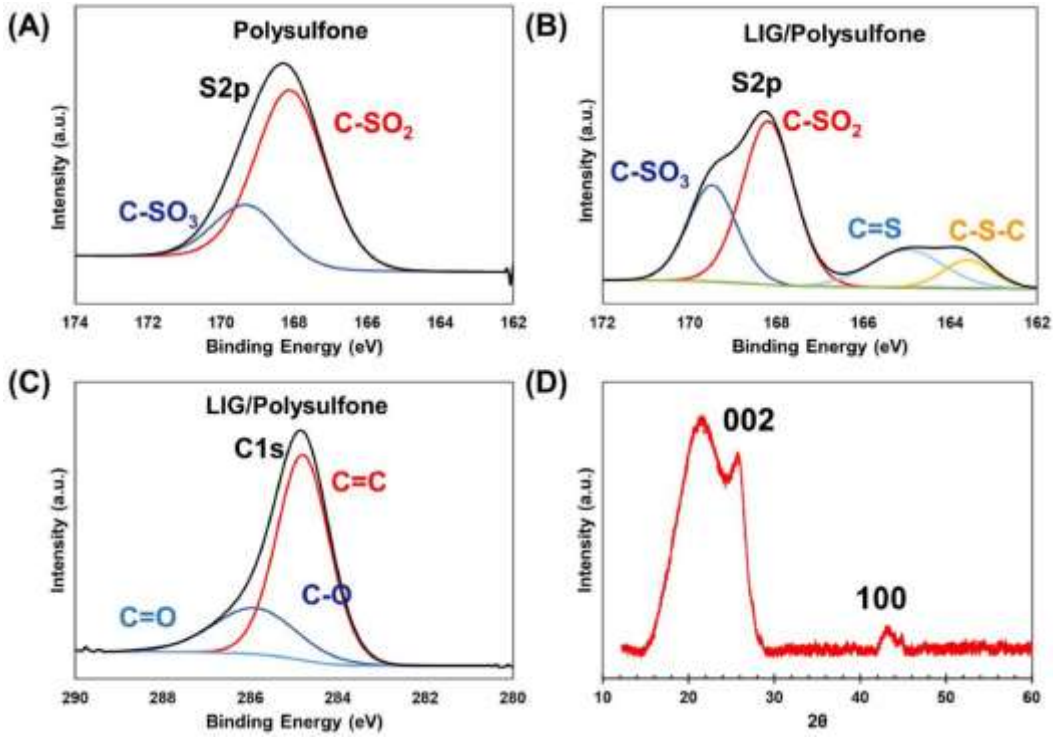


*Figure 2.2-19: (A) and (B) S2p peaks for polysulfone and LIG, respectively; (C) C1s peak for LIG, and (D) XRD data on LIG powder made on polysulfone.*

A peak deconvolution was performed on C1s and S2p peaks, and the data show details of bonds present on the surface. The C1s peakwas deconvoluted to identify C=O, C-O, and C=C bonds; a high C=C bond indicates a high level of graphitization. The S2p peak of LIG/polysulfone shows two kinds of bonds: C-$SO_x$ and C-S at 168.5 eV and 164 eV, respectively, whereas the

polysulfone has only C-$SO_x$ peak.. This again shows that the LIG process photothermally reduced some of the C-$SO_X$ bonds in polysulfone to C-S bonds. The X-Ray Diffraction (XRD) data for LIG powder shows graphene peaks between $10^o$ to $60^o$ 2θ values. Peak deconvolution shows a 002-plane peak at $25.77^o$ and a peak at $21.72^o$ due to sulfur functionalized groups similar to other published works.[160-162] The 002 peak indicates the graphitization during the LIG formation and the interlayer spacing of 0.34 nm. The peak at $43.9^o$ corresponds to 100 plane and is associated with an in-plane structure. The crystal sizes ($L_c$) along the 'c' axis and domain size along the 'a' axis ($L_a$) are 5.27 nm and 10.89 nm respectively calculated using Scherrer equation. Thermogravimetric analysis (TGA), differential scanning calorimetry (DSC), and gel permeation chromatography (GPC) on polysulfone (before and after laser treatment) suggests minimal thermal degradation or chemical changes in the polymer. Wide angle X-ray Diffraction (WAXD) analysis of the polysulfone before and after laser treatment indicate change in the interchain distance (d-spacing) of the polysulfone film (Figure 2.2-22).

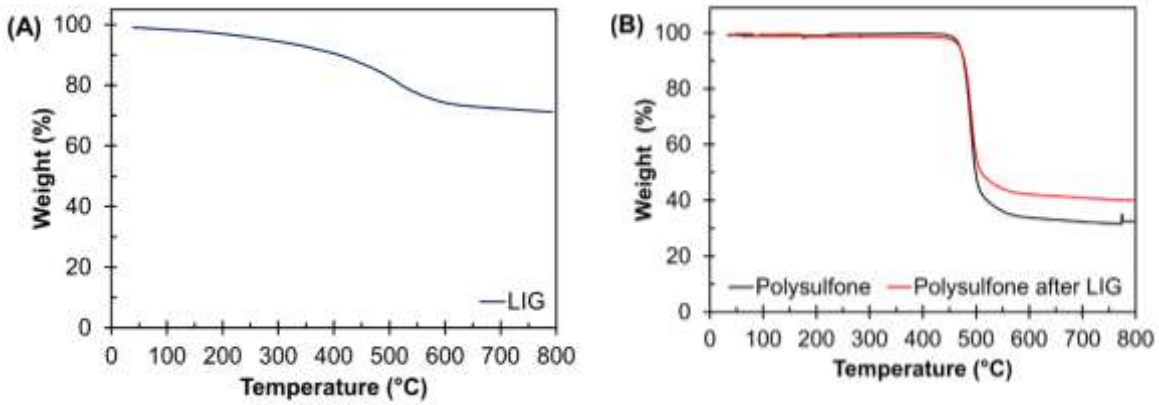


*Figure 2.2-20: TGA data for (A) LIG, (B) polysulfone before and after laser treatment, under nitrogen at 5ºC/min ramp rate.*

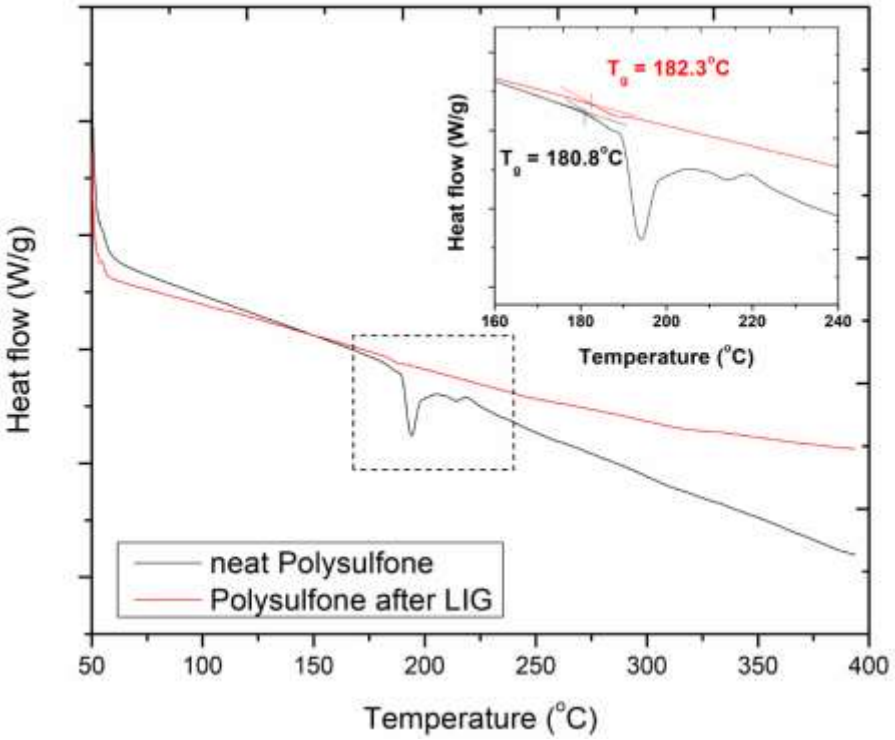


*Figure 2.2-21: Modulated DSC of neat polysulfone film and polysulfone after LIG formation*

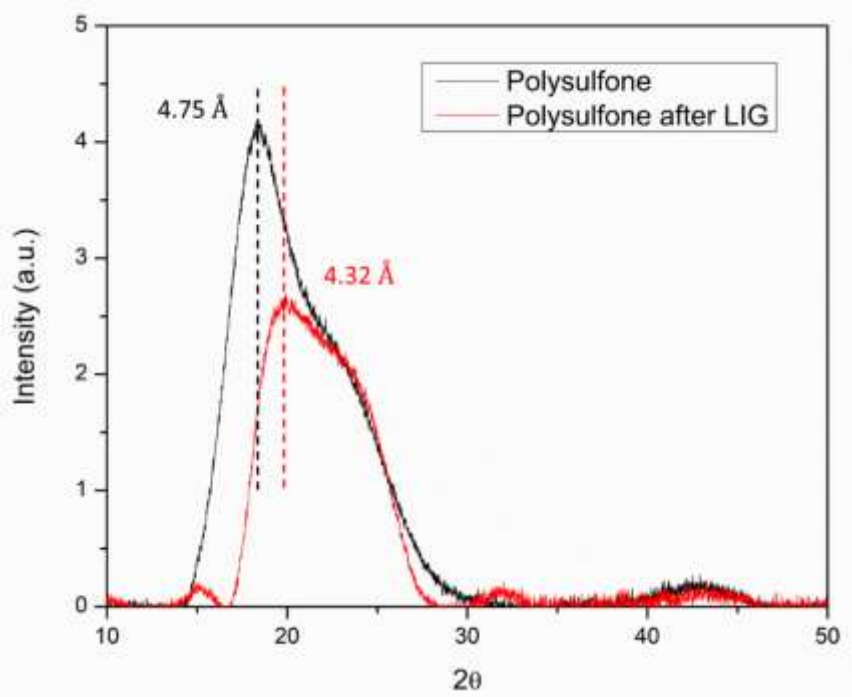


*Figure 2.2-22: Wide angle X-ray diffraction (WAXD) analysis of polysulfone before and after laser treatment indicating change in the d-spacing of the inter-chain distance.*

A schematic of a crossflow gas separation setup used to test the LIG/polysulfone membrane is shown in Figure 2.2-23. All experiments were performed at room temperature (~21 °C) and atmospheric pressure. The feed composition of gases was varied from 0 to 1 mole fraction. For the present case, the overall observed permeance can be calculated using Equation (1)

$$F_i = P_i . \Delta p_i \qquad (1)$$

where $F_i$ is the measured permeation rate (mol $m^{-2}$ $s^{-1}$) of species *i*, $P_i$ is the permeance (mol $m^{-2}$ $s^{-1}$ $Pa^{-1}$) and $\Delta p_i$ is the partial pressure difference (Pa). Gas selectivity of gas i over j ($\alpha_{i,j}$) is given by the ratio of their respective permeances ($P_i/P_j$).

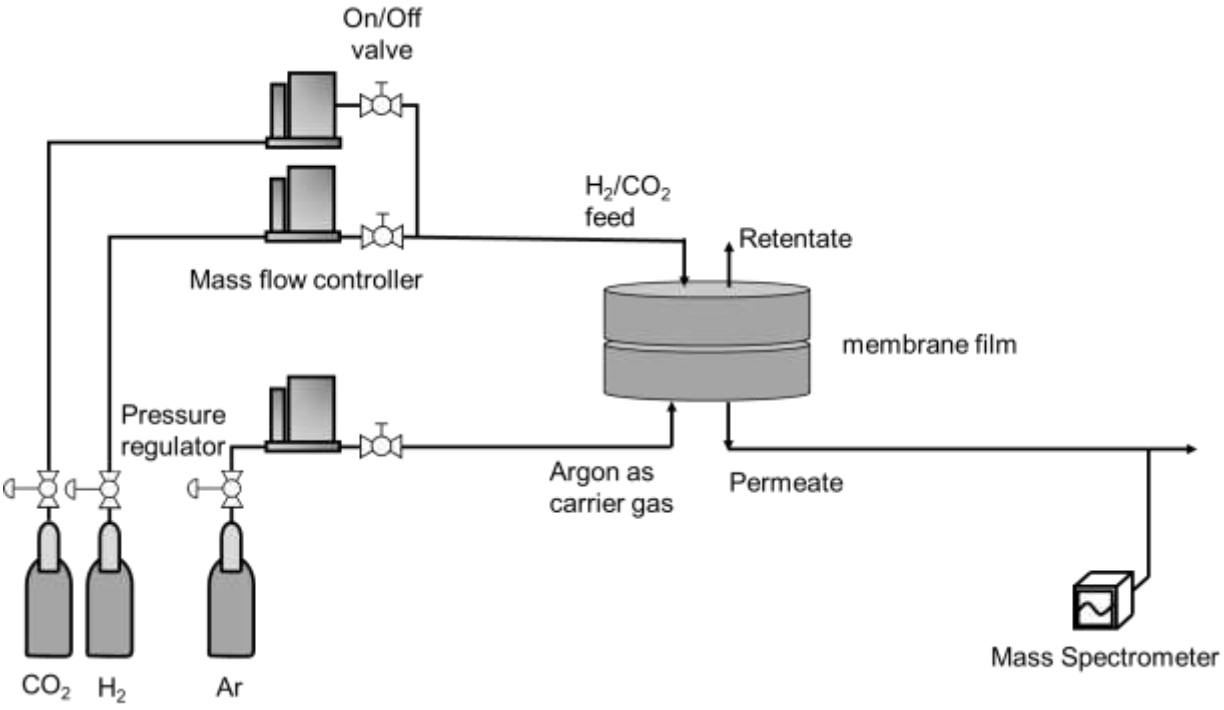


*Figure 2.2-23: Schematic of permeation study*

The permeance and selectivity was calculated by linear fit of $F_i$ vs. $\Delta p_i$ data where slope of lines is the permeance and ratio of permeance is selectivity. Initial gas permeation tests were performed with as received polysulfone film and permeance of ~0.25 GPU and ~0.125 GPU was observed for $H_2$ and $CO_2$ respectively and a selectivity of 2 for a 100 µm film. The measured values

were compared with permeance (0.19 GPU) and selectivity value (~ 1.87) for the same thickness polysulfone membrane studied in the literature.[157] The selectivity and permeance of the polysulfone film increased significantly on LIG formation on the surface. The selectivity vs. permeance of hydrogen values for LIG1 (power: 9.8 W; speed: 80 mm/s; resolution: 250 PPI) and polysulfone samples are shown in. LIG1 sample has a selectivity of 30.5 ± 1.4 and permeance of 176.4 ± 19.5 GPU, respectively, and the data points are highly reproducible. The performance of LIG/polysulfone membranes is comparable to GO on porous substrate (Hollow fiber, alumina, and metal organic frameworks) membranes and crosses the Robeson upper bound for 1 μm thick membranes.[27, 29, 163-165] **Table 1** summarizes the membrane performance data. For higher PPI values with optimized laser parameters, the membrane performance improved but the reproducibility was poor. The overlap between areas exposed to the laser increases with increasing PPI and adds more uncertainty to the data.[142]

**Table 3: Permeance and selectivity of LIG1 samples and polysulfone (control)**

| Sample | Permeance $H_2$ [GPU] [a] | Permeance $CO_2$ [GPU] [a] | $H_2/CO_2$ Selectivity |
|---|---|---|---|
| **Polysulfone** | 1.0 | 0.4 | 2.2 |
| **LIG1-1** | 167.8 | 5.2 | 32.1 |
| **LIG1-2** | 203.4 | 6.6 | 30.8 |
| **LIG1-3** | 158.0 | 5.5 | 28.75 |

[a]GPU, Gas Permeation Unit (1 GPU = $3.35 \times 10^{-10}$ mol $m^{-2}$ $s^{-1}$ $Pa^{-1}$)

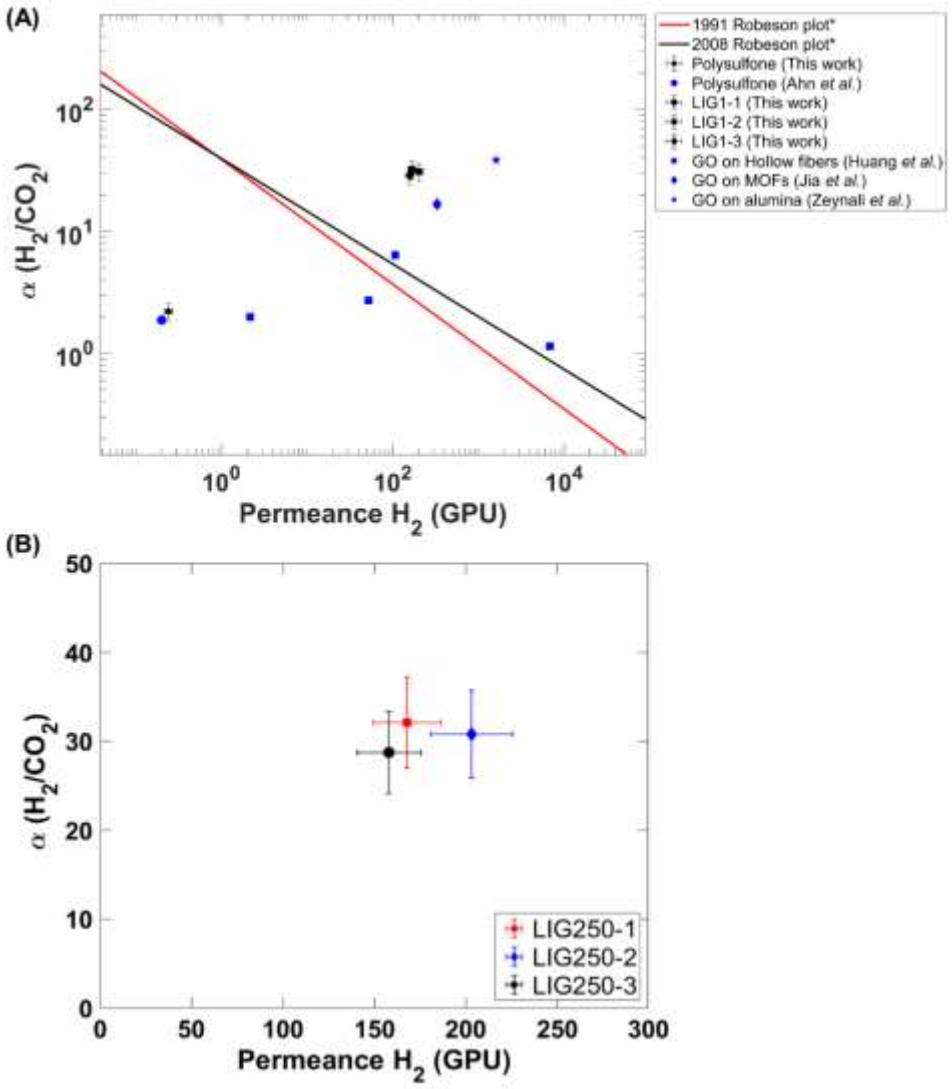


*Figure 2.2-24: (A) Comparison of selectivity and permeance of LIG membranes with control neat polysulfone (and published work on polysulfone),[157] Robeson plot (*Robeson plot for selectivity vs. permeance of 1μm thick membranes),[30] and similar previous literature (GO on polymeric hollow fibers, GO on MOFs, and GO on alumina),[163-165] (B) LIG membranes with error plot indicating repeatability of membrane performance using LIG1 processing parameters.*

Several factors may contribute to enhancements in selectivity of LIG/polysulfone relative to neat polysulfone. The LIG/polysulfone interface acts as a molecular sieve, allowing hydrogen to pass through the membrane and preventing the flow of $CO_2$. Several prior reports have

confirmed that the interlayer spacing for LIG (3.4 Å) is equivalent to graphene membranes, which contributes to this observed improvement in the selectivity.[153, 166-167] However, the selectivity values of LIG/polysulfone are still lower than GO and r-GO membranes or carbon molecular sieves; this can be attributed to the lack of uniform, conformal graphene sheets in LIG/polysulfone.[168-169] However, LIG has several advantages over traditional GO processing techniques: this process is rapid, can be fabricated in ambient conditions, is compatible with roll-to-roll processing, and can be created from a wide variety of polymers. In addition, enhancement in selectivity may also be attributed to a reduction in surface polar groups (sulfonic acids, sulfoxides and sulfones) resulting from LIG formation, which would reduce $CO_2$ solubility in polysulfone. In the neat polymer, sulfonic acid and sulfoxide groups enhance $CO_2$ solubility via polar interactions and hydrogen bonding with C=O bond. In the LIG phase, from the XPS data and peak deconvolution for S2p electronic state, it is seen that some of these polar groups are reduced photothermally to sulfide and disulfide groups. The polar groups interact with $CO_2$ via dipole-quadrupole interaction which is stronger than the hydrogen bonding.[170-171] Thus, decreased in polar interactions would decrease the solubility of $CO_2$ in the membrane, leading to an increase in selectivity for $H_2/CO_2$.[136, 172-173]

The increased hydrogen permeance of the LIG/polysulfone membranes indicates that the substrate polymer undergoes a change during the laser process. GPC data in **Table S4** shows that there is a slight decrease in molecular weight after the laser process, and DSC data confirms that there is a shift in glass transition temperature. During the laser exposure, the polymer is rapidly heated and then cooled, allowing changes in the existing micro and nano structures that contribute to the significant improvement in the overall permeance.[174-175] Prior literature have confirmed the improvement in diffusion of gases when polymer goes through the glass transition temperature

and extra free-volume is immobilized in the mixture, and also, the interchain distance (d-spacing) of the polymer decreases as confirmed by Wide angle X-ray Diffraction analysis (Figure 2.2-22).[176-179] The selectivity of LIG/polysulfone membranes in this work are equivalent to literature values reported for GO on porous hollow fiber and porous alumina substrates. Thus, the formation of this functional molecular sieving LIG layer, combined with the changes in the underlying polysulfone layer, explains the observed selectivity (~15x) and permeance (~700x) increases. Future research efforts will focus on understanding the relative contributions of each of these factors.

## 4.4 Conclusion

In conclusion, this study demonstrates an improvement in hydrogen selectivity as well as permeance over neat polysulfone using a scalable and rapid formation of laser induced graphene on the surface of polysulfone membranes. Also, the laser parameters play an important role in making conformal membranes. The observed enhancement in perm-selectivity of these membranes is possibly due to the molecular sieving carbon interface between graphene foam-like structure and polymer, decrease in polar sulfonic acid and sulfoxide groups on the surface of the membrane due to LIG formation, and large pore formation in polymeric phase.

# 5. Summary

## 5.1 Layer-by-layer membranes

Layer-by-layer approach provide an alternate approach to produce highly selective membranes deposited on high flux, low cost, easily manufacturable, and low selective hollow fibers. The hollow fiber support used in the study is produced using commercially used polymers with standard spinning process. The cost of manufacturing these membranes is expected to be comparable to the commercially available membrane. In Summary, layer-by-layer technique provide a new approach to deposit defect free coating of novel material that are industrially applicable. Given the performance of previously published work on LbL membranes, this work combined the properties of hollow fiber with surface functionalization to enhance the permselectivity of the membranes.

In future work, further analysis on LbL membrane is proposed to further analyze the structure-property relationship of the membrane. Polymeric membranes follow solution diffusion mechanism and further analysis of solubility and diffusivity of gases in the LbL films will provide fundamental understanding of the materials. Quartz crystal microbalance with dissipation (QCM-D) can be used to analyze the solubility of gases in the layers and study the effect of solubility with change in the numbers of bilayers. QCM-D can be used to detect change in the mass at picogram level and it can be used analyze the adsorption of these gases on a free-standing substrate with multiple bilayers.

This study has mainly focused on initial study of the LbL on hollow fibers for their application in hydrogen purification and carbon capture that can be further analyzed for industrial usage. In further studies, this membrane will be employed on a pilot-plant scale to study the response on a simulated flue gas mixture. Future studies will also focus on long-term stability, and

other influencing factors (including heat, moisture, acid, and other contaminants like SO2). For the permeability analysis, authors have used a mix gas as feed instead of pure gases as CO2 acts as a plasticizer for polymeric membranes which have an effect on the permeability of other gas (in this case nitrogen) therefore, it is important to analyze permeation performance of mixed gases.

## 5.2 Laser-induced-graphene membrane

The formation of LIG layer on surface of polymeric membranes modify surface properties in multiple ways: (a) Molecular sieve formation, (b) Change in hydrophilicity/hydrophobicity of material, (c) Change in functional groups on surface of polymer and hence, change in adsorption of gases on surface of polymer, and (d) Increased surface area due to porous LIG formation . These surface properties depend on the laser parameters like speed, power, PPI, and the atmosphere (oxidizing condition or reducing conditions ). The molecular dynamic simulations will provide better understanding the surface properties of LIG as a function of polymer choice and laser processing parameters. The modified surface properties can enhance the separation performance of membranes by combining multiple mechanisms. Future studies can focus n further characterization and analysis of structure property relationship.

The pore structure and surface area will be studied using BET analysis and mercury porosimeter. Dry polymeric substrate before and after LIG formation (and subsequent removal via doctor blade) will be characterized to measure extent of pore formation in polymer substrate during LIG formation. Further experiments on LIG powder can be performed to assess chemisorption activity of LIG formed over range of light gases (He, H2, CO, CO2, N2, CH4). For light gas separation, defect-free LIG/polymer membranes will be tested using a cross-flow permeation cell to quantify individual gas permeabilities over a range of binary gas pairs. Also, the effect of temperature on the permeation performance will studied using experiments over a suitable range

of membrane temperatures (nominally 298 – 398K) via multi-zone external heating of the entire permeation assembly.

In the final step, an in-depth study on the molecular dynamic simulation can be done using theoretical models to calculate individual selectivity and permeability of skin layer and substrate. The experimental data for selectivity, and permeability along with the characterization of the material will be used to compare with the proposed molecular simulations. ReaxFF simulations will be carried out to study chemisorption for S-doped LIG by examining the reduction of surface polar groups on polysulfone films and the H2 adsorption.

## REFERENCE


1. Sholl, D. S.; Lively, R. P., Seven chemical separations to change the world. *Nature News* **2016,** *532* (7600), 435.

2. Bernardo, P.; Drioli, E.; Golemme, G., Membrane gas separation: A review/state of the art. *Industrial and Engineering Chemistry Research* **2009,** *48* (10), 4638-4663.

3. Koros, W. J.; Fleming, G., Membrane-based gas separation. *Journal of membrane science* **1993,** *83* (1), 1-80.

4. Smith, A.; Klosek, J., A review of air separation technologies and their integration with energy conversion processes. *Fuel processing technology* **2001,** *70* (2), 115-134.

5. Sircar, S.; Golden, T., Purification of hydrogen by pressure swing adsorption. *Separation Science and Technology* **2000,** *35* (5), 667-687.

6. Ismail, A. F.; Khulbe, K. C.; Matsuura, T., Gas separation membranes. *Switz. Springer* **2015,** *10*, 978-3.

7. Chong, K.; Lai, S.; Thiam, H.; Teoh, H.; Heng, S., Recent progress of oxygen/nitrogen separation using membrane technology. *J. Eng. Sci. Technol* **2016,** *11*, 1016-1030.

8. Singh-Ghosal, A.; Koros, W., Air separation properties of flat sheet homogeneous pyrolytic carbon membranes. *Journal of Membrane Science* **2000,** *174* (2), 177-188.

9. Ockwig, N. W.; Nenoff, T. M., Membranes for hydrogen separation. *Chemical Reviews* **2007,** *107* (10), 4078-4110.

10. Alves, J. J.; Towler, G. P., Analysis of refinery hydrogen distribution systems. *Industrial & Engineering Chemistry Research* **2002,** *41* (23), 5759-5769.

11. Pinnau, I.; He, Z., Pure-and mixed-gas permeation properties of polydimethylsiloxane for hydrocarbon/methane and hydrocarbon/hydrogen separation. *Journal of membrane science* **2004,** *244* (1-2), 227-233.

12. Tong, J.; Matsumura, Y., Pure hydrogen production by methane steam reforming with hydrogen-permeable membrane reactor. *Catalysis today* **2006,** *111* (3-4), 147-152.

13. Dry, M. E., The fischer–tropsch process: 1950–2000. *Catalysis today* **2002,** *71* (3-4), 227-241.

14. Adhikari, S.; Fernando, S., Hydrogen membrane separation techniques. *Industrial & Engineering Chemistry Research* **2006,** *45* (3), 875-881.

15. Aika, K.-i.; Christiansen, L.; Dybkjaer, I.; Hansen, J.; Nielsen, P. H.; Nielsen, A.; Stoltze, P.; Tamaru, K., *Ammonia: catalysis and manufacture*. Springer Science & Business Media: 2012.

16. Du, H.; Li, J.; Zhang, J.; Su, G.; Li, X.; Zhao, Y., Separation of hydrogen and nitrogen gases with porous graphene membrane. *The Journal of Physical Chemistry C* **2011,** *115* (47), 23261-23266.

17. Rahimpour, M.; Samimi, F.; Babapoor, A.; Tohidian, T.; Mohebi, S., Palladium membranes applications in reaction systems for hydrogen separation and purification: A review. *Chemical Engineering and Processing: Process Intensification* **2017,** *121*, 24-49.

18. Abdalla, A. M.; Hossain, S.; Nisfindy, O. B.; Azad, A. T.; Dawood, M.; Azad, A. K., Hydrogen production, storage, transportation and key challenges with applications: A review. *Energy conversion and management* **2018,** *165*, 602-627.

19. Dincer, I.; Acar, C., Review and evaluation of hydrogen production methods for better sustainability. *International journal of hydrogen energy* **2015,** *40* (34), 11094-11111.

20. Li, H.; Song, Z.; Zhang, X.; Huang, Y.; Li, S.; Mao, Y.; Ploehn, H. J.; Bao, Y.; Yu, M., Ultrathin, Molecular-Sieving Graphene Oxide Membranes for Selective Hydrogen Separation. *Science* **2013,** *342* (6154), 95-98.

21. Scholes, C. A.; Smith, K. H.; Kentish, S. E.; Stevens, G. W., CO2 capture from pre-combustion processes—Strategies for membrane gas separation. *International Journal of Greenhouse Gas Control* **2010,** *4* (5), 739-755.

22. Chu, S., Carbon capture and sequestration. American Association for the Advancement of Science: 2009.

23. Chu, S.; Majumdar, A., Opportunities and challenges for a sustainable energy future. *nature* **2012,** *488* (7411), 294-303.

24. Levitz, P., From Knudsen diffusion to Levy walks. *EPL (Europhysics Letters)* **1997,** *39* (6), 593.

25. Joshi, R.; Carbone, P.; Wang, F.-C.; Kravets, V. G.; Su, Y.; Grigorieva, I. V.; Wu, H.; Geim, A. K.; Nair, R. R., Precise and ultrafast molecular sieving through graphene oxide membranes. *science* **2014,** *343* (6172), 752-754.

26. Koenig, S. P.; Wang, L.; Pellegrino, J.; Bunch, J. S., Selective molecular sieving through porous graphene. *Nature Nanotechnology* **2012,** *7* (11), 728-732.

27. Robeson, L. M., Correlation of separation factor versus permeability for polymeric membranes. *Journal of Membrane Science* **1991,** *62* (2), 165-185.

28. Robeson, L. M., Polymer membranes for gas separation. *Current Opinion in Solid State and Materials Science* **1999,** *4* (6), 549-552.

29. Robeson, L. M., The upper bound revisited. *Journal of Membrane Science* **2008,** *320* (1-2), 390-400.

30. Park, H. B.; Kamcev, J.; Robeson, L. M.; Elimelech, M.; Freeman, B. D., Maximizing the right stuff: The trade-off between membrane permeability and selectivity. *Science* **2017,** *356* (6343), eaab0530.

31. Freeman, B. D., Basis of permeability/selectivity tradeoff relations in polymeric gas separation membranes. *Macromolecules* **1999,** *32* (2), 375-380.

32. Sridhar, S.; Bee, S.; Bhargava, S. K., Membrane-based gas separation: principle, applications and future potential. *Materials Science* **2014**.

33. Figoli, A.; Santoro, S.; Galiano, F.; Basile, A., 2 - Pervaporation membranes: preparation, characterization, and application. In *Pervaporation, Vapour Permeation and Membrane Distillation*, Basile, A.; Figoli, A.; Khayet, M., Eds. Woodhead Publishing: Oxford, 2015; pp 19-63.

34. Bray, D. T.; Hopkins, D. H., Spiral wound membrane. Google Patents: 1989.

35. Qi, Z.; Cussler, E., Microporous hollow fibers for gas absorption: II. Mass transfer across the membrane. *Journal of Membrane Science* **1985,** *23* (3), 333-345.

36. Yang, M. C.; Cussler, E., Designing hollow-fiber contactors. *AIChE Journal* **1986,** *32* (11), 1910-1916.

37. Zhang, L.-Z., Chapter 8 - Heat and Mass Transfer in Hollow Fiber Membrane Bundles with Randomly Distributed Fibers. In *Conjugate Heat and Mass Transfer in Heat Mass Exchanger Ducts*, Zhang, L.-Z., Ed. Academic Press: Boston, 2013; pp 233-254.

38. Caskey, T. L., Method of forming tubesheet for hollow fibers. Google Patents: 1993.

39. Stroeve, P.; Vasquez, V.; Coelho, M. A. N.; Rabolt, J. F., Gas transfer in supported films made by molecular self-assembly of ionic polymers. *Thin Solid Films* **1996,** *284-285*, 708-712.

40. Dunn, S., Hydrogen futures: toward a sustainable energy system. *International Journal of Hydrogen Energy* **2002,** *27* (3), 235-264.

41. Turner, J. A., Sustainable hydrogen production. *Science* **2004,** *305* (5686), 972-974.

42. Gamble, A., Ullmann's encyclopedia of industrial chemistry. *The Charleston Advisor* **2019,** *20* (4), 46-50.

43. Kleinert, M.; Barth, T., Towards a lignincellulosic biorefinery: direct one-step conversion of lignin to hydrogen-enriched biofuel. *Energy & Fuels* **2008,** *22* (2), 1371-1379.

44. Ramachandran, R.; Menon, R. K., An overview of industrial uses of hydrogen. *International Journal of Hydrogen Energy* **1998,** *23* (7), 593-598.

45. Marbán, G.; Valdés-Solís, T., Towards the hydrogen economy? *International Journal of Hydrogen Energy* **2007,** *32* (12), 1625-1637.

46. Stern, S. A., Polymers for gas separations: the next decade. *Journal of Membrane Science* **1994,** *94* (1), 1-65.

47. Park, H. B.; Kamcev, J.; Robeson, L. M.; Elimelech, M.; Freeman, B. D., Maximizing the right stuff: The trade-off between membrane permeability and selectivity. *Science* **2017,** *356* (6343).

48. Robeson, L. M., The upper bound revisited. *Journal of Membrane Science* **2008,** *320* (1), 390-400.

49. Kirkland, J. J., Porous Thin-Layer Modified Glass Bead Supports for Gas Liquid Chromatography. *Analytical Chemistry* **1965,** *37* (12), 1458-1461.

50. Hammond, P. T., Building biomedical materials layer-by-layer. *Materials Today* **2012,** *15* (5), 196-206.

51. Ariga, K.; Lvov, Y. M.; Kawakami, K.; Ji, Q.; Hill, J. P., Layer-by-layer self-assembled shells for drug delivery. *Advanced Drug Delivery Reviews* **2011,** *63* (9), 762-771.

52. Liu, N.; Guo, H.; Fu, L.; Kaiser, S.; Schweizer, H.; Giessen, H., Three-dimensional photonic metamaterials at optical frequencies. *Nature Materials* **2007,** *7*, 31.

53. Qie, L.; Manthiram, A., A facile layer-by-layer approach for high-areal-capacity sulfur cathodes. *Advanced Materials* **2015,** *27* (10), 1694-1700.

54. Jin, W.; Toutianoush, A.; Tieke, B., Use of polyelectrolyte layer-by-layer assemblies as nanofiltration and reverse osmosis membranes. *Langmuir* **2003,** *19* (7), 2550-2553.

55. Lutkenhaus, J. L.; Hammond, P. T., Electrochemically enabled polyelectrolyte multilayer devices: from fuel cells to sensors. *Soft Matter* **2007,** *3* (7), 804-816.

56. Yang, Y. H.; Bolling, L.; Priolo, M. A.; Grunlan, J. C., Super gas barrier and selectivity of graphene oxide-polymer multilayer thin films. *Adv Mater* **2013,** *25* (4), 503-8.

57. Richardson, J. J.; Björnmalm, M.; Caruso, F., Technology-driven layer-by-layer assembly of nanofilms. *Science* **2015,** *348* (6233), aaa2491.

58. McAloney, R. A.; Sinyor, M.; Dudnik, V.; Goh, M. C., Atomic Force Microscopy Studies of Salt Effects on Polyelectrolyte Multilayer Film Morphology. *Langmuir* **2001,** *17* (21), 6655-6663.

59. Yang, Y.-H.; Haile, M.; Park, Y. T.; Malek, F. A.; Grunlan, J. C., Super Gas Barrier of All-Polymer Multilayer Thin Films. *Macromolecules* **2011,** *44* (6), 1450-1459.

60. Lundin, M.; Solaqa, F.; Thormann, E.; Macakova, L.; Blomberg, E., Layer-by-layer assemblies of chitosan and heparin: effect of solution ionic strength and pH. *Langmuir* **2011,** *27* (12), 7537-7548.

61. Shimazaki, Y.; Nakamura, R.; Ito, S.; Yamamoto, M., Molecular weight dependence of alternate adsorption through charge-transfer interaction. *Langmuir* **2001,** *17* (3), 953-956.

62. Xiang, F.; Tzeng, P.; Sawyer, J. S.; Regev, O.; Grunlan, J. C., Improving the gas barrier property of clay-polymer multilayer thin films using shorter deposition times. *ACS Appl Mater Interfaces* **2014,** *6* (9), 6040-8.

63. Chang, L.; Kong, X.; Wang, F.; Wang, L.; Shen, J., Layer-by-layer assembly of poly (N-acryloyl-N'-propylpiperazine) and poly (acrylic acid): Effect of pH and temperature. *Thin Solid Films* **2008,** *516* (8), 2125-2129.

64. Sullivan, D.; Bruening, M., Ultrathin, gas-selective polyimide membranes prepared from multilayer polyelectrolyte films. *Chemistry of materials* **2003,** *15* (1), 281-287.

65. Leväsalmi, J.-M.; McCarthy, T. J., Poly(4-methyl-1-pentene)-Supported Polyelectrolyte Multilayer Films: Preparation and Gas Permeability. *Macromolecules* **1997,** *30* (6), 1752-1757.

66. Kim, D.; Tzeng, P.; Barnett, K. J.; Yang, Y. H.; Wilhite, B. A.; Grunlan, J. C., Highly size-selective ionically crosslinked multilayer polymer films for light gas separation. *Adv Mater* **2014,** *26* (5), 746-51.

67. Wallace, D. W. Crosslinked hollow fiber membranes for natural gas purification and their manufacture from novel polymers. 2004.

68. Kosuri, M. R.; Koros, W. J., Defect-free asymmetric hollow fiber membranes from Torlon®, a polyamide–imide polymer, for high-pressure CO2 separations. *Journal of Membrane Science* **2008,** *320* (1), 65-72.

69. Vaughn, J. T.; Koros, W. J.; Johnson, J. R.; Karvan, O., Effect of thermal annealing on a novel polyamide–imide polymer membrane for aggressive acid gas separations. *Journal of Membrane Science* **2012,** *401-402*, 163-174.

70. Lim, S. K.; Setiawan, L.; Bae, T.-H.; Wang, R., Polyamide-imide hollow fiber membranes crosslinked with amine-appended inorganic networks for application in solvent-resistant nanofiltration under low operating pressure. *Journal of Membrane Science* **2016,** *501*, 152-160.

71. Wang, Y.; Goh, S. H.; Chung, T. S.; Na, P., Polyamide-imide/polyetherimide dual-layer hollow fiber membranes for pervaporation dehydration of C1–C4 alcohols. *Journal of Membrane Science* **2009,** *326* (1), 222-233.

72. Sun, S. P.; Wang, K. Y.; Rajarathnam, D.; Hatton, T. A.; Chung, T. S., Polyamide-imide nanofiltration hollow fiber membranes with elongation-induced nano-pore evolution. *AIChE journal* **2010,** *56* (6), 1481-1494.

73. Sun, S. P.; Hatton, T. A.; Chung, T. S., Hyperbranched polyethyleneimine induced cross-linking of polyamide-imide nanofiltration hollow fiber membranes for effective removal of ciprofloxacin. *Environ Sci Technol* **2011,** *45* (9), 4003-9.

74. Setiawan, L.; Wang, R.; Li, K.; Fane, A. G., Fabrication of novel poly(amide–imide) forward osmosis hollow fiber membranes with a positively charged nanofiltration-like selective layer. *Journal of Membrane Science* **2011,** *369* (1), 196-205.

75. Li, F. S.; Qiu, W.; Lively, R. P.; Lee, J. S.; Rownaghi, A. A.; Koros, W. J., Polyethyleneimine-Functionalized Polyamide Imide (Torlon) Hollow-Fiber Sorbents for Post-Combustion CO2 Capture. *ChemSusChem* **2013,** *6* (7), 1216-1223.

76. Li, F. S.; Qiu, W.; Lively, R. P.; Lee, J. S.; Rownaghi, A. A.; Koros, W. J., Polyethyleneimine-functionalized polyamide imide (Torlon) hollow-fiber sorbents for post-combustion CO2 capture. *ChemSusChem* **2013,** *6* (7), 1216-23.

77. Stalder, A. F.; Melchior, T.; Müller, M.; Sage, D.; Blu, T.; Unser, M., Low-bond axisymmetric drop shape analysis for surface tension and contact angle measurements of sessile drops. *Colloids and Surfaces A: Physicochemical and Engineering Aspects* **2010,** *364* (1), 72-81.

78. Podsiadlo, P.; Michel, M.; Lee, J.; Verploegen, E.; Wong Shi Kam, N.; Ball, V.; Lee, J.; Qi, Y.; Hart, A. J.; Hammond, P. T.; Kotov, N. A., Exponential Growth of LBL Films with Incorporated Inorganic Sheets. *Nano Letters* **2008,** *8* (6), 1762-1770.

79. Yoo, P. J.; Nam, K. T.; Qi, J.; Lee, S.-K.; Park, J.; Belcher, A. M.; Hammond, P. T., Spontaneous assembly of viruses on multilayered polymer surfaces. *Nature Materials* **2006,** *5* (3), 234-240.

80. Song, Y.; Meyers, K. P.; Gerringer, J.; Ramakrishnan, R. K.; Humood, M.; Qin, S.; Polycarpou, A. A.; Nazarenko, S.; Grunlan, J. C., Fast Self-Healing of Polyelectrolyte Multilayer Nanocoating and Restoration of Super Oxygen Barrier. *Macromol Rapid Commun* **2017,** *38* (10).

81. Holder, K. M.; Priolo, M. A.; Secrist, K. E.; Greenlee, S. M.; Nolte, A. J.; Grunlan, J. C., Humidity-Responsive Gas Barrier of Hydrogen-Bonded Polymer–Clay Multilayer Thin Films. *The Journal of Physical Chemistry C* **2012,** *116* (37), 19851-19856.

82. Hautier, Y.; Tilman, D.; Isbell, F.; Seabloom, E. W.; Borer, E. T.; Reich, P. B., Anthropogenic environmental changes affect ecosystem stability via biodiversity. *Science* **2015,** *348* (6232), 336-340.

83. Muradov, N. Z.; Veziroğlu, T. N., "Green" path from fossil-based to hydrogen economy: an overview of carbon-neutral technologies. *International journal of hydrogen energy* **2008,** *33* (23), 6804-6839.

84. Masson-Delmotte, V.; Zhai, P.; Pörtner, H.-O.; Roberts, D.; Skea, J.; Shukla, P. R.; Pirani, A.; Moufouma-Okia, W.; Péan, C.; Pidcock, R., Global warming of 1.5 C. *An IPCC Special Report on the impacts of global warming of* **2018,** *1*.

85. Haszeldine, R. S., Carbon capture and storage: how green can black be? *Science* **2009,** *325* (5948), 1647-1652.

86. Agency, I. E. In *Key World energy Statistics 2019*, IEA Paris: 2019.

87. D'Alessandro, D. M.; Smit, B.; Long, J. R., Carbon dioxide capture: prospects for new materials. *Angewandte Chemie International Edition* **2010,** *49* (35), 6058-6082.

88. Samanta, A.; Zhao, A.; Shimizu, G. K.; Sarkar, P.; Gupta, R., Post-combustion CO2 capture using solid sorbents: a review. *Industrial & Engineering Chemistry Research* **2012,** *51* (4), 1438-1463.

89. Zhao, M.; Minett, A. I.; Harris, A. T., A review of techno-economic models for the retrofitting of conventional pulverised-coal power plants for post-combustion capture (PCC) of CO 2. *Energy & Environmental Science* **2013,** *6* (1), 25-40.

90. Scott, V.; Gilfillan, S.; Markusson, N.; Chalmers, H.; Haszeldine, R. S., Last chance for carbon capture and storage. *Nature Climate Change* **2013,** *3* (2), 105-111.

91. Zhao, L.; Riensche, E.; Menzer, R.; Blum, L.; Stolten, D., A parametric study of CO2/N2 gas separation membrane processes for post-combustion capture. *Journal of Membrane Science* **2008,** *325* (1), 284-294.

92. Zhang, X.; He, X.; Gundersen, T., Post-combustion carbon capture with a gas separation membrane: parametric study, capture cost, and exergy analysis. *Energy & Fuels* **2013,** *27* (8), 4137-4149.

93. Merkel, T. C.; Lin, H.; Wei, X.; Baker, R., Power plant post-combustion carbon dioxide capture: An opportunity for membranes. *Journal of Membrane Science* **2010,** *359* (1-2), 126-139.

94. Saufi, S.; Ismail, A., Fabrication of carbon membranes for gas separation—a review. *Carbon* **2004,** *42* (2), 241-259.

95. Lin, H.; Van Wagner, E.; Raharjo, R.; Freeman, B. D.; Roman, I., High-performance polymer membranes for natural-gas sweetening. *Advanced Materials* **2006,** *18* (1), 39-44.

96. Lin, H.; Freeman, B. D., Gas solubility, diffusivity and permeability in poly(ethylene oxide). *Journal of Membrane Science* **2004,** *239* (1), 105-117.

97. Shao, L.; Chung, T.-S.; Wensley, G.; Goh, S. H.; Pramoda, K. P., Casting solvent effects on morphologies, gas transport properties of a novel 6FDA/PMDA–TMMDA copolyimide membrane and its derived carbon membranes. *Journal of Membrane Science* **2004,** *244* (1), 77-87.

98. Vanherck, K.; Koeckelberghs, G.; Vankelecom, I. F. J., Crosslinking polyimides for membrane applications: A review. *Progress in Polymer Science* **2013,** *38* (6), 874-896.

99. Car, A.; Stropnik, C.; Yave, W.; Peinemann, K.-V., Pebax®/polyethylene glycol blend thin film composite membranes for CO2 separation: Performance with mixed gases. *Separation and Purification Technology* **2008,** *62* (1), 110-117.

100. Hammond, P. T., Engineering materials layer-by-layer: Challenges and opportunities in multilayer assembly. *AIChE Journal* **2011,** *57* (11), 2928-2940.

101. Chen, Y.; Chen, T.; Dai, L., Layer-by-layer growth of CH3NH3PbI3− xClx for highly efficient planar heterojunction perovskite solar cells. *Advanced Materials* **2015,** *27* (6), 1053-1059.

102. Yang, Y. H.; Haile, M.; Park, Y. T.; Malek, F. A.; Grunlan, J. C., Super gas barrier of all-polymer multilayer thin films. *Macromolecules* **2011,** *44* (6), 1450-1459.

103. Leväsalmi, J. M.; McCarthy, T. J., Poly(4-methyl-1-pentene)-supported polyelectrolyte multilayer films: Preparation and gas permeability. *Macromolecules* **1997,** *30* (6), 1752-1757.

104. Sullivan, D. M.; Bruening, M. L., Ultrathin, gas-selective polyimide membranes prepared from multilayer polyelectrolyte films. *Chemistry of Materials* **2003,** *15* (1), 281-287.

105. Bruening, M. L.; Sullivan, D. M., Enhancing the ion-transport selectivity of multilayer polyelectrolyte membranes. *Chemistry–A European Journal* **2002,** *8* (17), 3832-3837.

106. Yong, J. K. J.; Stevens, G. W.; Caruso, F.; Kentish, S. E., In situ layer-by-layer assembled carbonic anhydrase-coated hollow fiber membrane contactor for rapid CO2 absorption. *Journal of Membrane Science* **2016,** *514*, 556-565.

107. Chung, A. J.; Rubner, M. F., Methods of loading and releasing low molecular weight cationic molecules in weak polyelectrolyte multilayer films. *Langmuir* **2002,** *18* (4), 1176-1183.

108. Delongchamp, D. M.; Hammond, P. T., Highly ion conductive poly(ethylene oxide)-based solid polymer electrolytes from hydrogen bonding layer-by-layer assembly. *Langmuir* **2004,** *20* (13), 5403-5411.

109. Sukhishvili, S. A.; Granick, S., Layered, erasable polymer multilayers formed by hydrogen-bonded sequential self-assembly. *Macromolecules* **2002,** *35* (1), 301-310.

110. Kharlampieva, E.; Sukhishvili, S. A., Hydrogen-bonded layer-by-layer polymer films. *Polymer Reviews* **2006,** *46* (4), 377-395.

111. Kim, D.; Tzeng, P.; Barnett, K. J.; Yang, Y. H.; Wilhite, B. A.; Grunlan, J. C., Highly size-selective ionically crosslinked multilayer polymer films for light gas separation. *Advanced Materials* **2014,** *26* (5), 746-751.

112. Song, Y.; Lugo, E. L.; Powell, S.; Tzeng, P.; Wilhite, B. A.; Grunlan, J. C., Highly selective multilayer polymer thin films for CO2/N2 separation. *Journal of Polymer Science Part B: Polymer Physics* **2017,** *55* (23), 1730-1737.

113. Grunlan, J. C.; Wilhite, B. A., Polyelectrolyte Multilayer Films for Gas Separation and Purification. Google Patents: 2016.

114. Tzeng, P.; Lugo, E. L.; Mai, G. D.; Wilhite, B. A.; Grunlan, J. C., Super hydrogen and helium barrier with polyelectolyte nanobrick wall thin film. *Macromolecular Rapid Communications* **2015,** *36* (1), 96-101.

115. Mishra, N. K.; Patil, N.; Long, C.; Yi, S.; Hopkinson, D.; Grunlan, J. C.; Wilhite, B. A., Enhancing H2-Permselectivity of high-flux hollow fiber membrane via in-situ layer-by-layer surface treatment. *Journal of Membrane Science* **2020**, 118312.

116. Lin, H.; Van Wagner, E.; Freeman, B. D.; Toy, L. G.; Gupta, R. P., Plasticization-enhanced hydrogen purification using polymeric membranes. *Science* **2006,** *311* (5761), 639-642.

117. Kosuri, M. R.; Koros, W. J., Defect-free asymmetric hollow fiber membranes from Torlon®, a polyamide–imide polymer, for high-pressure CO2 separations. *Journal of Membrane Science* **2008,** *320* (1-2), 65-72.

118. Li, F. S.; Qiu, W.; Lively, R. P.; Lee, J. S.; Rownaghi, A. A.; Koros, W. J., Polyethyleneimine-Functionalized Polyamide Imide (Torlon) Hollow-Fiber Sorbents for Post-Combustion CO2 Capture. *ChemSusChem* **2013,** *6* (7), 1216-1223.

119. Khutoryanskiy, V. V.; Dubolazov, A. V.; Nurkeeva, Z. S.; Mun, G. A., pH Effects in the Complex Formation and Blending of Poly(acrylic acid) with Poly(ethylene oxide). *Langmuir* **2004,** *20* (9), 3785-3790.

120. Sharma, A.; Smith, J.; Walters, K. B.; Rick, S. W., Constant pH simulations of pH responsive polymers. *The Journal of Chemical Physics* **2016,** *145* (23), 234906.

121. Picart, C.; Mutterer, J.; Richert, L.; Luo, Y.; Prestwich, G.; Schaaf, P.; Voegel, J.-C.; Lavalle, P., Molecular basis for the explanation of the exponential growth of polyelectrolyte multilayers. *Proceedings of the National Academy of Sciences* **2002,** *99* (20), 12531-12535.

122. Richert, L.; Lavalle, P.; Payan, E.; Shu, X. Z.; Prestwich, G. D.; Stoltz, J.-F.; Schaaf, P.; Voegel, J.-C.; Picart, C., Layer by Layer Buildup of Polysaccharide Films: Physical Chemistry and Cellular Adhesion Aspects. *Langmuir* **2004,** *20* (2), 448-458.

123. Miyoshi, T.; Takegoshi, K.; Hikichi, K., High-resolution solid-state 13C nuclear magnetic resonance study of a polymer complex: poly(methacrylic acid)/poly(ethylene oxide). *Polymer* **1996,** *37* (1), 11-18.

124. Schantz, S., Structure and Mobility in Poly(ethylene oxide)/Poly(methyl methacrylate) Blends Investigated by 13C Solid-State NMR. *Macromolecules* **1997,** *30* (5), 1419-1425.

125. Lowman, A. M.; Cowans, B. A.; Peppas, N. A., Investigation of interpolymer complexation in swollen polyelectolyte networks using solid-state NMR spectroscopy. *Journal of Polymer Science Part B: Polymer Physics* **2000,** *38* (21), 2823-2831.

126. Cao, Y.; Guan, Y.; Du, J.; Luo, J.; Peng, Y.; Yip, C. W.; Chan, A. S. C., Hydrogen-bonded polymer network—poly(ethylene glycol) complexes with shape memory effect. *Journal of Materials Chemistry* **2002,** *12* (10), 2957-2960.

127. Chaubey, R.; Sahu, S.; James, O. O.; Maity, S., A review on development of industrial processes and emerging techniques for production of hydrogen from renewable and sustainable sources. *Renewable and Sustainable Energy Reviews* **2013,** *23*, 443-462.

128. Thornton, A., Polymer Gas Separation Membranes. **2012**.

129. Pearton, S. J.; Corbett, J. W.; Stavola, M., *Hydrogen in crystalline semiconductors*. Springer Science & Business Media: 2013; Vol. 16.

130. Jacobson, M. Z.; Colella, W.; Golden, D., Cleaning the air and improving health with hydrogen fuel-cell vehicles. *Science* **2005,** *308* (5730), 1901-1905.

131. Babich, I. V.; Moulijn, J. A., Science and technology of novel processes for deep desulfurization of oil refinery streams: a review☆. *Fuel* **2003,** *82* (6), 607-631.

132. Holladay, J. D.; Hu, J.; King, D. L.; Wang, Y., An overview of hydrogen production technologies. *Catalysis today* **2009,** *139* (4), 244-260.

133. Fu, J.; Das, S.; Xing, G.; Ben, T.; Valtchev, V.; Qiu, S., Fabrication of COF-MOF Composite Membranes and Their Highly Selective Separation of H2/CO2. *Journal of the American Chemical Society* **2016,** *138* (24), 7673-7680.

134. Zhao, Z.; Ma, X.; Kasik, A.; Li, Z.; Lin, Y. S., Gas Separation Properties of Metal Organic Framework (MOF-5) Membranes. *Industrial & Engineering Chemistry Research* **2013,** *52* (3), 1102-1108.

135. Azar, A. N. V.; Velioglu, S.; Keskin, S., Large-Scale Computational Screening of Metal Organic Framework (MOF) Membranes and MOF-Based Polymer Membranes for H2/N2 Separations. *ACS Sustainable Chemistry & Engineering* **2019,** *7* (10), 9525-9536.

136. Won, J.; Kim, M. H.; Kang, Y. S.; Park, H. C.; Kim, U. Y.; Choi, S. C.; Koh, S. K., Surface modification of polyimide and polysulfone membranes by ion beam for gas separation. *Journal of Applied Polymer Science* **2000,** *75* (12), 1554-1560.

137. Thamaraiselvan, C.; Wang, J.; James, D. K.; Narkhede, P.; Singh, S. P.; Jassby, D.; Tour, J. M.; Arnusch, C. J., Laser-induced graphene and carbon nanotubes as conductive carbon-based materials in environmental technology. *Materials Today* **2019**.

138. Ye, R.; James, D. K.; Tour, J. M., Laser-Induced Graphene: From Discovery to Translation. *Advanced Materials* **2019,** *31* (1), 1803621.

139. Ye, R.; James, D. K.; Tour, J. M., Laser-Induced Graphene: From Discovery to Translation. *Adv. Mater.* **2019,** *31*, 1803621.

140. Hossain, M. Z.; Johns, J. E.; Bevan, K. H.; Karmel, H. J.; Liang, Y. T.; Yoshimoto, S.; Mukai, K.; Koitaya, T.; Yoshinobu, J.; Kawai, M.; Lear, A. M.; Kesmodel, L. L.; Tait, S. L.; Hersam, M. C., Chemically homogeneous and thermally reversible oxidation of epitaxial graphene. *Nature Chemistry* **2012,** *4* (4), 305-309.

141. Parviz, D.; Irin, F.; Shah, S. A.; Das, S.; Sweeney, C. B.; Green, M. J., Challenges in Liquid-Phase Exfoliation, Processing, and Assembly of Pristine Graphene. *Advanced Materials* **2016,** *28* (40), 8796-8818.

142. Chyan, Y.; Ye, R.; Li, Y.; Singh, S. P.; Arnusch, C. J.; Tour, J. M., Laser-Induced Graphene by Multiple Lasing: Toward Electronics on Cloth, Paper, and Food. *ACS Nano* **2018,** *12*, 2176.

143. Luong, D. X.; Yang, K.; Yoon, J.; Singh, S. P.; Wang, T.; Arnusch, C. J.; Tour, J. M., Laser-Induced Graphene Composites as Multifunctional Surfaces. *ACS Nano* **2019,** *13*, 2579.

144. Stanford, M. G.; Li, J. T.; Chyan, Y.; Wang, Z.; Wang, W.; Tour, J. M., Laser-Induced Graphene Triboelectric Nanogenerators. *ACS Nano* **2019,** *13*, 7166.

145. Stanford, M. G.; Yang, K.; Chyan, Y.; Kittrell, C.; Tour, J. M., Laser-Induced Graphene for Flexible and Embeddable Gas Sensors. *ACS Nano* **2019,** *13*, 3474.

146. Ye, R.; Peng, Z.; Wang, T.; Xu, Y.; Zhang, J.; Li, Y.; Nilewski, L. G.; Lin, J.; Tour, J. M., In Situ Formation of Metal Oxide Nanocrystals Embedded in Laser-Induced Graphene. *ACS Nano* **2015,** *9*, 9244.

147. Carvalho, A. F.; Fernandes, A. J. S.; Leitão, C.; Deuermeier, J.; Marques, A. C.; Martins, R.; Fortunato, E.; Costa, F. M., Laser-Induced Graphene Strain Sensors Produced by Ultraviolet Irradiation of Polyimide. *Adv. Funct. Mater.* **2018,** *28*, 1805271.

148. Gerringer, J. C.; Moran, A. G.; Habib, T.; Pospisil, M. J.; Oh, J. H.; Teipel, B. R.; Green, M. J., Radio Frequency Heating of Laser-Induced Graphene on Polymer Surfaces for Rapid Welding. *ACS Applied Nano Materials* **2019,** *2* (11), 7032-7042.

149. Baringhaus, J.; Ruan, M.; Edler, F.; Tejeda, A.; Sicot, M.; Taleb-Ibrahimi, A.; Li, A. P.; Jiang, Z.; Conrad, E. H.; Berger, C.; Tegenkamp, C.; de Heer, W. A., Exceptional Ballistic Transport in Epitaxial Graphene Nanoribbons. *Nature* **2014,** *506*, 349.

150. Chaudhury, S.; Thakur, A. K.; Gojman, R. S.; Arnusch, C. J.; Nir, O., Ion Transport in Laser-Induced Graphene Cation-Exchange Membrane Hybrids. *The Journal of Physical Chemistry Letters* **2020,** *11* (4), 1397-1403.

151. Li, J. T.; Stanford, M. G.; Chen, W.; Presutti, S. E.; Tour, J. M., Laminated Laser-Induced Graphene Composites. *ACS Nano* **2020**.

152. Li, L.; Zhang, J.; Peng, Z.; Li, Y.; Gao, C.; Ji, Y.; Ye, R.; Kim, N. D.; Zhong, Q.; Yang, Y.; Fei, H.; Ruan, G.; Tour, J. M., High-Performance Pseudocapacitive Microsupercapacitors from Laser-Induced Graphene. *Adv. Mater.* **2016,** *28*, 838.

153. Lin, J.; Peng, Z.; Liu, Y.; Ruiz-Zepeda, F.; Ye, R.; Samuel, E. L. G.; Yacaman, M. J.; Yakobson, B. I.; Tour, J. M., Laser-Induced Porous Graphene Films from Commercial Polymers. *Nat. Commun.* **2014,** *5*, 5714.

154. Peng, Z.; Lin, J.; Ye, R.; Samuel, E. L. G.; Tour, J. M., Flexible and Stackable Laser-Induced Graphene Supercapacitors. *ACS Appl. Mater. Interfaces* **2015,** *7*, 3414.

155. Singh, S. P.; Li, Y.; Zhang, J.; Tour, J. M.; Arnusch, C. J., Sulfur-Doped Laser-Induced Porous Graphene Derived from Polysulfone-Class Polymers and Membranes. *ACS Nano* **2018,** *12* (1), 289-297.

156. Pinnau, I.; Koros, W. J., Structures and gas separation properties of asymmetric polysulfone membranes made by dry, wet, and dry/wet phase inversion. *Journal of applied polymer science* **1991,** *43* (8), 1491-1502.

157. Ahn, J.; Chung, W.-J.; Pinnau, I.; Guiver, M. D., Polysulfone/silica nanoparticle mixed-matrix membranes for gas separation. *Journal of Membrane science* **2008,** *314* (1-2), 123-133.

158. Noshay, A.; Robeson, L. M., Sulfonated polysulfone. *Journal of Applied Polymer Science* **1976,** *20* (7), 1885-1903.

159. Erb, A. J.; Paul, D. R., Gas sorption and transport in polysulfone. *Journal of Membrane Science* **1981,** *8* (1), 11-22.

160. Gupta, B.; Kumar, N.; Panda, K.; Kanan, V.; Joshi, S.; Visoly-Fisher, I., Role of oxygen functional groups in reduced graphene oxide for lubrication. *Scientific Reports* **2017,** *7* (1), 45030.

161. Fu, Q.; Halim, A.; Kim, J.; Scofield, J. M. P.; Gurr, P. A.; Kentish, S. E.; Qiao, G. G., Highly permeable membrane materials for CO<inf>2</inf> capture. *Journal of Materials Chemistry A* **2013,** *1* (44), 13769-13778.

162. Garg, K.; Shanmugam, R.; Ramamurthy, P. C., New covalent hybrids of graphene oxide with core modified and -expanded porphyrins: Synthesis, characterisation and their non linear optical properties. *Carbon* **2017,** *122*, 307-318.

163. Jia, M.; Feng, Y.; Liu, S.; Qiu, J.; Yao, J., Graphene oxide gas separation membranes intercalated by UiO-66-NH2 with enhanced hydrogen separation performance. *Journal of Membrane Science* **2017,** *539*, 172-177.

164. Huang, K.; Yuan, J.; Shen, G.; Liu, G.; Jin, W., Graphene oxide membranes supported on the ceramic hollow fibre for efficient H2 recovery. *Chinese Journal of Chemical Engineering* **2017,** *25* (6), 752-759.

165. Zeynali, R.; Ghasemzadeh, K.; Sarand, A. B.; Kheiri, F.; Basile, A., Performance evaluation of graphene oxide (GO) nanocomposite membrane for hydrogen separation: Effect of dip coating sol concentration. *Separation and Purification Technology* **2018,** *200*, 169-176.

166. Zhu, C.; Zhao, D.; Wang, K.; Dong, X.; Duan, W.; Wang, F.; Gao, M.; Zhang, G., Direct laser writing of graphene films from a polyether ether ketone precursor. *Journal of Materials Science* **2019,** *54* (5), 4192-4201.

167. Zhu, J.; Guo, X.; Wang, H.; Song, W., Cost-effective fabrication and high-frequency response of non-ideal RC application based on 3D porous laser-induced graphene. *Journal of Materials Science* **2018,** *53* (17), 12413-12420.

168. Abdollahi, M.; Yu, J.; Liu, P. K. T.; Ciora, R.; Sahimi, M.; Tsotsis, T. T., Hydrogen production from coal-derived syngas using a catalytic membrane reactor based process. *Journal of Membrane Science* **2010,** *363* (1), 160-169.

169. Membrane reactors for hydrogen production from coal. In *Membrane Reactors for Energy Applications and Basic Chemical Production*, Basile, A.; Di Paola, L.; Hai, F. l.; Piemonte, V., Eds. Woodhead Publishing: 2015; pp xv-xviii.

170. Gu, Y.; Kar, T.; Scheiner, S., Fundamental Properties of the CH···O Interaction: Is It a True Hydrogen Bond? *Journal of the American Chemical Society* **1999,** *121* (40), 9411-9422.

171. Raveendran, P.; Wallen, S. L., Cooperative C−H···O Hydrogen Bonding in CO2−Lewis Base Complexes: Implications for Solvation in Supercritical CO2. *Journal of the American Chemical Society* **2002,** *124* (42), 12590-12599.

172. Bandosz, T. J.; Seredych, M.; Rodríguez-Castellón, E.; Cheng, Y.; Daemen, L. L.; Ramírez-Cuesta, A. J., Evidence for CO2 reactive adsorption on nanoporous S- and N-doped carbon at ambient conditions. *Carbon* **2016,** *96*, 856-863.

173. Seredych, M.; Jagiello, J.; Bandosz, T. J., Complexity of CO2 adsorption on nanoporous sulfur-doped carbons – Is surface chemistry an important factor? *Carbon* **2014,** *74*, 207-217.

174. Vashisth, A.; Kowalik, M.; Gerringer, J. C.; Ashraf, C.; van Duin, A. C. T.; Green, M. J., ReaxFF Simulations of Laser-Induced Graphene (LIG) Formation for Multifunctional Polymer Nanocomposites. *ACS Applied Nano Materials* **2020,** *3* (2), 1881-1890.

175. Bergsman, D. S.; Getachew, B. A.; Cooper, C. B.; Grossman, J. C., Preserving nanoscale features in polymers during laser induced graphene formation using sequential infiltration synthesis. *Nature Communications* **2020,** *11* (1), 3636.

176. Burns, R. L.; Koros, W. J., Structure− property relationships for poly (pyrrolone-imide) gas separation membranes. *Macromolecules* **2003,** *36* (7), 2374-2381.

177. Park, H. B.; Han, S. H.; Jung, C. H.; Lee, Y. M.; Hill, A. J., Thermally rearranged (TR) polymer membranes for CO2 separation. *Journal of Membrane Science* **2010,** *359* (1-2), 11-24.

178. Shapiro, A. A.; Davis, P. K.; Duda, J. L., Chapter 9 - Diffusion in Multicomponent Mixtures. In *Computer Aided Chemical Engineering*, Kontogeorgis, G. M.; Gani, R., Eds. Elsevier: 2004; Vol. 19, pp 205-227.

179. Vrentas, J.; Duda, J., A free-volume interpretation of the influence of the glass transition on diffusion in amorphous polymers. *Journal of applied polymer science* **1978,** *22* (8), 2325-2339.

180. Wells, P. B., Catalysis. In *Encyclopedia of Materials: Science and Technology*, Buschow, K. H. J.; Cahn, R. W.; Flemings, M. C.; Ilschner, B.; Kramer, E. J.; Mahajan, S.; Veyssière, P., Eds. Elsevier: Oxford, 2001; pp 1020-1025.

181. Fechete, I.; Wang, Y.; Védrine, J. C., The past, present and future of heterogeneous catalysis. *Catalysis Today* **2012,** *189* (1), 2-27.

182. Raseev, S., *Thermal and catalytic processes in petroleum refining*. CRC Press: 2003.

183. Sheldon, R. A.; Van Bekkum, H., *Fine chemicals through heterogeneous catalysis*. John Wiley & Sons: 2008.

184. Bender, T. A.; Dabrowski, J. A.; Gagné, M. R., Homogeneous catalysis for the production of low-volume, high-value chemicals from biomass. *Nature Reviews Chemistry* **2018,** *2* (5), 35.

185. Campos, K. R.; Coleman, P. J.; Alvarez, J. C.; Dreher, S. D.; Garbaccio, R. M.; Terrett, N. K.; Tillyer, R. D.; Truppo, M. D.; Parmee, E. R., The importance of synthetic chemistry in the pharmaceutical industry. *Science* **2019,** *363* (6424), eaat0805.

186. Busacca, C. A.; Fandrick, D. R.; Song, J. J.; Senanayake, C. H., The growing impact of catalysis in the pharmaceutical industry. *Advanced Synthesis & Catalysis* **2011,** *353* (11-12), 1825-1864.

187. Carberry, J. J.; Varma, A., Chemical reaction and reactor engineering. **1987**.

188. Ross, J. R., *Heterogeneous catalysis: fundamentals and applications*. Elsevier: 2011.

189. Peters, M. S.; Timmerhaus, K. D.; West, R. E.; Timmerhaus, K.; West, R., *Plant design and economics for chemical engineers*. McGraw-Hill New York: 1968; Vol. 4.

190. Zhang, T. Y., Process Chemistry: The Science, Business, Logic, and Logistics. *Chemical Reviews* **2006,** *106* (7), 2583-2595.

191. Luyben, W. L., *Chemical reactor design and control*. John Wiley & Sons: 2007.

192. Ross, J. R. H., Chapter 7 - Large-Scale Catalytic Reactors. In *Heterogeneous Catalysis*, Ross, J. R. H., Ed. Elsevier: Amsterdam, 2012; pp 143-169.

193. Karim, A.; Bravo, J.; Datye, A., Nonisothermality in packed bed reactors for steam reforming of methanol. *Applied Catalysis A: General* **2005,** *282* (1), 101-109.

194. Van Geem, K. M.; Galvita, V. V.; Marin, G. B., Making chemicals with electricity. *Science* **2019,** *364* (6442), 734-735.

195. Schiffer, Z. J.; Manthiram, K., Electrification and Decarbonization of the Chemical Industry. *Joule* **2017,** *1* (1), 10-14.

196. Lewis, N. S.; Nocera, D. G., Powering the planet: Chemical challenges in solar energy utilization. *Proceedings of the National Academy of Sciences* **2006,** *103* (43), 15729-15735.

197. Wismann, S. T.; Engbæk, J. S.; Vendelbo, S. B.; Bendixen, F. B.; Eriksen, W. L.; Aasberg-Petersen, K.; Frandsen, C.; Chorkendorff, I.; Mortensen, P. M., Electrified methane reforming: A compact approach to greener industrial hydrogen production. *Science* **2019,** *364* (6442), 756-759.

198. Grant, E.; Halstead, B. J., Dielectric parameters relevant to microwave dielectric heating. *Chemical society reviews* **1998,** *27* (3), 213-224.

199. Ramirez, A.; Hueso, J.; Abian, M.; Alzueta, M.; Mallada, R.; Santamaria, J., Escaping undesired gas-phase chemistry: Microwave-driven selectivity enhancement in heterogeneous catalytic reactors. *Science advances* **2019,** *5* (3), eaau9000.

200. Rao, K. S.; Chandra, G.; Narasimha Rao, P. V., Study on penetration depth and its dependence on frequency, soil moisture, texture and temperature in the context of microwave remote sensing. *Journal of the Indian Society of Remote Sensing* **1988,** *16* (2), 7-19.

201. Patil, N.; Camacho, A. C.; Mishra, N. K.; Singhla, P.; Sweeney, C. B.; Saed, M. A.; Radovic, M.; Green, M. J., Radio Frequency and Microwave Heating of Preceramic Polymer Nanocomposites with Applications in Mold-Free Processing. *Advanced Engineering Materials* **2019**, 1900276.

202. Ni, Y.; Mulier, S.; Miao, Y.; Michel, L.; Marchal, G., A review of the general aspects of radiofrequency ablation. *Abdominal imaging* **2005,** *30* (4), 381-400.

203. Sweeney, C. B.; Moran, A. G.; Gruener, J. T.; Strasser, A. M.; Pospisil, M. J.; Saed, M. A.; Green, M. J., Radio frequency heating of carbon nanotube composite materials. *ACS applied materials & interfaces* **2018,** *10* (32), 27252-27259.

204. Joseph, R. G.; Peralta, P. N., Nonisothermal radiofrequency drying of red oak. *Wood and Fiber Science* **2007,** *33* (3), 476-485.

205. Marra, F.; Zhang, L.; Lyng, J. G., Radio frequency treatment of foods: Review of recent advances. *Journal of food engineering* **2009,** *91* (4), 497-508.

206. Ioffe, M. S.; Pollington, S. D.; Wan, J. K., High-power pulsed radio-frequency and microwave catalytic processes: selective production of acetylene from the reaction of methane over carbon. *Journal of Catalysis* **1995,** *151* (2), 349-355.

207. Anas, M.; Zhao, Y.; Saed, M. A.; Ziegler, K. J.; Green, M. J., Radio frequency heating of metallic and semiconducting single-walled carbon nanotubes. *Nanoscale* **2019,** *11* (19), 9617-9625.

208. Patil, N.; Zhao, X.; Mishra, N. K.; Saed, M. A.; Radovic, M.; Green, M. J., Rapid Heating of Silicon Carbide Fibers under Radio Frequency Fields and Application in Curing

Preceramic Polymer Composites. *ACS Applied Materials & Interfaces* **2019,** *11* (49), 46132-46139.

209. Sweeney, C. B.; Lackey, B. A.; Pospisil, M. J.; Achee, T. C.; Hicks, V. K.; Moran, A. G.; Teipel, B. R.; Saed, M. A.; Green, M. J., Welding of 3D-printed carbon nanotube–polymer composites by locally induced microwave heating. *Science advances* **2017,** *3* (6), e1700262.

210. Patil, N.; Mishra, N. K.; Saed, M. A.; Green, M. J.; Wilhite, B. A., Radio Frequency Driven Heating of Catalytic Reactors for Portable Green Chemistry. *Advanced Sustainable Systems n/a* (n/a), 2000095.

# APPENDIX A

## RF REACTORS FOR PORTABLE GREEN CHEMISTRY*

## A.1 Introduction

Heterogeneous catalytic reactions, which require operating temperatures ranging from >100 °C to 1000 °C, pose a central challenge to achieving modular chemical processing in the absence of conventional plant-site utility infrastructure; this class of unit operation accounts for upwards of 80% of all chemical conversion processes. [180-188] Conventional catalytic reactor designs rely upon combustion for direct or indirect heating, with the latter requiring additional utility infrastructure for steam generation.[189-190] In addition to limiting the modularity of the resulting overall process, combustion-based heating of catalytic reactors results in significant greenhouse gas emissions.[191] According to a recent study, the chemicals and petrochemicals industries account for ~10% of global energy consumption and ~7% of greenhouse gas emissions.[181] Lastly, external heating of catalytic packed beds introduces radial heat transport limitations which can compromise catalyst efficiency, reaction selectivity and opportunities for scale-up.[192-193]

Recent studies have explored electric power-to-heat strategies in chemical production, termed as "power to chemicals"[194] and these electrically driven heterogeneous catalytic chemical processes can support distributed manufacturing. The use of electricity from carbon neutral sources can significantly reduce greenhouse gas emissions and directly support the realization of a carbon neutral chemical industry.[194-196] Wismann *et al.* designed a laboratory scale reactor from FeCrAl alloy coated with nickel-impregnated washcoat on interior for methane reforming achieving 85 %

* Reprinted with permission from (Nutan Patil, Naveen K. Mishra, Mohammad A. Saed, Micah J. Green, and Benjamin A. Wilhite, Radio Frequency Driven Heating of Catalytic Reactors for Portable Green Chemistry. Adv. Sustainable Syst. 2020, 2000095. https://doi.org/10.1002/adsu.202000095.) Copyright 2020 John Wiley and Sons.

conversion of methane. [197] The direct electrical heating of catalytic surface assisted in minimizing thermal gradients, increasing catalyst utilization, and limiting unwanted byproduct formation. However, direct current approach requires electrical contact with reactor internals and thus is limited by safety issues.

In contrast, use of noncontact microwave field (300 MHz – 300 GHz) enables indirect dielectric heating of the catalyst with the additional advantage of rapid heating times and high heating rates over conventional heating methods.[198] Ramirez *et al*. showed a similar finding that homogeneous undesired reactions can be avoided due to the lower gas phase and catalyst support temperature in microwaves for oxidative dehydrogenation of isobutane.[199] However, microwave frequencies are also limited by penetration depth, higher reflection and lower safety exposure limits. [200]

Radio frequency waves (1 MHz-200 MHz) can achieve faster and uniform heating as compared to conventional methods and they also have a greater penetration depth than microwaves.[201] They have been studied for a variety of application ranging from medical ablation,[202] polymer welding,[203] wood drying,[204] and food processing applications.[205] Ioffe *et al.* used high power RF (2.5 KW) for acetylene production from methane over activated carbon catalyst.[206] In our recent work, carbon nanotubes and silicon carbide fibers were used as RF susceptors to cure preceramic polymers to silicon carbides for noncontact processing in 3D printing, composite manufacturing and fiber processing applications.[201] Our group has studied RF susceptive novel nanomaterials including multi walled carbon nanotube (MWCNTs) ,[203] metallic and semiconducting single walled carbon nanotube,[207] MXenes, and silicon carbide fibers[208] and it was observed that these materials heat up to significantly high temperatures under low power RF radiation.

This study reports for the first time the use of radio frequency to selectively heat RF susceptible catalyst coatings or supports to drive an endothermic heterogeneous reaction using noncontact applicators. Multiwalled carbon nanotubes (MWCNTs) evolve heat on exposure to RF fields due to the vibration of the electrons in π bonds and SiC fibers heat due to interfacial polarization on surface of fibers. Thus, these two materials were used as model RF susceptors in this study. This concept was demonstrated for methanol steam reforming reaction using platinum as a catalyst. The RF heating response of CNT/Pt/alumina and SiC fiber/Pt were investigated for varying temperature using different kinds of applicators. The product flow and conversion for three different reaction temperatures were compared to conventional ovens. This method has application in power to heat route where conventional ovens and gas-fired reactors could be replaced by electricity for portable and distributed chemical production.

## A.2 Experimental Section

### *A.2.1 Materials:*

MWCNT (Cheaptubes, purity > 95 wt %), alumina nanopowder (5nm, Sigma Aldrich), and platinum on alumina powder (5 wt. % in alumina, 44 microns, Sigma Aldrich) were used to prepare a catalyst wash coat. Sodium dodecyl sulfate (Sigma Aldrich) was used as a surfactant to make a dispersion of MWCNT in water. SiC fibers supplied by COI Ceramics (Hi Nicalon type) were used and sputter coated with platinum.

### *A.2.2 Catalyst preparation:*

1 wt. % SDS was added to 30 ml of distilled water followed by mixing 1 wt. % MWCNTs to the mixture which was tip sonicated for 15 mins at 30 W power to prepare a well dispersed solution. Platinum on alumina particles (5 wt. % in alumina, 44 microns, Sigma Aldrich) and

alumina nano powder (5nm, Sigma Aldrich) (to adjust the viscosity of coating) were added to this water-SDS mixture and it was tip sonicated for another 15 mins. A $75\ mm \times 10\ mm \times 1\ mm$ glass slide was then coated with this aqueous solution and dried at ambient conditions for 24 hrs. The estimated dried coating composition is 6.5 wt. % MWCNT, 6.5 wt. % SDS, 2.8 wt. % Pt and 84.2 wt. % $Al_2O_3$ weight assuming complete evaporation of water from the washcoat solution. In order to remove SDS, the coating was pretreated by heating under RF fields using parallel plate applicator at 35 W power and 120 MHz frequency for 20 min at 300 $^{o}$C to decompose SDS. Glass slide was used as it was convenient to perform temperature measurements and optical analysis on a flat surface rather than on curved surfaces like the interior of the quartz tube Silicon carbide fiber was used as a substrate for depositing platinum on its surface. The catalyst thin films of platinum with an average thickness of 1.5 nm were prepared by means of Sputter Coater (208 HR by Cressington) at room temperature using a 2″-diameter platinum (99.95% purity) target and DC power of 10 W. Argon was used as a working gas for the growth of metallic platinum. With a constant gas pressure in the magnetron chamber at $4 \times 10^{-1}$ Pa the deposition rate was approximately 3 nm/min for metallic platinum.

### *A.2.3 RF reactor*

The RF source is a signal generator (DSG815, Rigol Inc.) and amplifier (GN500D, Prana R&D) connected to the applicator via 50-ohm coaxial cable with alligator clips. In this study, three types of RF applicator geometries were used: (a) Parallel plate capacitor, and (b) Fringing field applicator. For parallel plate applicator, two copper plates separated by 0.625 inch spacing were connected to ground and hot terminal of RF power source using alligator clips. In order to obtain the desired temperature, RF power was varied. For fringing field applicator, we used a quartz tube with two copper strips wound around the tube with one inch spacing. All temperature

measurements were made using Forward Looking Infrared Camera (FLIR). The target temperature for the reaction were 220 $^{o}$C, 250 $^{o}$C and 280 $^{o}$C for MWCNT as RF susceptor The RF power was varied such that we achieved $T_{avg}$ around these values in 180 seconds of RF exposure.

All temperature measurements were made using Forward Looking Infrared Camera (FLIR) as conventional thermocouples do not work in RF fields and are strongly affected by the electric current. For, maximum RF heating there needs to be an impedance match between the source and applicator system. It can be done either by using an auto tuner or by frequency sweep. We used the latter approach and manually chose an RF frequency where we observed maximum temperature at constant power.

The target temperature for the reaction were 220 $^{o}$C, 250 $^{o}$C and 280 $^{o}$C for CNT as RF susceptor The RF power was varied such that we achieved $T_{avg}$ around these values in 180 seconds of RF exposure. In order to perform temperature measurements without reaction, we used two quartz tubes with copper tape wrapped around and separated them. Depending on temperature values attained and uniformity of heating, half inch spacing was used for the reaction experiments.

The reactor setup comprised of a bubbler with 118 ml of methanol and 282 ml water such that the molar ratio of vapors is 1:1. The bubbler was operated at room temperature of 25 $^{o}$C. Argon gas with 99.99% purity was used as a carrier gas and was passed through the bubbler at 30 ml/min flow rate. The reactor comprised of a quartz tube with Swagelok at both ends. The reactor inlet was connected to the outlet of the bubbler and reactor outlet was sent through a liquid trap at -20 $^{o}$ C. The temperature of the moisture trap was controlled using dry ice. The gas flowing out of the liquid trap was sent to a mass flow controller.

Methanol steam reforming reactions were performed with conventional oven heating and RF heating setup. For RF-MWCNT experiments, we used two applicators: a) parallel plate b) Fringing field applicator. The glass slide was placed in the center of the quartz tube. The reactor is purged with argon for 30 mins. After the nitrogen signal drops significantly below the detectable limit, RF power was turned on. We performed the reaction at three different average temperatures: previous RF heating experiments determined 220 $^{o}$C, 250 $^{o}$C and 280 $^{o}$C. RF power required to achieve the desired temperature. RF power was on for 15 mins approximately for all reaction experiments. The hydrogen signal was recorded using the mass spectrometer throughout the experiment.

## A.3 Results and Discussion

### *A.3.1 Characterization of catalyst*

The RF-responsive catalytic wash coating was fabricated from a combination of commercial 5 wt. % platinum on alumina (44 microns, Sigma Aldrich), alumina nanopowder (5 nm, Sigma Aldrich), and multi walled carbon nanotubes (10-20 nm, Cheaptubes). Initial tests confirmed negligible heating response of the as-procured Pt-$Al_2O_3$ catalyst powder to the RF field. In our previous studies, a strong relation between electrical percolation and CNT loading on the heating response of CNT composites was observed, wherein, very high loadings of MWCNTs above percolation threshold results in increased conductivity and reflection of electromagnetic waves which compromises RF heating response.[209] Figure A- 1shows a microscopic image of two coatings where coating A is cracked and comprises of aggregates and results in poor heating whereas coating B, which is more uniform, resulted in a maximum heating response. Thus, an intermediate MWCNT solid loading of 7 wt. % was targeted and the solutions were properly dispersed to avoid agglomerate formation.

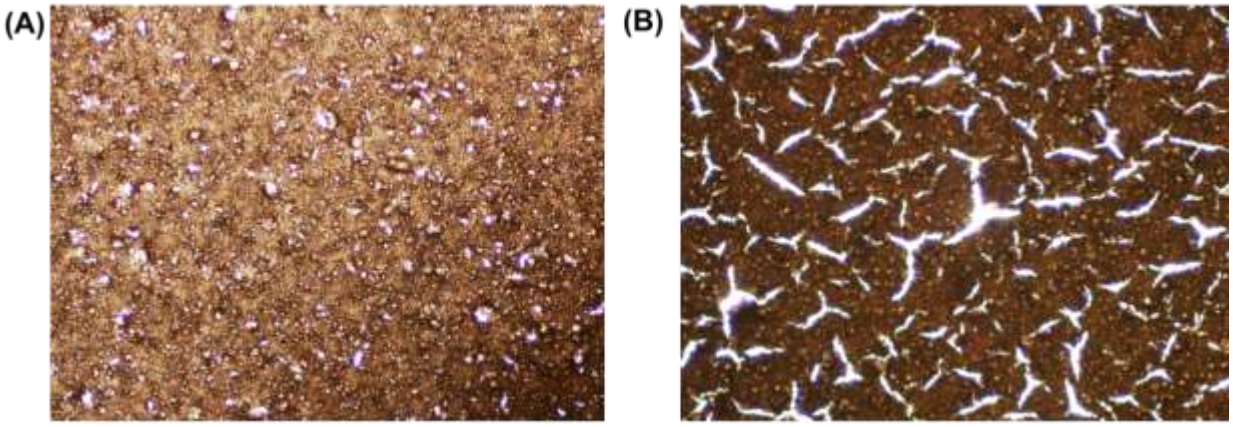


*Figure A- 1: Optical image of the wash coat showing a (A) RF responsive continuous coating, (B) Poor RF responsive cracked coating.*

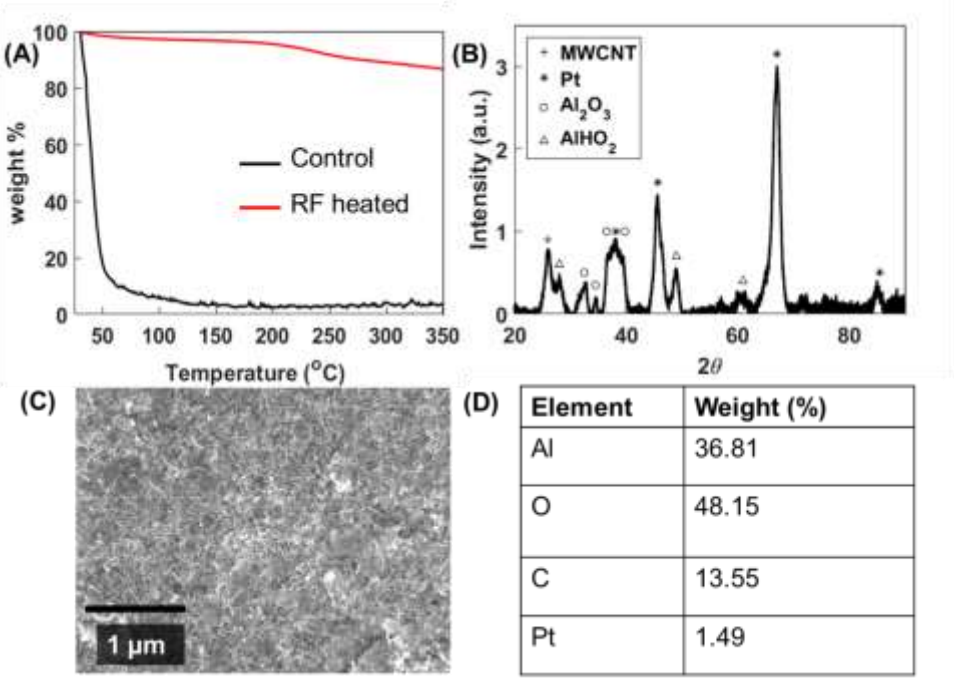


| Element | Weight (%) |
|---|---|
| Al | 36.81 |
| O | 48.15 |
| C | 13.55 |
| Pt | 1.49 |

*Figure A-2: Catalyst characterizations: (A) XRD data for CNT/Pt/Al2O3 wash coat, alumina is found in its hydroxide and oxide forms since coating is made from aqueous solution. (B) SEM image of the wash coat shows that the dispersion of MWCNTs was uniform. (C) TGA weight % vs. temperature data on wash coat before and after RF heating; shows that SDS degrades after the heat treatment. (D) EDS data showing weight % of respective elements in the wash coat.(Reprinted with permission from Patil & Mishra et al.)*[210]

A wash coating solution was prepared by tip sonicating 1 wt.% of MWCNTs in 1 wt.% SDS in DI water for 15 minutes followed by addition of 5 wt. % platinum in $Al_2O_3$ and alumina nano powder and tip sonication for another 15 mins. A $75\ mm \times 10\ mm \times 1\ mm$ glass slide was then coated with this aqueous solution and dried at ambient conditions for 24 hrs. The estimated dried coating composition is 6.5 wt. % MWCNT, 6.5 wt. % SDS, 2.8 wt. % Pt and 84.2 wt. % $Al_2O_3$ weight assuming complete evaporation of water from the washcoat solution.

In order to remove SDS, the coating was pretreated by heating under RF fields using parallel plate applicator at 35 W power and 120 MHz frequency for 20 min at 300 $^{o}$C to decompose SDS). Thermal Gravimetric Analysis of the coating before and after RF heating indicates virtually most of the SDS decomposes during the pretreatment (Figure A-2A). Assuming complete removal of SDS, the final composition of the catalyst wash coating is calculated as 7 wt. % MWCNT, 3 wt. % Pt, and 90 wt. % $Al_2O_3$. Figure A-2B presents X-ray Diffraction analysis of wash coat prior to treating obtained for $2\theta$ values of 20 $^{o}$ to 90 $^{o}$ at a scan rate of 1.8 $^{o}$/min, indicates peaks for platinum at 45 $^{o}$ and 65 $^{o}$, and alumina in its oxide (32.5$^{o}$, 34.5 $^{o}$, 36.5 $^{o}$, 39.8 $^{o}$) and hydroxide form (28 $^{o}$, 49 $^{o}$, 61 $^{o}$) as shown in Figure A-2B. The Scanning Electron Microscopy and Energy Dispersive X-ray Spectroscopy analysis on the wash coat before heating indicate uniform coating with excess O and C content resulting from SDS. Figure A-2C shows the uniform distribution of all four species over the catalyst wash coat; multiple EDS mapping throughout various areas on wash coat rendered a similar composition (Figure A-2D).

### *A.3.2 Heating Response*

The RF heating response of the pretreated wash coat was measured using parallel plate and fringing field applicators in the absence of chemical reaction. The RF source comprised of a signal generator (DSG815, Rigol Inc.) and amplifier (GN500D, Prana R&D) connected to the applicator

via 50-ohm coaxial cable with positive and negative alligator clips. Average surface temperature of the coating was monitored using a Forward Looking Infrared (FLIR) camera (A655sc, FLIR Systems Inc.). The RF heating response was initially optimized by matching impedance of the RF power source and the setup by manually varying the frequency at affixed power output to maximize temperature increase, this frequency was maintained over the full range of studied power levels. Hence, for this experiment, only 1-inch length of glass slide was heated, and reactions were carried over smaller catalyst loading as compared to parallel plate setup. Figure A-3A and Figure A-3B show the equilibrium average surface temperature attained after 180 s vs. RF power applied for both applicators at 120 MHz and 180 MHz, with a linear relationship between temperature and power for each.

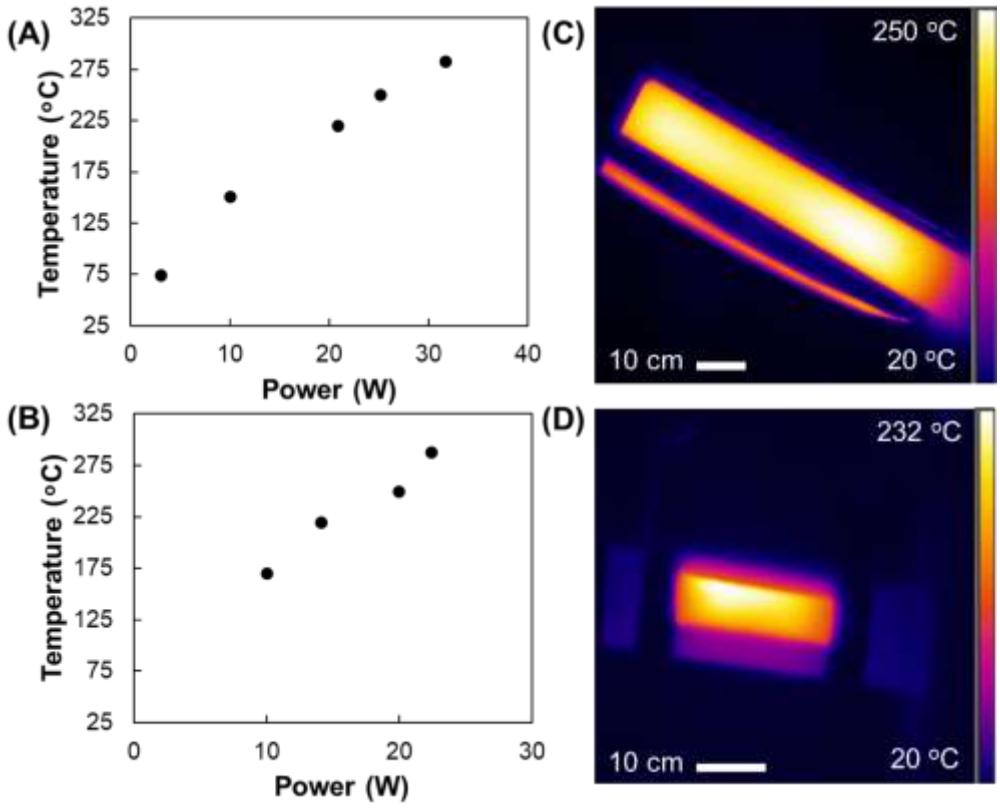


*Figure A-3: Steady state average temperature measured 180 s after RF power is on for CNT/Pt/$Al_2O_3$ wash coat catalyst tested on: (A) Parallel plate applicator, and (B) Fringing field applicator. Thermal image of catalyst wash coat heated using: (C) Parallel plate applicator and (D) Fringing field applicator.(Reprinted with permission from Patil & Mishra et al.)*[210]

### *A.3.3 RF Reactor*

Methanol steam reforming (MSR) reaction was employed to demonstrate catalytic reaction using novel RF-active catalytic mixture. MSR is an endothermic reaction where methanol and water decompose over a transition metal or oxide catalyst to form hydrogen and carbon dioxide via the following overall reaction:

$$CH_3OH + H_2O \rightarrow CO_2 + 3H_2 \qquad \Delta H = 49.2 \text{ kJ/mol}$$

**Table A-1: Methanol conversion obtained via RF field heating compared to conventional external (oven) heating.**

| CATALYST | T (°C) | METHANOL CONVERSION (%) | |
|---|---|---|---|
| | | RF Heating | Oven Heating |
| CNT/Pt/$Al_2O_3$ | 220 | 0.96 | 1.25 |
| CNT/Pt/$Al_2O_3$ | 250 | 1.19 | 1.93 |
| CNT/Pt/$Al_2O_3$ | 280 | 3.34 | 5.07 |
| SiC fiber/Pt | 400 | 1.52 | 1.89 |

A glass slide with 107 mg of catalyst washcoat was placed in the center of a half-inch quartz tube with Swagelok fittings on both ends to provide inlet and outlet gas connections (Figure 4.4A). Argon as a carrier gas was passed through a bubbler containing 118 ml of methanol and 282 ml water such that the vapor mole ratio of methanol and water was 1:1 as per Vapor Liquid Equilibrium (VLE) curve. The catalyst was then heated using either of the two RF applicators at

the previously identified resonant frequency (120 MHz and 180 MHz respectively for two RF applicators) to target three different temperatures: 220 $^{o}$C, 250 $^{o}$C and 280 $^{o}$C. As the quartz tube enclosure prevents temperature measurement under reaction conditions, temperature calibrations from were used to estimate the temperature. The outlet of the quartz tube was passed through a liquid trap at -20$^{o}$ C to remove any moisture and unreacted methanol prior to analysis via mass spectrometer to estimate the dry basis hydrogen composition in the product stream. The RF power was turned on for 15 mins at predefined power levels. Inlet vapor composition (Argon: 96.8 %, Methanol: 1.6 %, water 1.6 %, by volume) was calculated based on the humidity of the vapor (30 %, measured by hygrometer) and VLE for the methanol-water mixture (additional details can be found in the SI) at 298 K. The conversion of methanol to hydrogen was defined as:

$$X = \frac{1}{3} \frac{moles\ of\ H_2\ in\ outlet}{moles\ of\ methanol\ inlet} \times 100$$

Figure A-4B shows the parallel plate RF heating setup used to carry out MSR reaction with 7.5 cm$^2$ catalyst wash coating area (3 mg total platinum), respectively. Figure A-4C shows the steady state methanol conversion vs. temperature for the RF setup. The same catalyst coating was used in a conventional oven setup to compare the results from RF reactor. Once the furnace reached the set temperature (220 $^{o}$C, 250 $^{o}$C and 280 $^{o}$C), the quartz tube with catalyst coated glass slide was placed in the preheated tube furnace with identical inlet and outlet connections for estimating dry basis hydrogen outflow.

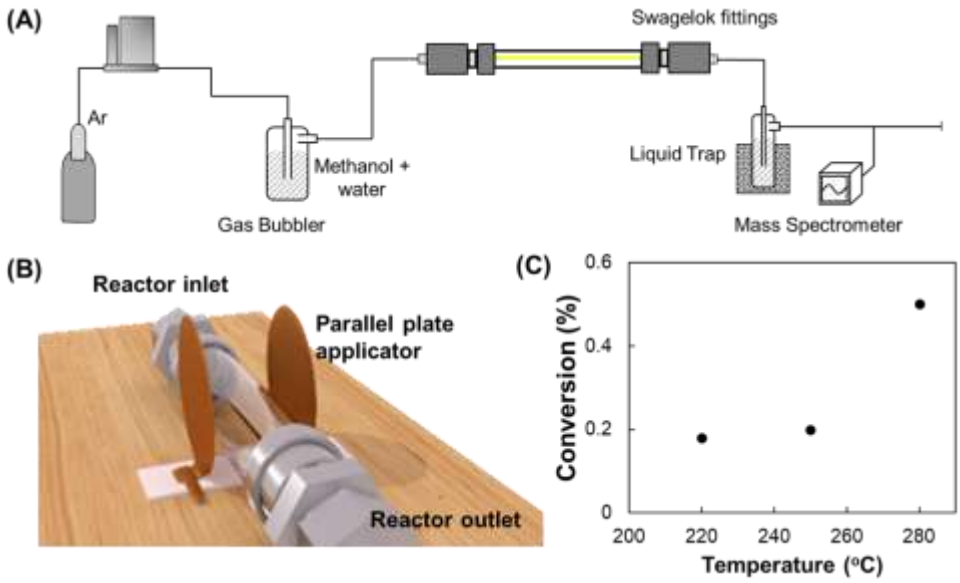


*Figure A-4: (A) Schematics of experimental set up used for methanol steam reforming. (B) Schematic of RF reactor setup using a parallel plate applicator. (C) Steady state conversion vs. reaction temperature for 3 mg platinum.(Reprinted with permission from Patil & Mishra et al.)*[210]

The summarized conversion data for RF and oven heating can be found in Table 4.1. For the target temperatures of 220 $^{o}$C and 250 $^{o}$C, the methanol conversion and hydrogen yield for RF reactor was comparable to that of the oven reactor; however, in the case of target temperature of 280 $^{o}$C, a significant difference in conversion was observed. The low conversion reported for Rf reactor at 280 $^{o}$C can be attributed to inaccuracies in temperature calibration as thermal imaging required for calibration experiments were performed in the absence of gas flow and associated convective losses due to gas flow during the experiment.

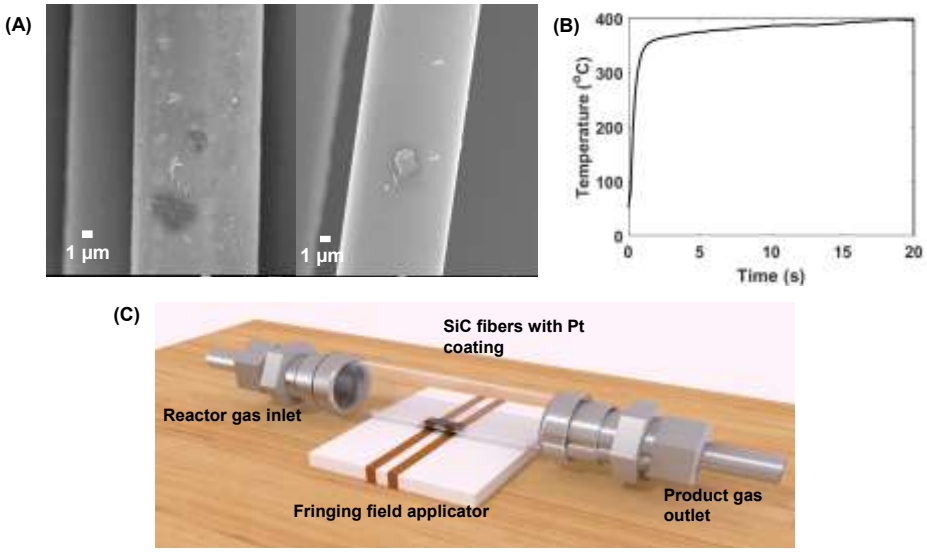


*Figure A-5: (A) SEM image of the fiber showing presence of Si/O/C impurities on the surface of the fiber, (B) RF heating response of SiC fiber with 1 nm sputter coating at 50 W. (C) Schematic of RF heating applicator system used for the reactor setup.(Reprinted with permission from Patil & Mishra et al.)*[210]

A second proof-of-concept experiment was performed using SiC fibers as catalytic support for a sputter coated platinum catalyst for methanol steam reforming. Our previous work has shown rapid RF heating property of commercial Hi-Nicalon silicon carbide fibers and turbostratic carbon on surface of fibers. A 1 nm platinum sputter coating was applied to the surface of these fibers using a sputter coater (208 HR, Cressington). The fibers were placed in the center of the quartz tube and heated using a fringing field applicator at 30 W RF power and 100 MHz frequency to 400 $^{o}$C (Figure 4.5A). Figure 4.5B shows the SEM images of fibers used as susceptors. The same sputter coated platinum on SiC fiber was used in a conventional oven heating method at the same temperature and the results were comparable. Since the catalyst loading was low (1 nm coating); the conversion of methanol was low; an increase in hydrogen flowrate as RF power is turned on and a drop as RF power is turned off is observed.

## A.4 Conclusion

A new route for chemical synthesis was demonstrated utilizing the interaction between RF susceptors and RF fields to heat catalytic sites and drive the reaction. The RF susceptors can be added to catalyst add mixture to form a coating or used as catalyst support. This route for chemical synthesis offers selective, volumetric, and local heating of catalysts without need of an external heat source like an oven. It is a potential breakthrough over conventional catalytic reactors as it enables small, safe, sustainable, on-site, and on-demand production of chemicals in the absence of traditional manufacturing infrastructure. A proof-of-concept of this method was shown for methanol steam reforming reaction using platinum as catalyst with two different types of RF applicators. The methanol conversion for RF experiment was comparable to oven heating.

The introduction of new chemicals to the market is often limited by the high risk and capital involved in the scale up from laboratories to industrial scale. This method could be useful for scale-up studies from laboratory to industry, and rapid screening of different catalysts and reaction pathways. This style of chemical production will be advantageous for the fine chemicals and in pharmaceutical industry, where annual production is often less than a few metric tons per day. This method also offers isolation of the reaction zone, which minimizes heat losses and increases safety. For heterogeneous catalysis, the selective heating of catalytic sites can prevent undesired side reactions for specific chemistries. Energy from intermittent renewable energy sources can be converted to electricity and stored in the form of chemicals using such RF reactors resulting in significant $CO_2$ savings. Thus, this method has direct application in sustainable and distributed production of chemicals like methanol, ammonia etc.